

FAILURE ANALYSIS OF INFRARED SENSING DEVICES DUE TO
CRYOGENIC COOLING

A THESIS SUBMITTED TO
THE GRADUATE SCHOOL OF NATURAL AND APPLIED SCIENCES
OF
MIDDLE EAST TECHNICAL UNIVERSITY

BY

EYÜP CAN BALOĞLU

IN PARTIAL FULFILLMENT OF THE REQUIREMENTS
FOR
THE DEGREE OF DOCTOR OF PHILOSOPHY
IN
MECHANICAL ENGINEERING

JUNE 2023

Approval of the thesis:

**FAILURE ANALYSIS OF INFRARED SENSING DEVICES DUE TO
CRYOGENIC COOLING**

submitted by **EYÜP CAN BALOĞLU** in partial fulfillment of the requirements for
the degree of **Doctor of Philosophy in Mechanical Engineering Department,**
Middle East Technical University by,

Prof. Dr. Halil Kalıpçılar
Dean, Graduate School of **Natural and Applied Sciences**

Prof. Dr. M.A. Sahir Arıkan
Head of Department, **Mechanical Engineering**

Assoc. Prof. Dr. Hüsnü Dal
Supervisor, **Mechanical Engineering, METU**

Examining Committee Members:

Prof. Dr. Fevzi Suat Kadiođlu
Mechanical Engineering, METU

Assoc. Prof. Dr. Hüsnü Dal
Mechanical Engineering, METU

Assoc. Prof. Dr. Sezer Özerinç
Mechanical Engineering, METU

Prof. Dr. Recep Güneş
Mechanical Engineering, Erciyes University

Assist. Prof. Dr. Mehmet Okan Görtan
Mechanical Engineering, Hacettepe University

Date:02.06.2023

I hereby declare that all information in this document has been obtained and presented in accordance with academic rules and ethical conduct. I also declare that, as required by these rules and conduct, I have fully cited and referenced all material and results that are not original to this work.

Name, Surname: Eyüp Can Balođlu

Signature :

ABSTRACT

FAILURE ANALYSIS OF INFRARED SENSING DEVICES DUE TO CRYOGENIC COOLING

Balođlu, Eyüp Can

Ph.D., Department of Mechanical Engineering

Supervisor: Assoc. Prof. Dr. Hüsnü Dal

June 2023, 142 pages

Development of Infrared Focal Plane Array (IRFPA) structures have become increasingly important in recent years due to their applications in a wide range of fields, including thermal imaging, remote sensing, security, surveillance, earth observation and astronomy. Semiconductor compounds used in IRFPA technologies are typically exposed to a wide range of temperatures during their operation and storage. Temperature-dependent material properties, such as thermal expansion coefficient, elastic constants, and heat capacity, play a crucial role in the performance and reliability of IRFPA devices. Therefore, it is important to have accurate and reliable temperature-dependent material properties for these materials. Having complete and accurate information about material properties is required for designing and optimizing IRFPA devices. In this thesis, Density Functional Theory (DFT) is implemented within quasi-harmonic approach to define temperature dependent material properties which is the first attempt for the selected III-V and II-VI semiconductor compounds (GaSb, InSb, CdTe, HgTe, ZnTe, CdZnTe). Both LDA and PBEsol approximations are used to obtain thermo-elastic material properties. Nanoindentation experiments on GaSb are conducted at room temperature to verify obtained material properties

such as elastic modulus and Vicker's hardness by DFT. Experimental results show good coherence with numerical outcomes of DFT for GaSb material. To mimic operation conditions of IRFPA structures at cryogenic temperatures, a custom test setup with cryocooler is designed. Crack initiation and propagation of GaSb and CdZnTe materials on SS304 material due to developed thermo-mechanical stress by cryocooling are investigated with this test setup and scanning electron microscopy (SEM) is used to observe cracks at room temperature. Thermo-mechanic stress determinations on bimaterial assemblies as well as on a representative IRFPA structure are performed with finite element simulations to show determined stress dependence on defined material properties. A novel phase field fracture model is developed to simulate crack initiation and propagation for materials that belongs to cubic anisotropy. Anisotropic energy based failure criterion that splits the free energy and eventually crack driving source into isotropic and anisotropic parts is used. Representative numerical example with a notched geometry is also provided for different in plane material orientations of GaSb. Obtained material properties of GaSb by DFT are used as material inputs of phase field fracture simulations. Both numerical and experimental investigations on semiconductor materials are performed. A novel and complete framework on failure analysis of IR sensing materials that cover from temperature dependent material property determinations to crack initiation/propagation subjects is developed.

Keywords: Cooled infrared detectors, temperature dependent material properties, density functional theory, nanoindentation, fracture in cubic anisotropic materials

ÖZ

KIZILÖTESİ ALGILAMA AYGITLARININ KRİYOJENİK SOĞUMAYA BAĞLI HASAR ANALİZİ

Baloğlu, Eyüp Can

Doktora, Makina Mühendisliği Bölümü

Tez Yöneticisi: Doç. Dr. Hüsnü Dal

Haziran 2023 , 142 sayfa

Kızılötesi Odak Düzlemi Dizilimi (IRFPA) yapılarının geliştirilmesi, termal görüntüleme, uzaktan algılama, güvenlik, gözetleme, yer gözlemi ve astronomi dahil olmak üzere çok çeşitli alanlardaki uygulamaları nedeniyle son yıllarda giderek daha önemli hale gelmiştir. IRFPA teknolojilerinde kullanılan yarı iletken bileşikler, operasyon ve depolama durumları sırasında geniş bir sıcaklık aralığına maruz kalırlar. Termal genleşme katsayısı, elastik sabitler ve ısı kapasitesi gibi sıcaklığa bağlı malzeme özellikleri, IRFPA cihazlarının performansında ve güvenilirliğinde önemli bir rol oynar. Bu nedenle, bu malzemeler için doğru ve güvenilir, sıcaklığa bağlı malzeme özelliklerine sahip olmak önemlidir. IRFPA cihazlarını tasarlamak ve optimize etmek için malzeme özellikleri hakkında eksiksiz ve doğru bilgilere sahip olmak gereklidir. Bu tezde, seçilen III-V ve II-VI yarı iletken bileşikler (GaSb, InSb, CdTe, HgTe, ZnTe, CdZnTe) için ilk deneme olan sıcaklığa bağlı malzeme özelliklerini tanımlamak için yarı harmonik yaklaşımla Yoğunluk Fonksiyonel Teorisi (DFT) uygulanmıştır. Termo-elastik malzeme özelliklerini elde etmek için hem LDA hem de PBEsol yaklaşımları kullanılmıştır. DFT ile elde edilen malzeme özelliklerini, elastik modülü ve Vicker sert-

liđi gibi, dođrulamak için GaSb üzerinde nanoindentasyon deneyleri oda sıcaklığında gerçekleştirilmiştir. Deneysel sonuçlar, GaSb malzemesi için DFT'nin sayısal sonuçlarıyla iyi bir tutarlılık göstermektedir. IRFPA yapılarının kriyojenik sıcaklıklarda çalışma koşullarını taklit etmek için kriyosođutuculu özel bir test düzeneđi tasarlanmıştır. Bu test düzeneđi ile GaSb ve CdZnTe malzemelerinin SS304 malzeme üzerinde gelişen termo-mekanik gerilme nedeniyle çatlak başlatması ve ilerlemesi bu test düzeneđi ile incelenmekte ve çatlakların oda sıcaklığında gözlemlenmesi için taramalı elektron mikroskobu (SEM) kullanılmaktadır. Bimateryal yapılarda ve ayrıca temsili bir IRFPA yapısındaki termo-mekanik gerilme belirlemeleri, tanımlanmış malzeme özelliklerine bađlı gerilme dođruluđunu göstermek için sonlu eleman simülasyonları ile gerçekleştirilmiştir. Kübik anizotropiye ait malzemeler için çatlak başlangıcını ve ilerlemesini simüle etmek için yeni bir faz alanı kırılma modeli geliştirilmiştir. Serbest enerjiyi bölen ve sonunda itici kaynađı izotropik ve anizotropik parçalara ayıran anizotropik enerji tabanlı başarısızlık kriteri kullanılmıştır. GaSb malzeme için farklı düzlem malzeme oryantasyonları için çentikli bir geometriye sahip temsili sayısal örnek de sağlanmıştır. DFT ile GaSb'nin elde edilen malzeme özellikleri, faz alanı kırılma simülasyonlarının malzeme girdileri olarak kullanılmıştır. Yarı iletken malzemeler üzerinde hem sayısal hem de deneysel arařtırmalar yapılmıştır. Sıcaklığa bađlı malzeme özelliđi belirlemelerinden çatlak başlatma/yayıma konularını kapsayan IR algılama malzemelerinin başarısızlık analizine iliřkin yeni ve eksiksiz bir çerçeve geliştirilmiştir.

Anahtar Kelimeler: Sođutmalı kızılötesi dedektörler, sıcaklığa bađlı malzeme özellikleri, yoğunluk fonksiyonel teorisi, nanoindentasyon, kübik anizotropik malzemelerde çatlak

To my family

ACKNOWLEDGMENTS

First and foremost, I extend my heartfelt appreciation to my supervisor, Assoc. Prof. Dr. Hüsni Dal, for his exceptional guidance, scholarly expertise, and invaluable mentorship throughout my research journey.

I am grateful to my advisory committee, Assoc. Prof. Dr. Cihan Tekoğlu and Assoc. Prof. Dr. Sezer Özerinç for their invaluable insights and constructive criticism. I would like to express my sincere thanks to Assoc. Prof. Dr. Hande Toffoli Üstünel, for her support and guidance on DFT studies that have greatly contributed to the depth and understanding of this research.

I would like to express my gratitude to my colleagues and fellow researchers, Dr. Ozan Arı, Dr. Funda Aksu Denli for their guidance, support and fruitful discussions. I want to extend my sincere thanks to the team at Aselsan Inc. for their support and collaboration. Their expertise have greatly contributed to the success of this research.

I would also like to acknowledge Arda and Mesut for their camaraderie and endless motivating conversations. Together with the Nerminator team, Ozan, Bahadır, Emre, their encouragement, and uplifting words have been instrumental throughout this journey.

I am profoundly grateful to my girlfriend, Gizem, for her unwavering love, support, and understanding. Her presence in my life has been a constant source of inspiration and motivation.

Lastly, I want to acknowledge my family for their unconditional love, encouragement, and belief in my abilities. Their unwavering support has been instrumental in keeping me motivated and focused during this journey.

To all those mentioned and those who may not be explicitly named, your contributions, both big and small, have shaped this thesis and made it possible. Thank you all for being an integral part of this transformative experience.

TABLE OF CONTENTS

ABSTRACT	v
ÖZ	vii
ACKNOWLEDGMENTS	x
TABLE OF CONTENTS	xi
LIST OF TABLES	xv
LIST OF FIGURES	xvi
LIST OF ABBREVIATIONS	xxii
CHAPTERS	
1 INTRODUCTION	1
1.1 Introduction	1
1.2 Literature Review on Material Properties of III-V and II-VI Semi-conductors	7
1.3 Literature Review on Phase Field Theory	11
1.4 Objective of Thesis	13
2 FUNDAMENTALS OF DENSITY FUNCTIONAL THEORY AND PHASE FIELD THEORY	15
2.1 Basic Concepts of Density Functional Theory	15
2.1.1 Schrödinger equation	16
2.1.2 Hohenberg-Kohn theorems	18

2.1.3	Kohn-Sham method	19
2.1.4	Approximations for exchange-correlation energy, E_{xc}	21
2.1.4.1	Local density approximation, LDA	22
2.1.4.2	Generalized gradient approximation, GGA	22
2.1.5	Tools for ab initio calculations	24
2.2	Basic Concepts of Continuum Mechanics	25
2.2.1	Stress measures	27
2.2.2	Stress power and dual variables	29
2.2.3	Balance laws	31
3	DENSITY FUNCTIONAL THEORY	37
3.1	Theory, Method and Computational Details	37
3.1.1	III-V compounds	38
3.1.2	II-VI compounds	42
3.2	Numerical Results	44
3.2.1	III-V compounds	44
3.2.2	II-VI compounds	51
4	EXPERIMENTAL STUDIES	63
4.1	Nanoindentation	63
4.1.1	Test results on GaSb	67
4.2	Custom Designed Test Setup for Cryocooling	72
4.2.1	Test setup design	72
4.2.2	Cryocooling experiments	74
4.2.2.1	GaSb - SS304 sample	75

4.2.2.2	CdZnTe - SS304 sample	77
5	THERMO-ELASTIC STRESS ANALYSIS OF IRFPA WITH FEM	79
5.1	Thermo-Mechanic Stress Determination on Bimaterial Assembly	79
5.2	Thermo-Mechanic Stress Determination on IRFPA Assembly	81
5.3	Free Energy Function and Stress Expression	85
5.3.1	Cubic anisotropy	86
5.3.2	Thermo-elastic cubic anisotropy	87
5.3.3	The Lamé and γ parameters of GaSb and InSb	89
6	PHASE FIELD THEORY	93
6.1	Introduction	93
6.2	Basics of the Phase Field Model of Fracture	94
6.2.1	Euler-Lagrange equations of the phase field model	98
6.3	Governing Equations of Anisotropic Fracture	99
6.3.1	Finite strain setting	99
6.3.2	Small strain setting	101
6.3.3	Constitutive model for cubic anisotropy	103
6.3.4	Linearization of the constitutive model	105
6.3.5	Energy based anisotropic failure criterion	106
6.4	Representative numerical examples	107
6.4.1	Effect of length scale parameter	107
6.4.2	Uniaxial tension of a notched plate	108
7	CONCLUDING REMARKS	113
	REFERENCES	117

CURRICULUM VITAE 141

LIST OF TABLES

TABLES

Table 1.1	Electromagnetic spectrum [1]	1
Table 3.1	Maximum error between DFT results and the experiments in SOEC.	48
Table 4.1	Geometrical parameters according to indenter shape	65
Table 5.1	Material Properties of GaSb and SS304 at 300K	79
Table 5.2	Geometric dimensions of parts	82
Table 5.3	Poisson ratio of the parts	84
Table 5.4	Rational curve fitting parameters as stated in (5.8),(5.13) for elastic constants of GaSb with goodness of fit parameter of R-sq.	89
Table 5.5	Rational curve fitting parameters of InSb according to (5.8),(5.13) with goodness of fit, R-sq.	91

LIST OF FIGURES

FIGURES

Figure 1.1	Infrared imaging scheme	3
Figure 1.2	a) Representative scheme of IR detector hybrid [2], b) Thermal image of IR sensor	4
Figure 1.3	Representative schematic of the cold region	5
Figure 1.4	Direct mechanical failure of a semiconductor	6
Figure 2.1	The deformation gradient \mathbf{F} is defined as a linear tangent map that transforms the material tangent vector, $\mathbf{T} \in T_X\mathcal{B}$ onto the spatial tangent vector, $\mathbf{t} \in T_x\mathcal{S}$	25
Figure 2.2	a) Push-forward, b) Pull-back operations	27
Figure 2.3	Lagrangian $\tilde{\mathbf{T}}(\mathbf{X}, t; \mathbf{N}) \in T_X\mathcal{B}$ and Eulerian $\mathbf{t}(\mathbf{x}, t; \mathbf{n}) \in T_x\mathcal{S}$ traction vectors on cut out parts of reference and deformed surfaces $\partial\mathcal{P}_\mathcal{B}$ and $\partial\mathcal{P}_\mathcal{S}$, respectively.	28
Figure 2.4	The push-forward and pull-back operations on stress measures corresponding to their covariant and contravariant representations.	29
Figure 3.1	Murnaghan EOS fit of volume dependent total Helmholtz free energy for GaSb with PBEsol approximation	41
Figure 3.2	Phonon dispersion plots for GaSb and InSb, respectively.	41

Figure 3.3 (a, b) Calculated temperature-dependent lattice constant of GaSb (left) and InSb (right) with PBEsol (blue), LDA (red). Dotted lines represent the experimental data from Nilsen *et al.* [43] and Breivik *et al.* [51] for GaSb and InSb, respectively, performed by X-ray diffraction measurements. (c, d) Coefficient of thermal expansion (CTE) of GaSb and InSb is provided by using LDA (red) and PBEsol (blue) pseudopotentials. Experimental result of thermal expansion coefficient (green) for GaSb and InSb are provided by Dutta *et al.* [164] and Cai and Wei [52] (green), Breivik *et al.* [51] (orange), Spark and Swenson [167] (purple), respectively. 46

Figure 3.4 (a, b, c, d, e, f) Temperature-dependent second order elastic constants, C_{11} , C_{12} , C_{44} , of GaSb (left) and InSb (right) are provided by using LDA (red) and PBEsol (blue). The supercell size of $3 \times 3 \times 3$ for LDA and PBEsol is only provided for GaSb. There is no significant difference between the two supercell sizes. So, the supercell size of $2 \times 2 \times 2$ is given only for InSb. Experimental data (purple) is taken from Boyle [172] and Slutsky [173]. 47

Figure 3.5 (a) Temperature-dependent Poisson's ratio of GaSb is given with LDA (blue) and PBEsol (orange). (b) Temperature-dependent Vicker's hardness of GaSb provided with LDA (blue) and PBEsol (orange). (c) Temperature-dependent Poisson's ratio of InSb. (d) Temperature-dependent Vicker's hardness of InSb. Both of these are provided with LDA (blue) and PBEsol (orange). Heat capacity results of DFT calculations for GaSb and InSb are given in (e) and (f), respectively. 49

Figure 3.6 (a) Calculated temperature-dependent lattice constant of CdTe with PBEsol (blue), LDA (red). (b) Coefficient of thermal expansion (CTE) of CdTe is provided by using LDA (red) and PBEsol (blue) pseudopotentials. Experimental result of thermal expansion coefficient (green) for CdTe is taken from Bagot et al. [77]. (c) Calculated temperature-dependent lattice constant of HgTe with PBEsol (blue), LDA (red). (d) Coefficient of thermal expansion of HgTe is provided by using LDA (red) and PBEsol (blue). Experimental result of coefficient of thermal expansion of HgTe is also provided by Bagot [77] (green). (e) Lattice constant of ZnTe is given with PBEsol (blue), LDA (red). (f) Thermal expansion coefficient of ZnTe is provided with PBEsol (blue), LDA (red) and compared with available experimental result of Bagot et al. [77]. 52

Figure 3.7 Temperature-dependent second order elastic constants of CdTe are provided by using LDA (red) and PBEsol (blue) with 0.1% strain (left column), 0.5% strain (middle column) and 2% strain (right column). Experimental data (purple) is taken from Greenough and Palmer [176]. 53

Figure 3.8 Temperature-dependent second order elastic constants of ZnTe are provided by using LDA (red) and PBEsol (blue) with 0.1% strain (left column), 0.5% strain (middle column) and 2% strain (right column). Experimental data (purple) is taken from Lee [177]. 54

Figure 3.9 Temperature-dependent second order elastic constants of HgTe are provided by using LDA (red) and PBEsol (blue) with 0.1% strain (left column), 0.5% strain (middle column) and 2% strain (right column). Experimental data (purple) is taken from Cottam [76]. 55

Figure 3.10	(a, d, g) Temperature-dependent second order elastic constants of CdTe are provided by using LDA (red) and PBEsol (blue) with the supercell size of $2 \times 2 \times 2$. Experimental data (purple) is taken from Greenough and Palmer [176]. (b, e, h) For HgTe, the second order elastic constants are provided by using LDA (red) and PBEsol (blue). Experimental data is taken from Cottam and Saunders [76] (green). (c, f, i) Second order elastic constants of ZnTe are provided with LDA and PBEsol. Experimental results of Lee [177] is also provided. LDA estimates approximately 10% larger values of elastic constants. A strain value of 0.001 is used to generate these results.	57
Figure 3.11	(a, b, c) Poisson ratio of CdTe, HgTe and ZnTe in the temperature range from 1K to 600K. (d, e, f) Temperature dependent heat capacity, C_v values of CdTe, HgTe and ZnTe are given in the same temperature interval.	58
Figure 3.12	Second order elastic constants, a) C_{11} , b) C_{12} , c) C_{44} , d) Poisson ratio, e) Vicker's hardness, f) Heat capacity values of CdZnTe	59
Figure 3.13	Temperature dependent energy band-gap of CdZnTe	60
Figure 3.14	Temperature dependent refractive index of CdZnTe	61
Figure 3.15	Temperature dependent extinction constant of CdZnTe	61
Figure 4.1	Typical indentation curve	65
Figure 4.2	Schematic of the indenter-sample contact	66
Figure 4.3	Representative load - displacement curve of nanoindentation test on GaSb with maximum applied load of 20mN	68
Figure 4.4	Measurements of elastic modulus of polished, non-polished GaSb samples by nanoindentation	69
Figure 4.5	GaSb test sample surfaces	69

Figure 4.6	Measurements of hardness of polished, non-polished GaSb samples by nanoindentation	70
Figure 4.7	Zygo New View 7100 optical profiler measurements on the samples	71
Figure 4.8	Test setup schematic	72
Figure 4.9	Test setup design	73
Figure 4.10	Ceramic with an integrated sample on cold head	74
Figure 4.11	Cooldown of the integrated sample	75
Figure 4.12	Observed cracks on GaSb sample	76
Figure 4.13	Observed crack on CdZnTe sample	77
Figure 5.1	a) Mesh structure, b) Defined path on GaSb midplane	80
Figure 5.2	The effect of material property definition on von Mises stress determinations via FEM of the two configuration, i.e, materials properties provided only at 300K and temperature dependent material property for 1K-300K temperature range	81
Figure 5.3	IRFPA model and regarding boundary conditions on the structure	82
Figure 5.4	Defined path on midplane of GaSb	83
Figure 5.5	Thermal expansion coefficient and elastic modulus parameters of the constituent materials on IRFPA assembly.	83
Figure 5.6	Effect of temperature dependent data on von Mises stress and out of plane deformation for defined path.	84
Figure 5.7	Effect of single point material data and temperature dependent data. a), b) represents the effect on von Mises stress, c), d) represents the out of plane deformation results.	85

Figure 5.8	Shear modulus μ , first Lamé parameter λ and the cubic symmetry parameter γ for (left) GaSb and (right) InSb are determined according to (5.8) by using the second order elastic constants C_{11} , C_{12} , C_{44} , and depicted (red) dots. The rational curves according to the parameters provided in Tables 5.4 and 5.5 for GaSb and InSb, respectively, are depicted with (blue) lines,	90
Figure 6.1	Definitions of crack with damage field, d where $d = 0$ represents intact state and $d = 1$ is broken state (a) Sharp crack, (b) Diffusive crack	97
Figure 6.2	Deformation field and crack phase field	97
Figure 6.3	Square plate with a single notch has $1mm$ thickness with the applied boundary conditions	108
Figure 6.4	Effect of length scale parameter on crack (a) $l = 0.3$, (b) $l = 0.6$, (c) $l = 1.2$, (d) $l = 2.4$	109
Figure 6.5	Force displacement results of different in plane material orientations	110
Figure 6.6	Effect of material orientation on crack propagation	111

LIST OF ABBREVIATIONS

IR	Infrared
NIR	Near Infrared
SWIR	Short-wavelength Infrared
MWIR	Mid-wavelength Infrared
LWIR	Long-wavelength Infrared
VLWIR	Very long-wavelength Infrared
FIR	Far Infrared
UV	Ultraviolet
EUV	Extreme Ultraviolet
ROIC	Readout Integrated Circuit
NETD	Noise Equivalent Temperature Difference
MTBF	Mean Time Between Failures
FPA	Focal Plane Array
IRFPA	Infrared Focal Plane Array
DFT	Density Functional Theory
DFPT	Density Functional Perturbation Theory
VASP	Vienna Ab initio Simulation Package
LDA	Local Density Approximation
GGA	Generalized Gradient Approximation
SEM	Scanning Electron Microscopy
OM	Optical Microscopy
CZT	Cadmium Zinc Telluride
MCT	Mercury Cadmium Telluride

CHAPTER 1

INTRODUCTION

1.1 Introduction

Infrared (IR) radiation covers electromagnetic spectrum from 750 nanometers to 1 millimeters. Infrared radiation can be divided into several subgroups according to their wavelength. Basically these subgroups cover the wavelengths from $0.75\mu\text{m}$ to $30\mu\text{m}$. Many opto-electronic devices are built in IR spectrum and abbreviated according to their spectral sensing regions such as NIR (near infrared), SWIR (short-wavelength IR), MWIR (mid wavelength IR), LWIR (long wavelength IR), FIR (far IR). Electromagnetic spectrum that covers IR bands is given in Table 1.1.

Table 1.1: Electromagnetic spectrum [1]

Wideband	Sub-division	λ_{min} (μm)	λ_{max} (μm)
Infrared	Very Longwave Infrared (VLWIR)	12	30
	Longwave Infrared (LWIR)	8	12
	Midwave Infrared (MWIR)	3	5
	Shortwave Infrared (SWIR)	1	3
	Near Infrared (NIR)	0.75	1
Visible		0.38	0.75
Ultraviolet (UV)	Ultraviolet C	0.10	0.38
	Extreme Ultraviolet (EUV)	0.01	0.12
X-Ray		0.00001	0.01

IR imaging devices are commonly used in military applications such as night vision

devices, missile guidance, thermal cameras for border security, unmanned aerial vehicles. Moreover, there also exist many applications of these devices in space, industry, medical and civil areas. Satellite earth observation, space telescopes, early detection and determination of cancer, petroleum exploration, rail safety, moisture analyzing are some of the applications from different industries. In addition, there are many other applications that is used in daily life such as infrared security cameras in airports, park sensors in automobiles. IR imaging systems are also commonly used in different weather conditions that causes poor visibility such as foggy and snowy weathers or nighttime conditions.

Each object that has a temperature greater than absolute zero (0K) has emits radiation which can be defined as self radiation. The self radiation is dependent on temperature and the radiating surface characteristics. IR sensors detect the self radiation of an object due to its temperature. IR imaging devices contains IR sensing layers that are made from semiconductor materials which will be explained in a more detailed manner later. The pathway of image production is basically given as follows, IR radiation that is coming from self radiated object is collected by IR sensing layer. The absorbed radiation can turn into an electrical or thermal signal depending on which type of sensor is built, i.e, thermal detector or photon detector. In photon detectors, the sensing layer produces an electrical signal due to moving electrons in this layer that regards to the absorbed IR radiation. The moving electrons that change electrical properties of the sensing layer is measured by an external circuit called as readout integrated circuit (ROIC). Produced electrical signals need to be transmitted which is eventually turned into observable image via amplification and video processing steps. A schematic of infrared imaging is provided in Figure 1.1. On the other hand, the absorbed radiation causes an increase of temperature that results in changing mechanical and electrical properties of the sensing material in thermal detectors. Bolometers, thermopile and pyroelectric sensors are belong to thermal detector family. Bolometers are resistive elements with small thermal capacity. They may be positive and negative temperature coefficients according to type of temperature resistive sensing element. So, their resistance changes with changing temperature. Response rate of IR sensors is dependent on how fast the sensing layer produces output and it is measured by ROIC.

Photon detectors have generally faster response in comparison with thermal detectors because the formation of moving electrons in photon detectors happens in a shorter time with respect to heating up the detection layer in thermal detectors.

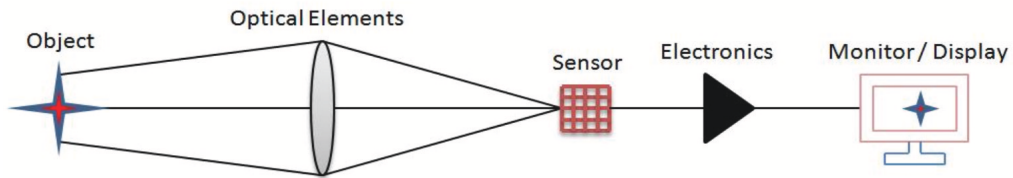


Figure 1.1: Infrared imaging scheme

According to operating temperatures, IR imaging devices can be divided into two groups as cooled and uncooled sensors. Although there exist many differences between cooled and uncooled sensors regarding to sensing materials, microfabrication processes, operation condition performances, device size, weight etc, the main difference is operation temperature of these sensor types that affects the thermo-mechanical behaviour on sensing layers. Uncooled sensors are able to operate around room temperature whereas cooled IR sensors must at cryogenic temperatures, i.e 77K for a generic operation temperature of the cooled IR sensors. For uncooled IR sensors, a lower power consumption is generally adequate. They are smaller in physical dimensions and lighter with respect to cooled IR sensors with proper opto-mechanical package structures. Both of the sensor types have civil and military applications. However the cooled IR sensors are generally preferred if a higher performance is required. Noise equivalent temperature difference (NETD) is a performance metric for IR sensors which defines the sensitivity of sensor. For example, InSb cooled detectors have good sensitivity which means low NETD. Cooled IR detectors have some drawbacks regarding to price, size, weight, mean time between failures (MTBF) etc. General trend in the cooled IR imaging device industry is to increase operation temperature without having performance degradation so that the critical parameters such as power consumption, physical dimensions, weight of the opto-mechanical structure with cryocooler can significantly decrease. To reach cryogenic temperatures with possible minimum cooling power, all of the heat losses in opto-mechanical carrier must be minimized by dealing with two modes of heat transfer (radiation and conduction).

Convection mode of heat transfer is already eliminated with the help of high vacuum environment (10^{-6} to 10^{-9} Torr).

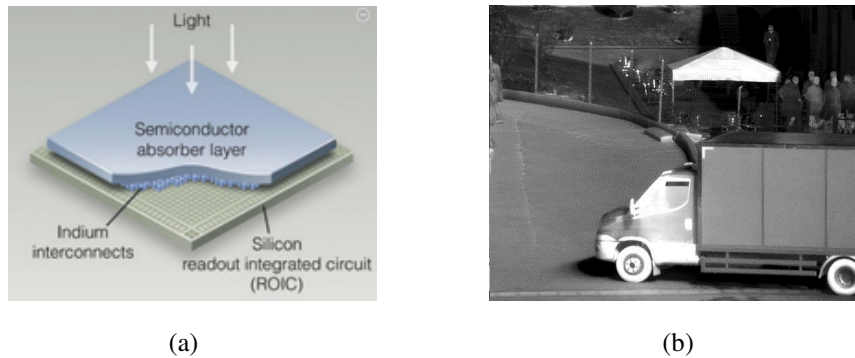


Figure 1.2: a) Representative scheme of IR detector hybrid [2], b) Thermal image of IR sensor

II-VI and III-V semiconductor compounds are widely used as sensing layer materials for IR imaging applications due to their superior structural and opto-electronic properties. The most commonly used semiconductor materials can be listed as CdZnTe, HgTe, HgCdTe, CdTe, ZnTe, InGaAs, InSb, GaAs/AlGaAs, InAs/GaSb (type II superlattices). Epitaxial methods such as MBE, MOCVD, LPE can be used to build the single crystal materials on specific substrates. Different processes must be performed to have an active detection layer for IR imaging which are microfabrication processes, hybridization between focal plane array (FPA) and readout integrated circuit (ROIC), underfilling, integrating hybridized FPA - ROIC couple onto carrier material etc. The arrays that are composed of infrared sensing pixels, is also named as FPA, are located at the focus plane of a lens system in the imaging system architecture. The formed electrical signal in sensing pixels cannot be measured or digitized by FPA itself. This function is performed by ROIC via collecting output signals from FPA with the help of hybridization process that can be named as flip chip bonding [3, 4] . To increase mechanical and thermal stability of the integrated structure, the underfilling [5, 6] is applied between the bonds that interconnects each pixel on FPA to related couple on ROIC. This process is nothing but feeding epoxy material inbetween coupled FPA and ROIC layers. In this way, total thermal and mechanical coupling of the sensing layer to ROIC is achieved. Then, back-end processes such as wirebonding, die bonding,

dicing, grinding can be applied to obtain final geometry. Grinding [7, 8], chemical etching [9] are widely used processes to thinning of materials in semiconductor industry. The obtained IR sensor structure which can also be named as coupled FPA is given in Figure 1.2a for representative purposes. The coupled FPA needs to be placed in a vacuum environment that can be named as opto-mechanical carrier or dewar with proper electrical, mechanical and optical interfaces. IR imaging sensor can be integrated in a opto-electronic system via the opto-mechanical carrier. The coupled FPA is integrated with polymer materials onto opto-mechanical carrier that may contain different types of materials on cooled region such as ceramics, metals, epoxies etc. The term cold region defines a region that reaches cryogenic temperatures during the operation phase of IR sensor whereas its temperature is equal to ambient temperature when the device is not working. So, during operation phase of a cooled IR sensor, these materials given in Figure 1.3 must be cooled down to cryogenic temperatures.

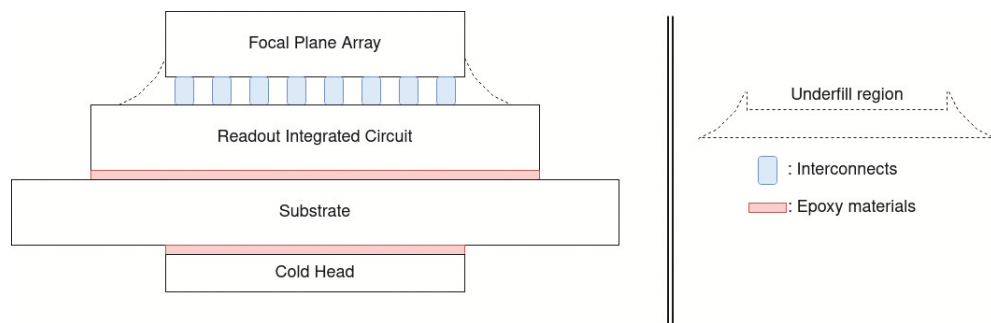


Figure 1.3: Representative schematic of the cold region

Although the lowest exposure temperature for a sensing layer is observed during the operation of a cooled IR sensor, the highest temperature limit is observed generally during crystal growth process for sensing materials. Beyond the crystal growth process, the microfabrication and integration (epoxy cure) processes may require reasonably high temperatures to have residual stresses on IR sensors. The integrated components with FPA may differ in terms of material and dimension. Exposure of temperature change for integrated material assemblies is a routine practice for IR sensor production/operation studies. Thermal expansion coefficient mismatch of constituent materials with cryocooling of the assembly may cause thermo-mechanical stress problems. Opto-electronic properties of semiconductors can also be affected by the deformation and stresses which may cause performance degradation of semicon-

ductor devices. Moreover, a direct mechanical failure of these single crystals can be observed under thermo-mechanical loadings. Using temperature dependent material properties of single crystals play an important role to perform accurate stress-strain predictions. However, obtaining the material properties in a temperature regime from cryogenic temperatures such as 60K to elevated temperatures of 600K is not a trivial task. Experimental methods that can cover such a great temperature difference to obtain thermo-elastic material properties can be very costly and lack of accuracy. The semiconductor materials that are used in IR imaging applications are generally a few microns to a few hundreds of microns in thickness and several millimeters in planar dimensions which makes experimental investigations even harder. In this thesis, Density Functional Theory is used to determine temperature dependent material properties of the selected semiconductors.

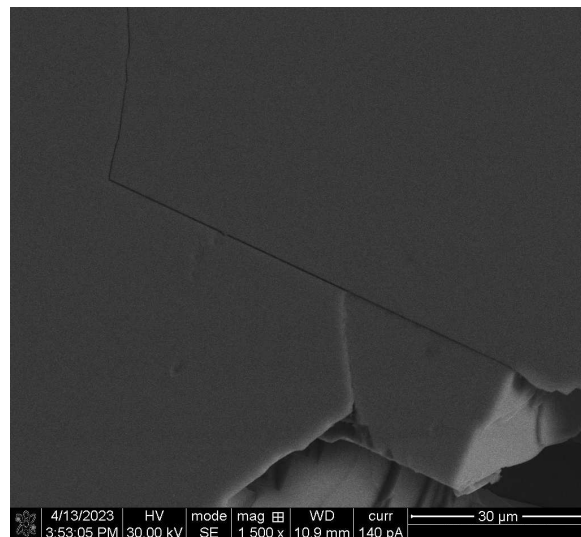


Figure 1.4: Direct mechanical failure of a semiconductor

Mechanical failure is one of the commonly observed problems in opto-electronic devices. However, providing a solution framework for the crack initiation and propagation problems related with the cooled IR imaging sensors is one of the main interests of this thesis. Fractured single crystals or microcracks in IR imaging applications deteriorates electro-optical performance and hence the image quality. These devices expose to harsh environments such as very low temperatures (77K) during operation conditions. However, the storage temperature of the cooled IR sensors is ambient

temperature. During the lifetime of the cooled IR sensors, it is expected to operate between these temperature limits for thousands of cycles without degrading the device performance significantly. Phase field theory for cubic crystal materials is proposed to determine crack initiation and propagation in this thesis.

1.2 Literature Review on Material Properties of III-V and II-VI Semiconductors

DFT is a powerful tool to simulate different types of materials and obtain material properties under different conditions. There are many DFT studies on investigation of structural, electronic, optical material properties on a wide scale in literature. In this thesis, II-VI and III-V semiconductors of GaSb, InSb, CdTe, HgTe, ZnTe and CdZnTe are investigated to obtain thermo-elastic material parameters in a wide temperature range. The upper and lower temperature limits may change according to investigated material due to reaching different temperature limits by applied processes. Extensive literature review is performed to obtain the results of previously performed experiments for the materials that are investigated via DFT. To show the diversity of investigated materials, various papers considering both experimental and numerical studies are referred. Experimental results of the investigated materials in this thesis will be compared with our DFT results later.

Olsson [10] performed first principle investigation to determine temperature dependent elastic constants of zirconium, magnesium and gold via ab initio DFT study and a good coherence is observed with the available experimental results. Shao *et al.* [11] combined the first principle calculations with quasi-harmonic approximation so temperature dependent lattice geometries, coefficient of thermal expansion, elastic constants and ultimate strength of graphene and graphyne are determined. Malica and Dal Corso [12] used *thermo_pw* code to compare quasi-static and quasi-harmonic approaches in investigating temperature dependent elastic constants which is applied to silicon, aluminum and silver materials. It is showed that although quasi-harmonic approach requires a higher computational cost and time, it provides reasonably better accuracy to determine temperature dependent elastic constants. Khanzadeh and Alah-

yarizadeh [13] investigated pressure dependence of mechanical and thermal properties of TiC and ZrC. Wang *et al.* [14] determined temperature dependent elastic constants of rare-earth intermetallic compounds YAg and YCu. Ravindran *et al.* [15] applied DFT to orthorhombic crystals by using both LDA and GGA approximations whereas Pham *et al.* [16] compared atomistic simulations (DFT and Molecular Dynamics (MD)) and ultrasonic measurements for face centered cubic aluminum. Argaman and Makov [17] studied hexagonal closed pack titanium mechanical properties with changing temperature. Third order and second order elastic constants of zinc-blende nitrides AlN, GaN and InN are determined in the study of Lopuzynski and Majewski [18]. Comparison of empirical pseudopotentials and DFT simulations are performed by Lebedeva *et al.* [19] on graphene material.

III-V semiconductor compounds used for infrared sensors are exposed to wide temperature differences during their lifetime. These crystals are typically grown at 1000-1200K [20, 21] whereas cooled IR detectors that use InSb from III-V group as a sensing material typically operates at 77K [22]. Thermomechanical reliability of this class of materials relies heavily on accurate prediction of their stress-strain response across their operating temperatures, which prove difficult via experimental means due to the high cost, the difficulty of measurements at extreme temperatures and the large scatter in the data [23, 24]. A reliable and affordable alternative is the calculation of these properties with quantum mechanical computational methods such as density functional theory (DFT). By now, it has become routine practice to predict zero-temperature elastic constants of crystalline materials within 10% of the experimental results using DFT [25, 26, 27]. The computational tools developed for the extension to finite temperatures have been established in seminal papers [16, 28, 29, 30] although applications have been sparse [31, 32]. Numerical investigations are carried out in order to obtain the theoretical limits of the thermoelastic properties of GaSb and InSb for III-V semiconductor group materials regarding to changing temperature. The results are compared against the available experimental data and extend their range to cover all relevant temperatures. The results will be given in Chapter 3.

Experimentally determined optical properties of antimonide based III-V compounds

have been reported in [33, 34]. GaSb and InSb are both direct band-gap semiconductors with zero-temperature band gaps of 0.67 and 0.18eV [35], respectively. GaSb is widely used in solar cells [36, 37] and photodetector applications [38, 39, 40]. Thermal and elastic properties such as the bulk modulus [41] and the thermal expansion coefficient [42] of GaSb have been the subject of many studies. Al-Douri *et al.* [41] provided bulk modulus of several semiconductors compounds including GaSb. Nilsen *et al.* [43] performed X-ray diffraction measurements to obtain the temperature-dependent thermal expansion of GaSb. Salehi *et al.* [42] reported the elastic constants of antimonide compounds under the effect of pressure. Varshney *et al.* [44] demonstrated the phase transitions of binary antimonide compounds under the effect of pressure and the changes in elastic constants of these materials caused by the phase transitions. InSb is often used by itself or as part of ternary compounds for electro-optical components of the laser structures [45, 46] and infrared photodetectors [47, 48]. Stresses generated by thermal mismatch in InSb infrared focal plane arrays were also investigated [49, 50]. Breivik *et al.* [51] determined the temperature-dependent lattice constants in the range 32-325 °C by using X-ray diffraction measurements and Cai *et al.* [52] reported temperature-dependent thermal properties such as thermal conductivity, coefficient of thermal expansion, thermal diffusivity experimentally in between 300-800K.

Application areas of II-VI semiconductor compounds are infrared detector, laser, light emitting diodes (LEDs), radiation detector applications. Widely used ternary alloys in II-VI semiconductor group in IR imaging applications are mercury cadmium telluride (HgCdTe or MCT) and cadmium zinc telluride (CdZnTe or CZT). Mercury cadmium telluride (MCT) is a promising material that can be used in various infrared ranges of imaging applications due to its superior properties by changing the cadmium concentration i.e, $\text{Hg}_{(1-x)}\text{Cd}_x\text{Te}$ [53, 54, 55]. In addition, CdZnTe (CZT) is a key material as substrate in epitaxial processes of IR imaging devices as well as for solar cell and X-ray detector applications [56, 57, 58, 59]. In this thesis, DFT studies are performed only one ternary alloy which is CZT material from II-VI group materials due to limitations on computational power and time.

Although the growth temperature of these semiconductor compounds can vary with respect to different criterias such as substrate material, growth method, desired defect density, the compounds can expose to temperatures of 200°C-300°C [53, 60, 61, 62]. Zhan *et al.* [63] showed that the cooling of IR sensing layer on Si substrate from growth temperature to operation temperature results in developing thermo-mechanical stresses which affect the focal plane array (FPA) performance that is also valid for CdZnTe substrate material. Gergaud *et al.* [64] investigated lattice parameter measurements of CdZnTe from room temperature up to 300°C by using high resolution X-ray diffraction. Skauli *et al.* [65] also determined experimental lattice constant and thermal expansion coefficients of the ternary compound in the temperature range of 25°C and 110°C for different composition ranges of cadmium. Jacobs *et al.* [66] performed residual thermal stress calculations caused by cooling from growth to room temperature of CdTe film on different substrates, i.e, Si, Ge, GaAs. Elasto-plastic behavior of HgCdTe is determined experimentally via nanoindentation studies by Martyniuk *et al.* [67] and Shkir *et al.* [68] investigated hardness measurements with crack length, fracture determinations of CdZnTe. Irwan *et al.* [69] determined elastic modulus and hardness of HgCdTe as well as showed ductile to brittle transition in terms of depth of cut during diamond cutting of single crystal wafers of this material. There are various studies which investigate electro-optical properties and phonon behaviors of XTe ($X = Hg, Cd, Zn$) binary compounds under different conditions [70, 71, 72, 73, 74, 75]. Cottam and Saunders [76] determined experimental temperature dependent second order elastic constants of HgTe between 2K and 300K. Bagot *et al.* [77] provided experimental thermal expansion coefficient data of CdTe, ZnTe, HgTe. Strauss [78] studied on the physical, including structural, thermal, mechanical, optical and electrical properties of CdTe. Temperature dependent lattice constant and total energy of CdTe is investigated with molecular dynamics by Kanoun *et al.* [79] in the temperature regime of 150K-450K. Yamada *et al.* [80] measured elastic and photoelastic constants of ZnTe by Brillouin scattering at room temperature. Alper and Saunders [81] measured elastic constants of HgTe in the temperature regime of 1.4K to 300K with pulse echo technique.

There are different single crystals from III-V and II-VI groups exposed to great tem-

perature differences which results in arising thermo-mechanical stress on IRFPAs. To ensure performance stability of such opto-electronic devices, investigations of thermo-mechanical stresses are performed in several studies [82, 83, 84]. However, using the temperature dependent material property is rare in these thermo-mechanical stress investigations.

1.3 Literature Review on Phase Field Theory

There are various methods that can be used to determine crack propagation, delamination, fracture on different materials such as eXtended Finite Element Method (XFEM) [85, 86, 87] and Cohesive Zone Method (CZM) [88, 89, 90]. Phase Field Model (PFM) provides good results on where classical fracture mechanics has some limitations such as curvilinear crack paths, branching angles, multiple cracking etc. In this thesis, PFM is used to describe and determine crack propagation on cubic anisotropic materials.

Strength based and energy based criterias are used to determine crack propagation path in the literature. In strength based criteria, a threshold stress or strain level must be reached locally to form micro cracks. Tsai and Hill [91, 92], Tsai and Wu [93] are widely used strength based failure criterias. Difference of the investigated material response in tension and compression is not taken into account in Tsai-Hill criterion. So, the same yield stress is valid both in tension and compression. On the other hand, Tsai-Wu criterion can define different material response according to tension or compression loading mode. Energy based criteria is defined such that formation of new surfaces happens as crack propagates whereas a material point fails in strength based criteria. As introduced by Griffith [94], a crack starts to grow when the energy release rate, G reaches a critical value G_c in energy based Griffith's theory.

Thermodynamically consistent and robust algorithmic implementation of phase field fracture model is provided by Miehe *et al.* [95, 96] in 2010. Then, the phase field fracture models are integrated with multi-physics problems with more seminal papers

[97, 98, 99, 100, 101]. Anisotropic crack phase field is investigated for brittle solids by Li *et al.* [102] and Teichtmeister *et al.* [103]. Nguyen *et al.* [104] and Clayton and Knap [105] investigated phase field modeling for polycrystal materials. Gültekin *et al.* [106] investigated rate dependent anisotropic crack phase-field model for soft biological tissues. Ambati *et al.* [107] provided ductile fracture of elasto-plastic solids in the quasi-static kinematically linear regime. Dal *et al.* [108] also investigated phase field approach to fracture of biological tissues and fiber-reinforced composites. Denli *et al.* [109] provided fracture model of unidirectional fiber reinforced polymer matrix composites with phase field model. Phase field representation of cohesive fracture is determined within energetic framework by Verhoosel and Borst [110]. Fracture of single crystals is also determined by phase field models [111, 112, 113].

1.4 Objective of Thesis

In IR imaging applications, semiconductor materials expose to wide temperature differences due to operation/storage conditions of the devices as well as applied processes to build a functional device. Aerospace and defence industries require high level and long term reliability with exposure of severe temperatures. High-reliability semiconductor market was valued over two billion dollars in 2022 and it is expected to grow in the upcoming years as a result of geopolitical concerns. In the automotive industry, electronic devices are becoming more common. High-reliability components need to be deployed especially for self-driving cars because they help ensure that critical systems and components operate as intended without failure or malfunction, which is essential for maintaining the safety of the vehicle and its occupants. These factors are providing the reasons of the demand growth of the high-reliability semiconductors.

To establish excellent long term reliability of these devices, accurate thermo-mechanical behavior prediction of semiconductor materials is vital. However, the temperature dependent material properties is not available in literature that covers cryogenic as well as elevated temperatures. Experimental methods to determine the material properties require great costs and provide less accurate results. As a numerical alternative to obtain temperature dependent material properties, Density Functional Theory (DFT) is proposed for single crystal materials that are commonly used in IR imaging applications. Investigation of elastic modulus and hardness on GaSb material is also performed via nanoindentation experiments at room temperature to check the validity of DFT simulation results. Besides GaSb, InSb, CdTe, HgTe, ZnTe and CdZnTe semiconductors have been investigated with DFT. Direct mechanical failure can be observed on semiconductor compounds due to harsh temperatures and thermal expansion mismatch of the materials. Phase Field (PF) model for cubic anisotropic fracture is proposed. Fracture on cubic single crystal GaSb due to mechanical loading, i.e, uniaxial tension of notched plate is investigated by using developed model and obtained material properties by DFT. So, quantum mechanical material modelling studies are combined with phase field fracture model in this thesis. Investigated sin-

gle crystals are mostly binary compounds from III-V and II-VI groups that show cubic symmetry. Experimental observation of crack propagation paths on GaSb and CdZnTe semiconductor materials are performed with a custom test setup that is designed to operate at cryogenic temperatures that simulates the operation condition of cooled IR sensor. By using thermal expansion mismatch of different materials, i.e, semiconductors and stainless steel, the crack initiation and propagation on selected single crystal materials are observed experimentally. Scanning Electron Microscopy (SEM) is used to observe fracture patterns. Main motivation of this thesis is to provide a complete framework starting from material property determinations in desired temperature regime and cover crack initiation, propagation of semiconductor materials with both numerical and experimental investigations.

In Chapter 2, fundamantels of Density Functional Theory and Phase Field Theory are provided. Thermal, elastic as well as opto-electronic properties of selected materials are given by DFT simulations in Chapter 3. Experimental investigations regarding nanoindentation tests, test setup design, cryocooling experiments and crack observations on semiconductors are provided in Chapter 4. Effect of temperature dependent material property on thermo-mechanic stress predictions of semiconductor materials as well as IRFPA structure are given with finite element simulations in Chapter 5. Then, Chapter 6 covers theory, method and computational details of Phase Field Theory to model crack propagation in cubic anisotropic materials. Summary of the investigated studies and concluding remarks with future work are determined in Chapter 7.

CHAPTER 2

FUNDAMENTALS OF DENSITY FUNCTIONAL THEORY AND PHASE FIELD THEORY

2.1 Basic Concepts of Density Functional Theory

Density Functional Theory (DFT) is a quantum mechanical modelling method of solving many body systems, in particular atoms, molecules and condensed matter systems. The condensed matter is a definition of matter whose energy is low enough to form stable systems of molecules, atoms generally in liquid and solid phases. Software packages are able to provide open source codes to calculate various material properties of different types of materials by using DFT. In general, one can simulate mechanical, electrical or optical properties of a material as long as the atomic or molecular structure of the material defined properly. There are some alternatives to DFT formulations which include Quantum Monte-Carlo (QMC) [114][115][116] and configuration interaction (CI) [117] methods.

Ab initio, first principle, approach aims to model a material without using any experimental input by defining its atomic, molecular structure including the definition of positively charged nucleus, a number of negatively charged electrons and the interaction between atoms. The interaction between the atoms includes interactions between electron and electron, nucleus and nucleus, electron and nucleus. When these interactions can be defined accurately, the first principle approach can define more complex phenomena called as many body Schrödinger equation.

2.1.1 Schrödinger equation

Schrödinger Equation, which is essentially a wave equation, describes the probability of wave functions that defines motion and behaviour of small particles. One can obtain information about physical properties of systems by solving many-body Schrödinger equation.

Many Body Schrödinger Equation which is given below uses kinetic energy of nuclei and electrons as well as electrostatic interactions between nucleus-nucleus and electron-electron. In equation 2.1, the Hamiltonian is defined with \hat{H} where total energy is given as E and the many-body wavefunction for N electronic eigenstates is represented by Ψ . The Hamiltonian given in equation 2.2 includes the kinetic energy of nuclei and electrons, nucleus-nucleus and electron-electron repulsions as well as the electron-nuclei interaction. In equation 2.2, R and r represent the coordinates of nuclei and electrons, mass and charge of the I -th nucleus are M_I and Z_I and electronic mass and charge are represented with m_e and $-e$, respectively. Ψ , the wavefunction is defined to be a function describing the probability of a particle's quantum state as a function of position, momentum, time and spin. All possible system information can be found in the wavefunction. Exact solution of many-body Schrödinger equation is not possible for particles more than two or atoms heavier than hydrogen. However, approximate solution for many-body Schrödinger equation can be performed. The exact solution of this equation requires great amount of speeds and memory of computers which is not practically possible today.

$$\hat{H}\Psi(r, R) = E\Psi(r, R) \quad (2.1)$$

$$\hat{H} = -\sum_{I=1}^{N_I} \frac{\hbar^2}{2M_I} \nabla_{R_I}^2 - \sum_{i=1}^{N_e} \frac{\hbar^2}{2m_e} \nabla_{r_i}^2 + \frac{1}{2} \sum_{I \neq J} \frac{Z_I Z_J e^2}{|R_I - R_J|} + \frac{1}{2} \sum_{i \neq j} \frac{e^2}{|r_i - r_j|} - \sum_{i,I} \frac{Z_I e^2}{|r_i - R_I|} \quad (2.2)$$

The terms in equation 2.2 can be defined as

$$\mathcal{T}_n = - \sum_{I=1}^{N_I} \frac{h^2}{2M_I} \nabla_{R_I}^2 \quad (2.3)$$

where \mathcal{T}_n is the kinetic energy of nuclei,

$$\mathcal{T} = - \sum_{i=1}^{N_e} \frac{h^2}{2m_e} \nabla_{r_i}^2 \quad (2.4)$$

where \mathcal{T} is the electron kinetic energy,

$$\mathcal{V}_n = \frac{1}{2} \sum_{I \neq J} \frac{Z_I Z_J e^2}{|R_I - R_J|} \quad (2.5)$$

where \mathcal{V}_n is the nuclei-nuclei interaction,

$$\mathcal{V} = \frac{1}{2} \sum_{i \neq j} \frac{e^2}{|r_i - r_j|} \quad (2.6)$$

where \mathcal{V} is the electron-electron interaction,

$$\mathcal{V}_{ext} = - \sum_{i,I} \frac{Z_I e^2}{|r_i - R_I|} \quad (2.7)$$

where \mathcal{V}_{ext} defines the interaction term between electrons and nuclei that can also be defined as external potential for electrons. The Hamiltonian of the many-body system can also be represented as

$$\hat{H} = \mathcal{T}_n + \mathcal{T} + \mathcal{V}_n + \mathcal{V} + \mathcal{V}_{ext} \quad (2.8)$$

With *Born-Oppenheimer approximation*, it is assumed that motion of the electrons and nuclei can be separated due to heavy mass of nuclei in comparison to electrons. Motion of the nuclei is much slower than the electron that results in having a fixed position of the nuclei, so the kinetic energy of the nuclei which is given in equation 2.3 can be neglected. By using Born-Oppenheimer approximation, the system's degrees

of freedom are reduced such that the interactions between nuclei, \mathcal{V}_n in equation 2.5 can be treated as constant value.

Pseudopotential approximation used in DFT to simplify the calculation of the electronic wavefunction. In a pseudopotential calculation, the core electrons (those that are tightly bound to the nucleus) are replaced with an effective potential that includes the average effect of the core electrons on the valence electrons. This reduces the number of electrons that need to be explicitly included in the calculation, which makes the calculation more computationally efficient [118, 119, 120]. For further reading about pseudopotentials, it is referred to Singh and Nordström [121].

Relativistic pseudopotentials are effective potentials that replace the full relativistic Hamiltonian in the DFT calculations. These potentials are constructed by separating the core electrons from the valence electrons, and then replacing the core electrons with a pseudopotential that incorporates the relativistic effects. The use of relativistic pseudopotentials is important for accurately modeling heavy elements, as the relativistic effects become more significant as the atomic number increases.

2.1.2 Hohenberg-Kohn theorems

Hohenberg-Kohn theorems are two foundational theorems in DFT. The first theorem states that the ground-state electronic density of a many-electron system uniquely determines the external potential of the system. The second theorem states that there exists a universal functional of the electronic density that gives the total energy of the system. The minimum value of the energy functional that encompasses all possible electron densities represents the lowest possible energy state of the system, which is called the ground state energy. The electron density that corresponds to this minimum energy state is known as the ground state density. Together, these theorems provide the theoretical framework for DFT, which enables efficient and accurate calculations of the electronic structure of materials. [122].

In principle, all properties of the system are exact functionals of the ground state electron density, $E[\rho_{GS}]$. Energy functional, $E[\rho]$ is expressed as in equation 2.10

$$E_{GS} = E[\rho_{GS}] \quad (2.9)$$

$$E[\rho] = F[\rho] + V_{ext} + \mathcal{V}_n \quad (2.10)$$

where $F[\rho]$ is system internal energy composed of electron kinetic, potential and interaction energies.

$$F[\rho] = T[\rho] + E_{int}[\rho] \quad (2.11)$$

Hohenberg and Kohn [122] states that true ground state density for the external potential, V_{ext} is the density that minimizes the energy. the external potential energy is given by

$$V_{ext} = \int d\mathbf{r} v_{ext}(\mathbf{r})\rho(\mathbf{r}) \quad (2.12)$$

When the system internal energy, $F[\rho]$ is known, the ground state electron density, ρ_{GS} can be determined by minimizing the energy functional, $E[\rho]$.

2.1.3 Kohn-Sham method

Kohn-Sham method [123] is a formulation of DFT which finds a good approximation to internal electronic energy, F , by defining a set of component energies that sum to give F . It approximates the true many electron system (*interacting*) by using *non-interacting* systems. It assumes that the true ground state density is also ground state density of *non-interacting* system. The Kohn-Sham method effectively separates the exchange-correlation energy, which accounts for electron-electron interactions, from the kinetic and external potential energies, making it computationally feasible for larger systems. The Kohn-Sham equations are typically solved self-consistently, iteratively adjusting the electron density until a stable solution is reached.

The Schrödinger-like equation for the Kohn-Sham orbitals is given as

$$\hat{H}_{KS}[\rho]\phi_i(\mathbf{r}) = \epsilon_i\phi_i(\mathbf{r}) \quad (2.13)$$

where \hat{H}_{KS} is the Kohn-Sham Hamiltonian, ρ is the electron density, ϕ_i is the i th Kohn-Sham orbital, ϵ_i is the corresponding eigenvalue or energy of the i th orbital, and \mathbf{r} represents position as given before. The expression for the electron density can be given as

$$\rho(\mathbf{r}) = \sum_i^N |\phi_i(\mathbf{r})|^2 \quad (2.14)$$

where the number of electrons is defined with N . The Kohn-Sham Hamiltonian, \hat{H}_{KS} , can be defined as

$$\hat{H}_{KS}[\rho] = -\frac{\hbar^2}{2m_e}\nabla^2 + V_{KS}(\mathbf{r}) \quad (2.15)$$

where V_{KS} is the Kohn-Sham potential, which consists of the external potential, Hartree potential and exchange-correlation potential given as

$$V_{KS}(\mathbf{r}) = V_{ext}(\mathbf{r}) + V_{Hartree}(\mathbf{r}) + V_{xc}(\mathbf{r}) \quad (2.16)$$

with the definitions of Hartree potential

$$V_{Hartree}(\mathbf{r}) = \int \frac{\rho(\mathbf{r}')}{|\mathbf{r} - \mathbf{r}'|} d\mathbf{r}' \quad (2.17)$$

and exchange-correlation potential which accounts for the effects of electron exchange and correlation on the electron density.

$$V_{xc}(\mathbf{r}) = \frac{\delta E_{xc}[\rho]}{\delta \rho(\mathbf{r})} \quad (2.18)$$

Lets summarize the Kohn-Sham procedure for self-consistency;

1. Choose an initial guess for the electron density, $\rho(\mathbf{r})$.

2. Use the electron density to calculate the Kohn-Sham potential, $V_{KS}(\mathbf{r})$, in equation 2.16.
3. Use the Kohn-Sham potential to solve for the Kohn-Sham orbitals, $\phi_i(\mathbf{r})$, using the Schrödinger-like equation 2.13
4. Calculate the electron density from the Kohn-Sham orbitals in equation 2.14
5. Check for self-consistency by comparing the new electron density with the previous guess. If the difference is below a certain tolerance, the calculation is considered converged. If not, repeat steps 2-4 using the new electron density until the convergence is achieved

The self-consistency procedure involves iteratively solving the Kohn-Sham equations until the electron density converges to a stable solution. In step 2, the exchange-correlation potential is calculated using the current electron density and the functional derivative of the exchange-correlation energy. In step 3, the Kohn-Sham orbitals are solved for using the Kohn-Sham Hamiltonian, which includes the Kohn-Sham potential. In step 4, the electron density is calculated from the Kohn-Sham orbitals. Finally, in step 5, the electron density is checked for self-consistency, and the procedure is repeated until convergence is achieved.

2.1.4 Approximations for exchange-correlation energy, E_{xc}

Exchange-Correlation energy the component of the total energy in density functional theory that accounts for the effects of electron exchange and electron correlation. The exchange energy is a component of the electron-electron interaction potential energy that arises from the Pauli exclusion principle. It is a quantum mechanical effect that arises because two identical fermions (such as electrons) cannot occupy the same quantum state simultaneously. The exchange energy is therefore a penalty for two electrons occupying the same quantum state, and it is a key factor in determining the electronic structure of a system. On the other hand, the correlation energy is a measure of the additional energy required to account for the fact that the electron-electron interaction potential energy is not simply the sum of pairwise interactions between electrons, but also includes more complex many-body interactions that arise from the

correlated motion of electrons. There are empirical [124, 125] and non-empirical [126, 127] density functional approximations that are used to approximate exchange correlation functional, $E_{xc}[\rho]$, given in equation 2.18. To obtain empirical pseudopotentials, some of the information should be derived from the experiments whereas non-empirical pseudopotentials are derived from the results of first principle calculations without requirement of any experimental data. Local density approximation (LDA) and generalized gradient approximation (GGA) are commonly used density functional approximations to approximate the exchange-correlation energy in DFT calculations.

2.1.4.1 Local density approximation, LDA

LDA [122] assumes that the exchange-correlation energy density is a function of the electron density at each point in space. This approximation is valid for slowly varying electron densities and is based on the assumption that the electron density at each point in space is uniform. Exchange-correlation energy expression for LDA is given as

$$E_{xc}^{LDA}[\rho] = \int \rho(\mathbf{r}) \epsilon_{xc}^{LDA}(\rho(\mathbf{r})) d\mathbf{r} \quad (2.19)$$

where $\epsilon_{xc}^{LDA}(\rho)$ is the LDA exchange-correlation energy per particle as a function of the electron density $\rho(\mathbf{r})$. LDA often provides good results for structural, vibrational, elastic properties for a wide range of solid state systems.

2.1.4.2 Generalized gradient approximation, GGA

GGA [128] is a more sophisticated version with respect to LDA that includes additional terms to improve the accuracy of the approximation.

$$E_{xc}^{GGA}[\rho] = \int \rho(\mathbf{r}) \epsilon_{xc}^{GGA}(\rho(\mathbf{r}), \nabla \rho(\mathbf{r})) d\mathbf{r} \quad (2.20)$$

where $\epsilon_{xc}^{GGA}(\rho, \nabla \rho)$ is the GGA exchange-correlation energy per particle as a function of the electron density $\rho(\mathbf{r})$ and its gradient $\nabla \rho(\mathbf{r})$. GGA provides improved description of stability of bulk phases, molecular structures and representation of weak inter-molecular bonds.

PBESol is a type of generalized gradient approximation (GGA) in DFT that is often used to calculate the electronic properties of solids. PBESol is a variant of the PBE (Perdew-Burke-Ernzerhof) GGA [128], which was originally developed to calculate the electronic properties of molecules.

The main difference between PBE and PBESol is the way in which they treat the exchange-correlation energy in the GGA. PBESol uses a modified form of the exchange part of the GGA that is designed to improve the description of the cohesive properties of solids, while maintaining the accuracy of PBE for molecular systems. Specifically, PBESol includes a scaling factor that reduces the amount of exchange in the GGA, which leads to a more accurate description of the bulk properties of solids. PBESol has been shown to be a reliable and accurate method for calculating the electronic properties of a wide range of solids, including metals, semiconductors, and insulators. In this thesis, LDA and PBESol approximations are used to obtain bulk material properties of semiconductor materials.

$$E_{xc}^{PBESol}[\rho] = \int \rho(\mathbf{r}) \epsilon_{xc}^{PBESol}(\rho(\mathbf{r}), \nabla \rho(\mathbf{r})) d\mathbf{r} \quad (2.21)$$

where $\epsilon_{xc}^{PBESol}(\rho, \nabla \rho)$ is the PBESol exchange-correlation energy per particle as a function of the electron density $\rho(\mathbf{r})$ and its gradient $\nabla \rho(\mathbf{r})$. The exact expression for ϵ_{xc}^{PBESol} is quite lengthy and involves multiple terms, but it can be found in Perdew *et al.* [129].

Other types of non-empirical density functional approximations include meta-GGAs, hybrid functionals, range-separated functionals [130, 131, 132]. These approximations are widely used in materials science, chemistry and physics to study a variety of

systems, ranging from molecules to solids and surfaces.

2.1.5 Tools for *ab initio* calculations

To perform *ab initio* calculations, specialized software tools that can handle quantum mechanical calculations are required. The most commonly used tools for *ab initio* calculations are ;

- Quantum Espresso

Quantum Espresso (QE) [133, 134] is an open source package. QE contains implementations of Density Functional Perturbation Theory (DFPT). One has to choose the correct pseudopotential for QE as there are different pseudopotentials for the same element. One can use Quantum Espresso to calculate first principles and also linear response calculations [135]. Since it is open source, implementation of new methods can be quicker for QE.

- Vienna Ab initio Simulation Package (VASP)

VASP is a commercial code. Generally, it is faster than QE and ABINIT tools as shown in some benchmark studies. There are well tested pseudopotential library for VASP package. On the other hand, it uses third party packages for density functional perturbation theory.

- MedeA

MedeA contains different software packages to perform wide range of calculations. It contains VASP with proper graphical user interface (GUI) to perform DFT calculations. Moreover, Large-scale Atomic/Molecular Massively Parallel Simulator (LAMMPS), Grand Canonical Monte Carlo method for fluids (GIBBS) and semi-empirical quantum chemistry method for fast property prediction and screening (MOPAC) are some software features with proper GUIs on MedeA. In this thesis, DFT calculations are performed with MedeA VASP package [136].

Some other tools for DFT calculations can be listed as CASTEP [137], CPMD

[138], ABINIT [139].

2.2 Basic Concepts of Continuum Mechanics

Fundamental concepts of continuum mechanics i.e, the basic relations of motion of a body, geometric mappings, kinematics stress measures and balance laws are given in this section. For further reading, one can use the following seminal books by Holzapfel [140], Marsden & Hughes [141], Ogden [142]

Let the solid body at time $t_0 \in \mathcal{T} \subset \mathbb{R}_+$ be referred to as the reference configuration in the three-dimensional Euclidean space $\mathcal{B} \subset \mathbb{R}^3$. The spatial or current configuration of the body, $\mathcal{S} \subset \mathbb{R}^3$, is defined at current time $t \in \mathcal{T} \subset \mathbb{R}_+$. The material point $\mathbf{X} \in \mathcal{B}$ is mapped with the deformation map, $\varphi_t(\mathbf{X})$ onto the spatial point $\mathbf{x} \in \mathcal{S}$

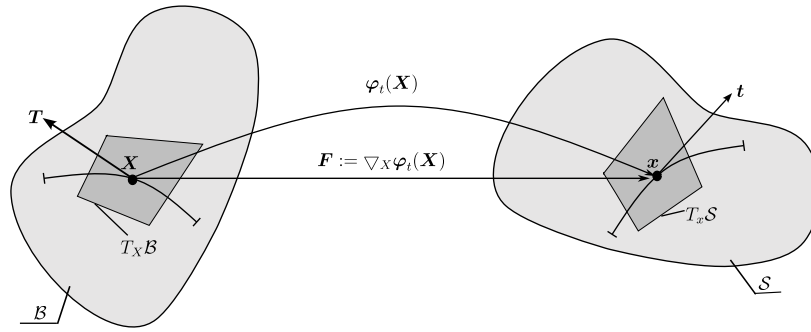


Figure 2.1: The deformation gradient \mathbf{F} is defined as a linear tangent map that transforms the material tangent vector, $\mathbf{T} \in T_{\mathbf{X}}\mathcal{B}$ onto the spatial tangent vector, $\mathbf{t} \in T_{\mathbf{x}}\mathcal{S}$

$$\varphi_t(\mathbf{X}) : \begin{cases} \mathcal{B} \times \mathcal{T} \rightarrow \mathcal{S} \\ (\mathbf{X}, t) \mapsto \mathbf{x} = \varphi(\mathbf{X}, t), \end{cases} \quad (2.22)$$

The deformation map, $\varphi_t(\mathbf{X})$ characterizes the motion of the solid body. In this framework, the velocity and acceleration of the reference configuration are introduced as

$$\mathbf{V}_t(\mathbf{X}) := \partial_t \varphi(\mathbf{X}, t) = \frac{d}{dt} \varphi_{\mathbf{X}}(t), \quad \mathbf{A}_t(\mathbf{X}) := \partial_t \mathbf{V}(\mathbf{X}, t) = \frac{d}{dt} \mathbf{V}_{\mathbf{X}}(t) \quad (2.23)$$

On the other hand, the spatial velocity and acceleration are defined

$$\mathbf{v}_t(\mathbf{x}, t) := \mathbf{V}_t(\mathbf{X}) \circ \varphi_t^{-1}(\mathbf{x}), \quad \mathbf{a}_t(\mathbf{x}, t) := \mathbf{A}_t(\mathbf{X}) \circ \varphi_t^{-1}(\mathbf{x}) = \partial_t \mathbf{v} + \nabla_{\mathbf{x}} \mathbf{v} \cdot \mathbf{v} \quad (2.24)$$

The reference \mathcal{B} and spatial \mathcal{S} configurations are continuous three-dimensional manifolds parametrized locally in the neighborhoods $\mathcal{N}_X \subset \mathcal{B}$ and $\mathcal{N}_x \subset \mathcal{S}$ by overlapping coordinate charts $\{X^A\}_{A=1,2,3}$ and $\{x^a\}_{a=1,2,3}$, respectively. The deformation gradient that maps tangents, $\mathbf{T} \in T_X \mathcal{B}$ of material curves onto tangents, $\mathbf{t} \in T_x \mathcal{S}$ of spatial curves is defined as

$$\mathbf{F} := \nabla_X \varphi_t(\mathbf{X}) \quad \text{with} \quad F_A^a = \frac{\partial x^a}{\partial X^A}, \quad (2.25)$$

Basic mapping relations for line, area and volume mapping can be defined as follows,

$$d\mathbf{x} = \mathbf{F} d\mathbf{X}, \quad d\mathbf{a} = \text{cof } \mathbf{F} d\mathbf{A}, \quad dv = J dV \quad (2.26)$$

with infinitesimal reference line, area, volume elements $d\mathbf{X}, d\mathbf{A}, dV \in \mathcal{B}$ and related spatial elements $d\mathbf{x}, d\mathbf{a}, dv \in \mathcal{S}$. J , determinant of the deformation gradient, maps infinitesimal reference volume element onto the associated spatial volume element, i.e., $J := \det \mathbf{F} > 0$. The cofactor, $\text{cof}[\mathbf{F}] := J\mathbf{F}^{-T}$ of the deformation gradient, \mathbf{F} maps area vectors of material surfaces onto area vectors of the associated spatial surfaces. Similarly, the deformation gradient, \mathbf{F} maps material line elements onto its spatial counterpart as given in equation 2.26.

To furnish coordinate systems in both Lagrangian or reference and Eulerian or spatial configurations at hand, the two manifolds regarding to material, \mathcal{B} and spatial, \mathcal{S} states equipped with the symmetric and positive definite covariant reference \mathbf{G} and spatial \mathbf{g} metric tensors. The metric tensors reduce to the Kronecker deltas, i.e., $G_{AB} = \delta_{AB}$ and $g_{ab} = \delta_{ab}$ in the Cartesian coordinate system. The metric tensors link the tangent and co-tangent spaces

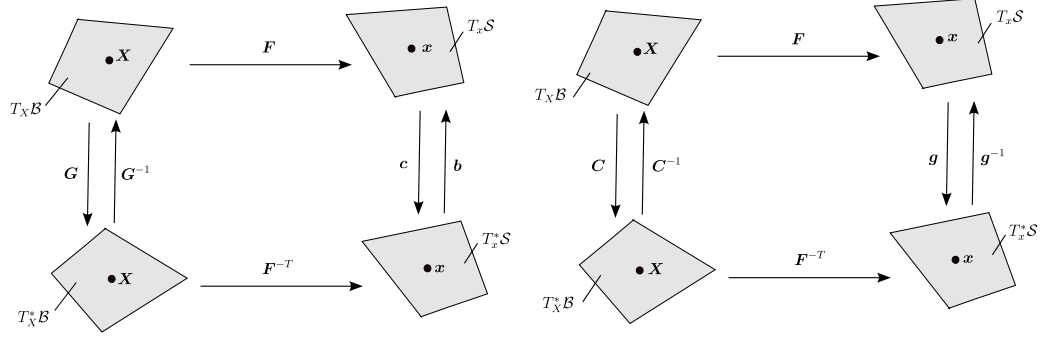


Figure 2.2: a) Push-forward, b) Pull-back operations

$$\mathbf{G} : \begin{cases} T_X \mathcal{B} \rightarrow T_X^* \mathcal{B} \\ \mathbf{T} \mapsto \mathbf{N} = \mathbf{G}\mathbf{T} \end{cases}, \quad \mathbf{g} : \begin{cases} T_X \mathcal{S} \rightarrow T_X^* \mathcal{S} \\ \mathbf{t} \mapsto \mathbf{n} = \mathbf{g}\mathbf{t} \end{cases} \quad (2.27)$$

Figure 2.2 shows the push forward, $\varphi_*(\bullet)$ operations on the covariant metric \mathbf{G} and the contravariant inverse metric \mathbf{G}^{-1} producing the left Cauchy-Green tensor \mathbf{b} along with its inverse $\mathbf{b}^{-1} = \mathbf{c}$

$$\begin{aligned} \mathbf{b} &:= \varphi_*(\mathbf{G}^{-1}) = \mathbf{F}\mathbf{G}^{-1}\mathbf{F}^T, \\ \mathbf{c} = \mathbf{b}^{-1} &:= \varphi_*(\mathbf{G}) = \mathbf{F}^{-T}\mathbf{G}\mathbf{F}^{-1}, \end{aligned} \quad (2.28)$$

Similarly, the pull-back, $\varphi^*(\bullet)$ operations on the covariant metric \mathbf{g} and the contravariant inverse metric \mathbf{g}^{-1} leading to right Cauchy-Green tensor \mathbf{C} along with its inverse \mathbf{C}^{-1}

$$\begin{aligned} \mathbf{C} &:= \varphi^*(\mathbf{g}) = \mathbf{F}^T\mathbf{g}\mathbf{F} \\ \mathbf{C}^{-1} &:= \varphi^*(\mathbf{g}^{-1}) = \mathbf{F}^{-1}\mathbf{g}^{-1}\mathbf{F}^{-T} \end{aligned} \quad (2.29)$$

2.2.1 Stress measures

Lagrangian and Eulerian tangent vectors have been given in Figure 2.4 such that the vector $\mathbf{t} \in T_x \mathcal{S}$ is the true traction action on the deformed surface da of $\partial \mathcal{P}_S$. The Cauchy stress theorem postulates

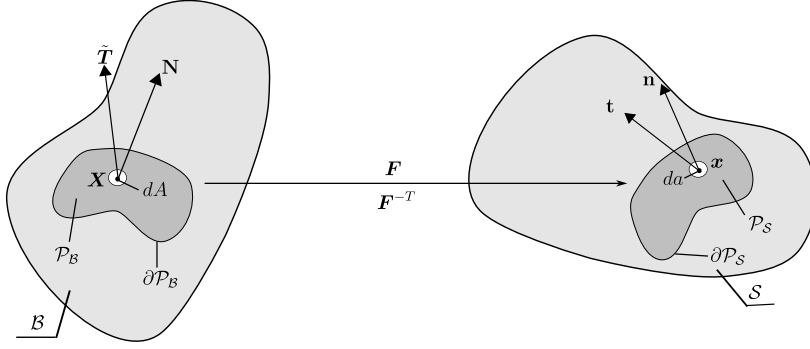


Figure 2.3: Lagrangian $\tilde{T}(\mathbf{X}, t; \mathbf{N}) \in T_X \mathcal{B}$ and Eulerian $\mathbf{t}(\mathbf{x}, t; \mathbf{n}) \in T_x \mathcal{S}$ traction vectors on cut out parts of reference and deformed surfaces $\partial \mathcal{P}_B$ and $\partial \mathcal{P}_S$, respectively.

$$\mathbf{t}(\mathbf{x}, t; \mathbf{n}) := \boldsymbol{\sigma}(\mathbf{x}, t) \mathbf{n} \quad \text{with} \quad t^a = \sigma^{ab} n_b \quad (2.30)$$

with the spatial traction vector $\mathbf{t} \in T_x \mathcal{S}$ and spatial normal vector $\mathbf{n} \in T_x^* \mathcal{S}$ of the surface. The Cauchy stress tensor is dependent on the actual force and the actual deformed area. Kirchoff stress tensor, $\boldsymbol{\tau}$, and first Piola-Kirchoff stress tensor, \mathbf{P} are defined as follows

$$\boldsymbol{\tau} := J \boldsymbol{\sigma} \quad (2.31)$$

$$\mathbf{P} = J \boldsymbol{\sigma} \mathbf{F}^{-\text{T}} = \boldsymbol{\tau} \mathbf{F}^{-\text{T}} \quad (2.32)$$

Similarly, the relation between material traction vector \tilde{T} and material normal vector \mathbf{N} is established by the second Piola-Kirchoff stress tensor \mathbf{S} which is a symmetric, purely Lagrangian object

$$\tilde{T}(\mathbf{X}, t; \mathbf{N}) = \mathbf{S}(\mathbf{X}, t) \mathbf{N} \quad (2.33)$$

The mappings between tangential and cotangential spaces of Lagrangian and Eulerian manifolds for stress tensors are summarized in Figure 2.4. First Piola-Kirchoff,

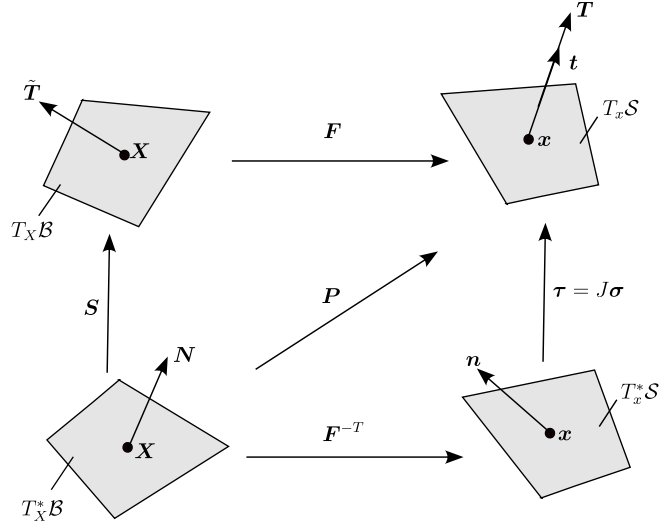


Figure 2.4: The push-forward and pull-back operations on stress measures corresponding to their covariant and contravariant representations.

second Piola-Kirchoff and Kirchoff stress tensors can be related with each other from the pull-back, push forward relations as summarized in Figure 2.4

$$\begin{aligned} \mathbf{S} &:= \mathbf{F}^{-1} \mathbf{P} \\ \mathbf{S} &:= \mathbf{F}^{-1} \boldsymbol{\tau} \mathbf{F}^{-\text{T}} \end{aligned} \quad (2.34)$$

$$\begin{aligned} \boldsymbol{\tau} &:= \mathbf{P} \mathbf{F}^{\text{T}} \\ \boldsymbol{\tau} &:= \mathbf{F} \mathbf{S} \mathbf{F}^{\text{T}} \end{aligned} \quad (2.35)$$

or first Piola-Kirchoff stress tensor can also be represented in terms of Kirchoff stress $\mathbf{P} = \boldsymbol{\tau} \mathbf{F}^{-\text{T}}$ or Cauchy stress tensor, $\mathbf{P} = J \boldsymbol{\sigma} \mathbf{F}^{-\text{T}}$. The first-Piola Kirchoff stress tensor measures the stress with regard to the undeformed cut surface, $\partial \mathcal{P}_B$

2.2.2 Stress power and dual variables

The Kirchoff stress tensor $\boldsymbol{\tau}$ and the second Piola-Kirchoff stress tensor \mathbf{S} are dual objects just as dual Eulerian metrics \mathbf{g} and \mathbf{C} . Dual geometric objects in Eulerian and Lagrangian configurations that characterize strain and stress are (\mathbf{S}, \mathbf{C}) and $(\boldsymbol{\tau}, \mathbf{g})$. In stress power, these dualities are used as work-conjugate objects. In the reference

configuration, the stress power per unit volume is defined as $\mathcal{P} := \mathbf{S} : \dot{\mathbf{E}}$ can be reformulated with $\dot{\mathbf{E}} = \frac{1}{2}\dot{\mathbf{C}}$ as

$$\mathcal{P} := \mathbf{S} : \frac{1}{2}\dot{\mathbf{C}} \quad (2.36)$$

The rate of right Cauchy Green tensor \mathbf{C} can be given in terms of the Green strain rate tensor $\dot{\mathbf{E}}$. The push forward of the equation 2.36 results in Eulerian configuration with the dual variables of the Kirchoff stress tensor $\boldsymbol{\tau}$ and Eulerian metric \mathbf{g} .

$$\mathcal{P} := \boldsymbol{\tau} : \mathfrak{L}_v e = \boldsymbol{\tau} : \frac{1}{2} \mathfrak{L}_v \mathbf{g} = \boldsymbol{\tau} : \mathbf{d} \quad (2.37)$$

Lie-derivative \mathfrak{L}_v defines the Oldroyd-type rates of the Eulerian tensor fields in three steps

- Pull back of the Eulerian object to the time-invariant Lagrangian setting
- Material time derivation of the Lagrangian object
- Push forward the resulting quantity to the Eulerian configuration

For example, the application of the Lie-derivative to the current metric \mathbf{g} results in the rate of deformation tensor, \mathbf{d}

$$\mathfrak{L}_v \mathbf{g} := \mathbf{F}^{-T} \frac{d}{dt} (\mathbf{F}^T \mathbf{g} \mathbf{F}) \mathbf{F}^{-1} = \mathbf{g} \mathbf{l} + \mathbf{l}^T \mathbf{g} = 2 \text{sym}(\mathbf{g} \mathbf{l}) = 2\mathbf{d} \quad (2.38)$$

with the definition of spatial velocity gradient, $\mathbf{l} := \nabla_x \mathbf{v} = \dot{\mathbf{F}} \mathbf{F}^{-1}$. Two-point, Lagrangian and Eulerian geometric settings for the stress power can be expressed as

$$\mathcal{P} := \mathbf{g} \tilde{\mathbf{P}} : \dot{\mathbf{F}} = \mathbf{S} : \frac{1}{2}\dot{\mathbf{C}} = \boldsymbol{\tau} : \frac{1}{2} \mathfrak{L}_v \mathbf{g} \quad (2.39)$$

2.2.3 Balance laws

Balance of mass, balance of linear and angular momentum, first and second law of thermodynamics are the fundamental axioms of thermomechanics for the primary field variables. A defined special volume \mathcal{P}_S is enclosed by a smooth boundary $\partial\mathcal{P}_S$ as given in Figure 2.3. The balance relations are determined according to the volumetric source and the surface flux terms by considering the temporal change of the related quantity.

Balance of mass

A fundamental physical property of any material is mass. The mass density of referential and spatial configurations can be defined as $\rho_0(\mathbf{X})$ and $\rho(\mathbf{x}, t)$. Conservation of the mass states that the total mass of special volume \mathcal{P}_S remains constant that requires

$$\frac{d}{dt}\mathcal{M} := \frac{d}{dt} \int_{\mathcal{P}_S} \rho(\mathbf{x}, t)dv = \frac{d}{dt} \int_{\mathcal{P}_B} J\rho(\mathbf{x}, t)dV = \frac{d}{dt} \int_{\mathcal{P}_B} \rho_0(\mathbf{X}, t)dV = 0 \quad (2.40)$$

This yields the local Eulerian form of mass balance equation

$$\dot{\rho} + \rho \operatorname{div} \mathbf{v} = 0 \quad \text{and} \quad J\rho(\mathbf{x}, t) = \rho_0(\mathbf{X}, t) \quad (2.41)$$

Balance of linear momentum

The linear momentum, \mathcal{I} of the part \mathcal{P}_S is given by $\mathcal{I} = \int_{\mathcal{P}_S} \rho\mathbf{v}(\mathbf{x}, t)dv$ and the resulting forces i.e, the sum of volume specific body forces and the forces on the surface $\int_{\mathcal{P}_S} \rho\boldsymbol{\gamma}(\mathbf{x}, t)dv + \int_{\partial\mathcal{P}_S} \mathbf{t}(\mathbf{x}, t; \mathbf{n})da$. The conservation of linear momentum postulates that

$$\frac{d}{dt}\mathcal{I} := \frac{d}{dt} \int_{\mathcal{P}_S} \rho\mathbf{v}(\mathbf{x}, t)dv = \int_{\mathcal{P}_S} \rho\boldsymbol{\gamma}(\mathbf{x}, t)dv + \int_{\partial\mathcal{P}_S} \mathbf{t}(\mathbf{x}, t; \mathbf{n})da \quad (2.42)$$

By using the mass balance equation, the Cauchy stress theorem and Gaussian integral

theorem on the surface term, the Eulerian form of the linear momentum balance is obtained as

$$\rho \dot{\mathbf{v}} = \rho \boldsymbol{\gamma} + \operatorname{div} \boldsymbol{\sigma} \quad (2.43)$$

and the Lagrangian form of this equation yields

$$\rho_0 \dot{\mathbf{V}} = \rho_0 \boldsymbol{\gamma}_0 + \operatorname{Div} \mathbf{P} \quad (2.44)$$

with the material body force given per unit mass, $\boldsymbol{\gamma}_0(\mathbf{X}, t) := \boldsymbol{\gamma}(\mathbf{x}, t) \circ \boldsymbol{\varphi}_t(\mathbf{X})$.

Balance of angular momentum

Balance of angular momentum is another fundamental principle of continuum mechanics. The resultant moment of the forces acting on \mathcal{P}_S with respect to the origin described by the position vector \mathbf{x} is given as

$$\mathbf{M}_0 = \int_{\partial \mathcal{P}_S} \mathbf{x} \times \rho \boldsymbol{\gamma} dv + \int_{\partial \mathcal{P}_S} \mathbf{x} \times \mathbf{t} da. \quad (2.45)$$

The conservation of angular momentum states that the change in time of the angular momentum of the body part equals the couple \mathbf{M}_0

$$\frac{d}{dt} \int_{\mathcal{P}_S} \mathbf{x} \times \rho \mathbf{v} dv = \mathbf{M}_0 = \int_{\mathcal{P}_S} \mathbf{x} \times \rho \boldsymbol{\gamma} dv + \int_{\partial \mathcal{P}_S} \mathbf{x} \times \mathbf{t} da \quad (2.46)$$

and by inserting the mass balance equation with Cauchy stress and Gaussian integral theorems lead to

$$\int_{\mathcal{P}_S} \mathbf{x} \times (\rho \dot{\mathbf{v}} - \rho \boldsymbol{\gamma} - \operatorname{div} \boldsymbol{\sigma}) dv = \mathbf{0} \quad (2.47)$$

The above equation shows that the Cauchy stress tensor is symmetric. Thus, the balance of angular momentum provides that

$$\boldsymbol{\sigma} = \boldsymbol{\sigma}^T \quad (2.48)$$

Note that the other stress measures of $\boldsymbol{\tau}$ and \boldsymbol{S} satisfy the symmetry relation except the first Piola-Kirchoff stress \boldsymbol{P} which is a non-symmetric tensor, i.e.,

$$\boldsymbol{\tau} = \boldsymbol{\tau}^T, \quad \boldsymbol{P}\boldsymbol{F}^T = \boldsymbol{F}\boldsymbol{P}^T, \quad \boldsymbol{S} = \boldsymbol{S}^T \quad (2.49)$$

First law of thermodynamics

First law of thermodynamics is often referred as balance of energy that describes the evolution of the internal energy in a system. Total energy in a system is defined as the sum of the kinetic energy \mathcal{K} and the internal energy, E as given below

$$\mathcal{K} := \int_{\mathcal{P}_S} \frac{1}{2} \rho \boldsymbol{v} \cdot \boldsymbol{v}^b \, dv \quad \text{and} \quad E := \int_{\mathcal{P}_S} \rho e \, dv \quad (2.50)$$

with the internal energy per unit mass $e(\boldsymbol{x}, t)$ and the spatial velocity covector $\boldsymbol{v}^b = \boldsymbol{g}\boldsymbol{v}$.

The mechanical, \mathcal{P} and thermal power, \mathcal{Q} is given by

$$\mathcal{P} := \int_{\mathcal{P}_S} \rho \boldsymbol{\gamma} \cdot \boldsymbol{v}^b \, dv + \int_{\partial \mathcal{P}_S} \boldsymbol{t} \cdot \boldsymbol{v}^b \, da \quad (2.51)$$

$$\mathcal{Q} := \int_{\mathcal{P}_S} \rho r \, dv - \int_{\partial \mathcal{P}_S} \boldsymbol{q} \cdot \boldsymbol{n} \, da \quad (2.52)$$

where $r(\boldsymbol{x}, t)$ is the mass specific heat source and $\boldsymbol{q}(\boldsymbol{x}, t)$ the surface heat flux vector together with the unit normal outward, \boldsymbol{n}

The global form of the first law of thermodynamics states that time rate of change of total energy must be balanced with the mechanical power and thermal heating of the body

$$\frac{d}{dt}(\mathcal{K} + E) = \mathcal{P} + \mathcal{Q} \quad (2.53)$$

By inserting the previous relations and with the use of balance of mass and linear momentum in conjunction with the Cauchy stress and Gaussian integral theorem, the spatial form is achieved as

$$\rho \dot{e} = \boldsymbol{\sigma} : (\mathbf{gl}) + \rho r - \operatorname{div} \mathbf{q} \quad (2.54)$$

whereas the Lagrangian form of the balance of energy is given as

$$\dot{e}_0 = \mathbf{P} : \dot{\mathbf{F}} + R_0 - \operatorname{Div}[\mathbf{Q}] \quad (2.55)$$

with $R_0(\mathbf{X}, t) = r(\mathbf{x}, t) \circ \varphi_t(\mathbf{X})$

Second law of thermodynamics

The second law of thermodynamics serves as major regulation on constitutive relations of elastic and dissipative mechanisms on a thermodynamical system in which the exchange of energy with its exterior is existed via heat, work done by the body and contact forces acting on that body. Entropy which is a measure of disorder. The total entropy in a system is defined with specific entropy, $\eta(\mathbf{x}, t)$

$$\mathcal{H} := \int_{\mathcal{P}_S} \rho \eta \, dv \quad (2.56)$$

External sources can cause an irreversible change of entropy. On the other hand, the dissipative processes such as fracture evolution, plastic deformation etc result in irreversible change of the entropy. The fundamental statement of the second law of thermodynamics is that the disorder in a system tends to increase such that net entropy production is always non-negative as given in 2.57 with the integration of the mass specific entropy production, $\gamma(\mathbf{x}, t)$

$$\Gamma := \int_{\mathcal{P}_S} \rho \gamma \, dv \geq 0. \quad (2.57)$$

The quantity of heat received per unit temperature is given by

$$\mathcal{S} := \int_{\mathcal{P}_S} \frac{\rho r}{\theta} dv - \int_{\partial \mathcal{P}_S} \frac{\mathbf{q} \cdot \mathbf{n}}{\theta} da \quad (2.58)$$

So, the entropy imbalance is defined as

$$\Gamma := \frac{d}{dt} \mathcal{H} - \mathcal{S} \geq 0 \quad (2.59)$$

which can be rewritten as

$$\int_{\mathcal{P}_S} \rho \gamma dv := \frac{d}{dt} \int_{\mathcal{P}_S} \rho \eta dv - \int_{\mathcal{P}_S} \frac{\rho r}{\theta} dv + \int_{\partial \mathcal{P}_S} \frac{\mathbf{q} \cdot \mathbf{n}}{\theta} da \geq 0 \quad (2.60)$$

Spatial local form of the entropy imbalance is achieved as

$$\rho \gamma = \rho \dot{\eta} - \rho \frac{r}{\theta} + \operatorname{div} \left(\frac{\mathbf{q}}{\theta} \right) = \rho \dot{\eta} - \rho \frac{r}{\theta} + \frac{1}{\theta} \operatorname{div} \mathbf{q} - \frac{1}{\theta^2} \mathbf{q} \cdot \nabla_x \theta \geq 0 \quad (2.61)$$

This inequality can also be written in the form of Clausius-Duhem inequality

$$\rho \dot{\eta} \geq \rho \frac{r}{\theta} - \frac{1}{\theta} \operatorname{div} \mathbf{q} + \frac{1}{\theta^2} \mathbf{q} \cdot \nabla_x \theta, \quad (2.62)$$

for which the material local form is obtained as

$$\rho_0 \dot{\eta} \geq \rho_0 \frac{R}{\theta} - \frac{1}{\theta} \operatorname{Div} \mathbf{Q} + \frac{1}{\theta^2} \mathbf{Q} \cdot \nabla_X \theta \quad (2.63)$$

The entropy production in 2.61 with absolute temperature θ results in spatial dissipation

$$\mathcal{D} := \rho \gamma \theta \geq 0 \quad (2.64)$$

with the local (Clausius-Planck inequality) and conductive parts, i.e.,

$$\mathcal{D}_{\text{loc}} := \rho \dot{\eta} \theta - (\rho r - \operatorname{div} \mathbf{q}) \geq 0 \quad (2.65)$$

$$\mathcal{D}_{\text{con}} := -\frac{1}{\theta} \mathbf{q} \cdot \nabla_{\mathbf{x}} \theta = -\frac{1}{\theta} \mathbf{Q} \cdot \nabla_{\mathbf{X}} \theta \geq 0 \quad (2.66)$$

CHAPTER 3

DENSITY FUNCTIONAL THEORY

In this chapter, the results of a comprehensive study covering thermo-elastic material properties of various semiconductors from III-V and II-VI groups are provided by using ab-initio DFT simulations. Due to computationally demanding nature of DFT simulations, different simulation parameters such as supercell size, strain dependency of elastic properties are discussed on III-V and II-VI semiconductors. GaSb and InSb are commonly used III-V compounds in opto-electronic devices. Temperature dependent elastic and thermal properties of these materials are obtained from 1K to 1000K via DFT. Moreover, binary compounds of CdTe, HgTe, ZnTe from II-VI groups are also investigated to obtain thermo-elastic properties from 1K to 600K. To use computational power more efficiently, the highest temperature of II-VI semiconductor compound simulations is limited to 600K. In addition, processes such as surface cleaning, sputtering, depositing, even epitaxial growth with MOCVD on CdZnTe material can be performed below this temperature limit [143, 144]. Thermo-elastic and opto-electronic properties of CdZnTe ternary compound which is widely used for IR sensor, solar cell and X-ray detector applications are also investigated by DFT simulations. The obtained results for all of the studied materials are compared with available experimental data for different temperatures and good coherence is observed for all of the thermo-elastic material parameters.

3.1 Theory, Method and Computational Details

Computational details for DFT calculations of III-V compounds and II-VI compounds are given in this section. The investigated materials from III-V group are GaSb

and InSb whereas from II-VI group compounds, DFT calculations are performed on CdTe, HgTe, ZnTe binaries and CdZnTe ternary compound. Supercell size effect on temperature dependent elastic constants is determined on GaSb. In all III-V group calculations, combined strain levels of 0.02, 0.01, 0.005, 0.001 are applied to obtain temperature dependent elastic constants. In the calculations of II-VI group, a single supercell size is used. However, strain dependency of second order elastic constants is investigated for binaries of this group materials. Due to limited computational power and time, strain dependence of second order elastic constants of CdZnTe is not investigated.

3.1.1 III-V compounds

In this section, the computational details for DFT calculations of GaSb and InSb are provided. Temperature-dependent elastic constants (TDECs) of materials are often calculated using either the quasi-static approximation (QSA) or the quasi-harmonic approximation (QHA) [145, 146, 12, 147, 148]. In the QSA, the effect of temperature is assumed to be limited to the expansion of the lattice. For a given temperature θ , the elastic constants are calculated as the second derivatives of the total DFT ground state energy with respect to strain at a lattice constant that minimizes the Helmholtz free energy. Herein, the vibrational entropy is ignored. In the QHA, the Helmholtz free energy is written as the sum of the DFT ground state energy and the vibrational free energy. The TDECs are then calculated as second derivatives of the full free energy at the appropriate lattice constant. Since it involves the calculation of a sufficient number of phonon modes at each lattice constant and strain value, QHA is significantly costlier than QSA. However, its superior accuracy, especially at higher temperatures, compensates the computational cost. The elements of the fourth order elastic tensor C_{ijkl} are defined as

$$C_{ijkl} = \left(\frac{\partial \sigma_{ij}}{\partial \epsilon_{kl}} \right)_{\epsilon=0} \quad (3.1)$$

where σ_{ij} and ϵ_{kl} are the elements of the stress and strain tensors, respectively. Since the stress and strain are conjugate pairs, the elastic tensor can also be written through the internal energy U , using the relation

$$C_{ijkl} = \frac{1}{\Omega} \left(\frac{\partial^2 U}{\partial \epsilon_{ij} \partial \epsilon_{kl}} \right)_{\epsilon=0}, \quad (3.2)$$

where Ω represents the volume of the reference system. At a finite temperature, in the absence of external pressure, the internal energy can be replaced by the Helmholtz free energy

$$C_{ijkl} = \frac{1}{\Omega} \left(\frac{\partial^2 \psi}{\partial \epsilon_{ij} \partial \epsilon_{kl}} \right)_{\epsilon=0}, \quad (3.3)$$

where ψ is defined as

$$\psi = U + F_{\text{vib}}. \quad (3.4)$$

Here F_{vib} is the vibrational contribution to the free energy dependent on the strain ϵ and the absolute temperature θ . In terms of the phonon frequencies of the crystal, the vibrational free energy is given as

$$F_{\text{vib}}(\epsilon, \theta) = \frac{1}{2N} \sum_{\mathbf{q}\eta} \hbar \omega_{\eta}(\mathbf{q}, \epsilon) + \frac{k_{\text{B}}\theta}{N} \sum_{\mathbf{q}\eta} \ln \left[1 - \exp \left(-\frac{\hbar \omega_{\eta}(\mathbf{q}, \epsilon)}{k_{\text{B}}\theta} \right) \right]. \quad (3.5)$$

Here N represents the irreducible unit cells in the crystal, \mathbf{q} is the phonon wavevector and η is the polarization of the phonon mode. The sum runs over the wavevectors in the first Brillouin zone and are limited to a discrete grid in our computational treatment. The internal energy is replaced by the total ground state DFT energy for each strain mode. Electronic contribution to the free energy [149], which is usually treated within Mermin's theorem [150] is omitted. This contribution for the materials of interest and the temperature ranges studied here has been identified to be within a few per cent [16, 151, 12]. In addition, the QHA approximation has been identified to be accurate enough for temperatures below 1000 K instead of the full anharmonic treatment [152].

To understand the effect of different exchange-correlation functionals, all calculations are performed using both the local density approximation (LDA) [153] and the PBEsol [154] exchange-correlation functional frameworks using the Vienna Ab initio Simulation Package (VASP) [155]. Structural optimization of the materials are conducted using the conjugate gradient algorithm until all forces are under a threshold of 0.001 eV/Å. Self-consistent field calculations are conducted using the RMM-DIIS algorithm with a total energy threshold of 10^{-7} eV between consecutive steps. A threshold of 10^{-8} eV is also used in a set of test calculations to ensure total convergence. The difference between these limits is not more than %0.21 for bulk modulus, shear modulus and Poisson's ratio. A planewave cutoff of 500 eV is used to truncate the basis expansion while a Monkhorst-Pack [156] grid of $11 \times 11 \times 11$ k-points are

used to conduct Brillouin zone integrations. Gaussian smearing is used with a smearing width of 0.05 eV. Following the structural relaxation, phonon calculations are performed using finite differences to obtain F_{vib} as seen in Equation 3.5. The accuracy of the phonon dispersion is monitored by making sure that all phonon modes are real. The zero-temperature phonon dispersion is reported for both materials in Figure 3.2. As expected, the dispersion relations are very similar except for the acoustic-optic branch gap, which is smaller in InSb due to the similarity in the masses of In and Sb. At each temperature, the Helmholtz free energy is calculated at seven evenly spaced values between (and including) $0.88a_0$ - $1.12a_0$ for GaSb and $0.98a_0$ - $1.04a_0$ for InSb, where a_0 is the zero temperature equilibrium lattice constant. The Helmholtz free energy is then fit with a Murnaghan equation of state (EOS) [157] to determine the equilibrium lattice constant, $a(\theta)$, at the temperature in question. After determining total energies at seven different lattice volumes, the calculated total energies are fitted with the Murnaghan EOS,

$$E_T(V) = E_T(V_0) + \frac{B_0 V}{B'_0} \left(\frac{(V_0/V)^{B'_0}}{B'_0 - 1} + 1 \right) - \frac{V_0 B_0}{B'_0 - 1} \quad (3.6)$$

where V is the volume, B_0 and B'_0 are the bulk modulus and the pressure derivative of the bulk modulus at equilibrium volume V_0 . A representative Murnaghan EOS fit [157] is provided with PBEsol approximation for GaSb in Figure 3.1. Only temperatures of 1K, 300K and 500K are provided to simply observe lowest energy volume points. These datapoints are nothing but providing lattice constants of GaSb material at the lowest energy points for corresponding temperature. Then, the temperature-dependent linear coefficient of thermal expansion is calculated by using

$$\alpha = \frac{1}{a(\theta)} \frac{da(\theta)}{d\theta}. \quad (3.7)$$

as a readily available by-product. Once the equilibrium lattice constant is obtained for a given temperature θ , the stress values are calculated regarding to applied strains to obtain the elastic constants [158, 159]. Heat capacity determinations are equal for constant pressure and constant volume within the harmonic approximation. In Debye approximation, the specific heat capacity is given as follows [160]

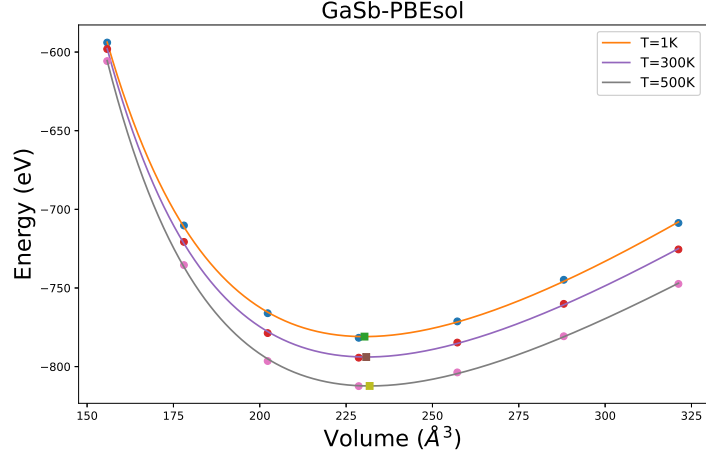


Figure 3.1: Murnaghan EOS fit of volume dependent total Helmholtz free energy for GaSb with PBEsol approximation

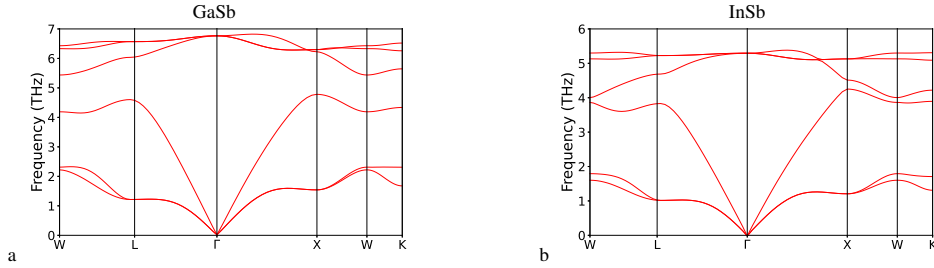


Figure 3.2: Phonon dispersion plots for GaSb and InSb, respectively.

$$C_V(\theta) = 9qk_B \left(\frac{\theta}{\theta_D} \right)^3 \int_0^{x_D} x^4 \frac{\exp x}{(\exp x - 1)^2} dx \quad \text{and} \quad x_D = \frac{\theta_D}{\theta} \quad (3.8)$$

In order to ensure convergence with respect to the number of phonon modes included, elastic constants of GaSb are calculated in supercell sizes of $2 \times 2 \times 2$ and $3 \times 3 \times 3$. For InSb, a $2 \times 2 \times 2$ supercell is considered. The numerical derivatives are calculated using a much finer grid of $27 \times 27 \times 27$ k-points and at four different values of ϵ , namely 0.02, 0.01, 0.005, 0.001. This amounts to a total of 13 total energy calculations at each temperature, 1 for the unstrained system at the equilibrium lattice constant determined at that temperature and 3 strained systems for each of the 4 strain levels. Using this method, elastic properties of GaSb, InSb are obtained in the temperature range of 1-1000K.

In addition to the elastic constants and the thermal expansion coefficients, several other related material properties such as heat capacity, Vicker's hardness, Poisson ratio are important.

The Vicker's hardness using the semiempirical expression developed by Chen [161] which is given as follows.

$$H_v = 2(\kappa^2 \mu)^{0.585} - 3, \quad (3.9)$$

Bulk modulus, B , is the response to a uniform compression so applying the strain field of $e = \epsilon_{xx} = \epsilon_{yy} = \epsilon_{zz}$ allows the computation of B with the relation

$$U = \frac{Be^2}{2} \quad (3.10)$$

where U represents the energy change due to applied strain field. Similarly, the shear modulus can be determined using the strain field of $e = \epsilon_{zz} = -2\epsilon_{xx} = -2\epsilon_{yy}$ with the equation of

$$U = \frac{3Ge^2}{2} \quad (3.11)$$

where G is the shear modulus. For cubic symmetry, the Voigt and Reuss approximations for the shear modulus are defined as

$$G_{Voigt} = \frac{1}{5}(C_{11} - C_{12} + 3C_{44}) \quad (3.12)$$

$$G_{Reuss} = \frac{5}{4(S_{11} - S_{12}) + 3S_{44}},$$

where S is the compliance matrix which is nothing but the inverse matrix to C . Finally, Hill shear modulus is defined as the arithmetic mean

$$G_{Hill} = \frac{1}{2}(G_{Voigt} + G_{Reuss}) \quad (3.13)$$

Once Bulk modulus, B , and shear modulus, G , are defined, elastic modulus, E , and Poisson's ratio ν can be determined by standard formulae of elasticity.

$$\nu = \frac{1}{2} \frac{B - \frac{2}{3}G}{2B + \frac{1}{3}G} \quad \text{and} \quad E = \frac{9B}{1 + \frac{3B}{G}} \quad (3.14)$$

3.1.2 II-VI compounds

Binary compounds of CdTe, HgTe, ZnTe from II-VI group are investigated with DFT studies to obtain temperature dependent thermal and elastic material properties from

1K to 600K. In addition, a representative case study is performed on CdZnTe ternary alloy that covers second order elastic constants as well as opto-electronic material properties, i.e, refractive index, energy bandgap, extinction in the same temperature interval. Due to requirement of greater computational power and time for ternary alloys, only CdZnTe material is investigated in this manner.

The given procedure in 3.1.1 is also followed for binary compounds of II-VI group with slight differences. QHA is still used for II-VI group materials with both of the pseudopotentials, i.e, LDA and PBEsol. Force convergence calculations are performed with conjugate gradient algorithm with a threshold of 0.001 eV/Å in structural optimizations. Self-consistent field calculations are performed with a total energy threshold of 10^{-7} eV between consecutive steps. Planewave cutoff energy of 500 eV is still valid with a Monkhorst-Pack grid of $27 \times 27 \times 27$ k-points for conducting Brillouin zone integrations. Gaussian smearing width is kept constant for all II-VI group calculations with a value of 0.05 eV. The effect of supercell size is determined on GaSb and InSb materials so only supercell size of $2 \times 2 \times 2$ is used on II-VI group binaries to use computational power efficiently. Strain dependency of elastic constants is investigated for XTe binary compounds ($X = Hg, Cd, Zn$) by applying discrete strain levels of %2, %0.5, %0.1 in the temperature range of 5-600K. The procedure of analysis for lattice constant and thermal expansion coefficient determinations are kept the same with the analysis procedure of GaSb and InSb materials. Elastic constants of CdZnTe are calculated at one strain level, i.e, $\epsilon = 0.001$. When the elastic constants are reported for disordered cubic systems which is the case for our ternary compound, CdZnTe only, the effective SOECs are defined via an average of coefficients for a simplified, anisotropic cubic system as follows,

$$\begin{aligned}\bar{C}_{11} &= \frac{C_{11} + C_{22} + C_{33}}{3}, & \bar{S}_{11} &= \frac{S_{11} + S_{22} + S_{33}}{3} \\ \bar{C}_{12} &= \frac{C_{23} + C_{13} + C_{12}}{3}, & \bar{S}_{12} &= \frac{S_{23} + S_{13} + S_{12}}{3} \\ \bar{C}_{44} &= \frac{C_{44} + C_{55} + C_{66}}{3}, & \bar{S}_{44} &= \frac{S_{44} + S_{55} + S_{66}}{3}\end{aligned}\quad (3.15)$$

where the effective elastic constants and compliances are represented with \bar{C}_{ij} and \bar{S}_{kl} . In this case, shear modulus in Voigt and Reuss approximations in (3.12) is still valid with the effective coefficients.

In order to calculate the temperature-dependent energy band gap of the CdZnTe, the equilibrium lattice constants are extracted from the QHA calculations, then the electron-phonon interaction is introduced in the method proposed by Zacharias and Giustino [162] by displacing atoms from their ground state position according to the vibrational spectrum by 0.015 Angstrom for temperatures of 5 K, 20 K, 40 K, 80 K, 100 K, 150 K, 200 K, 250 K, and 300 K. The displacement is performed within a total of 2 steps by the PBEsol approximation and a 277 eV cut-off for plane-waves and $0.154 \times 0.152 \times 0.037$ 1/Angstrom³ k-point spacing with an electronic convergence of 10^{-7} eV. The band gaps are calculated from the resulting structure of the one-shot displacement pattern by employing modified Becke and Johnson LDA (MBJLDA) [163] functional to have a more accurate value compared to standard LDA or GGA approximations. The temperature-dependent optical properties are only calculated within the PBEsol approximation due to the high computational cost with 3000 grid points and 0.1 shift parameter to have more accurate dielectric functions.

3.2 Numerical Results

3.2.1 III-V compounds

Temperature-dependent lattice constants, thermal expansion coefficients, and elastic constants of bulk GaSb and InSb are computed for a wide range of temperatures with the quasi-harmonic approximation (QHA) based DFT calculations.

Figure 3.3 displays the temperature-dependent lattice constant and coefficient of thermal expansion of GaSb and InSb. The numerical values are compared with the available experimental data of Nilsen *et al.* [43] and Dutta *et al.* [164]. Both LDA and PBEsol show good agreement with the experimental lattice constant data. As often documented in the literature [165, 166], PBEsol slightly overestimates the lattice constant. The calculated linear expansion coefficient also displays excellent agreement with experimental data for GaSb and InSb in the range of experimental data. The coefficient of thermal expansion of InSb from 2K to 40K is determined experimentally

by Sparks in 1967 [167] which shows good agreement with both LDA and PBEsol calculations. Breivik *et al.* [51] determined lattice constant and coefficient of thermal expansion of InSb between 32°C and 325°C and provided first and second order polynomial fits, respectively which provides also excellent coherence with our results but shows clear difference in magnitudes. The discrepancies in lattice constant calculations of InSb have been previously reported. For III-V compounds such as InAs, InSb, Lindsay *et al.* [168] report an error of 1.0%-1.5% DFT calculations and experimental values of the lattice constant. Mohammed *et al.* [169] performed DFT calculations on InSb and InAs and determined the lattice constant of these compounds with an error of 2.5% with respect to the experimental results given by Landolt *et al.*[170]. Finally, the InSb linear expansion coefficient was underestimated by at least a factor of two in the work by Miranda *et al.* [171]. The three TDECs relevant to the cubic lattice, namely C_{11} , C_{12} , and C_{44} are displayed for the two materials in Figure 3.4. The dependence on the supercell size for GaSb resulted in a slight difference between $2 \times 2 \times 2$ and $3 \times 3 \times 3$. This difference is observed to increase as temperature increases, but remains below 2% throughout the full temperature range. Both the LDA and the PBEsol functionals slightly underestimate the experimental values. However, the errors remain small. The maximum errors occur for all of the cases at 0K and are displayed in Table 3.1. Overall, LDA provides a better representation of the second-order elastic coefficients, which can be expected due to the softening of the bonds in the PBEsol approximation.

The variation of the elastic constants and thermal expansion coefficient with temperature is important to predict developed stresses on materials accurately. For GaSb, LDA results showed that C_{11} , C_{12} drop 5.37% and 10.94% in the given temperature regime, respectively. C_{44} shows a relatively stable results in the given temperature interval with 2.78% decrease. In contrast, LDA provides C_{11} and C_{12} in the same temperature interval such that drop of 10.04% and 18.90% observed for InSb material. For InSb, C_{44} again shows a small drop with 2.68%. It can be concluded that thermo-mechanical stress predictions by using temperature dependent material properties can provide higher accuracy difference for InSb material in comparison to GaSb due to effect of temperature on second order elastic constants is more obvious for InSb material. PBEsol provides very similar differences in temperature regarding

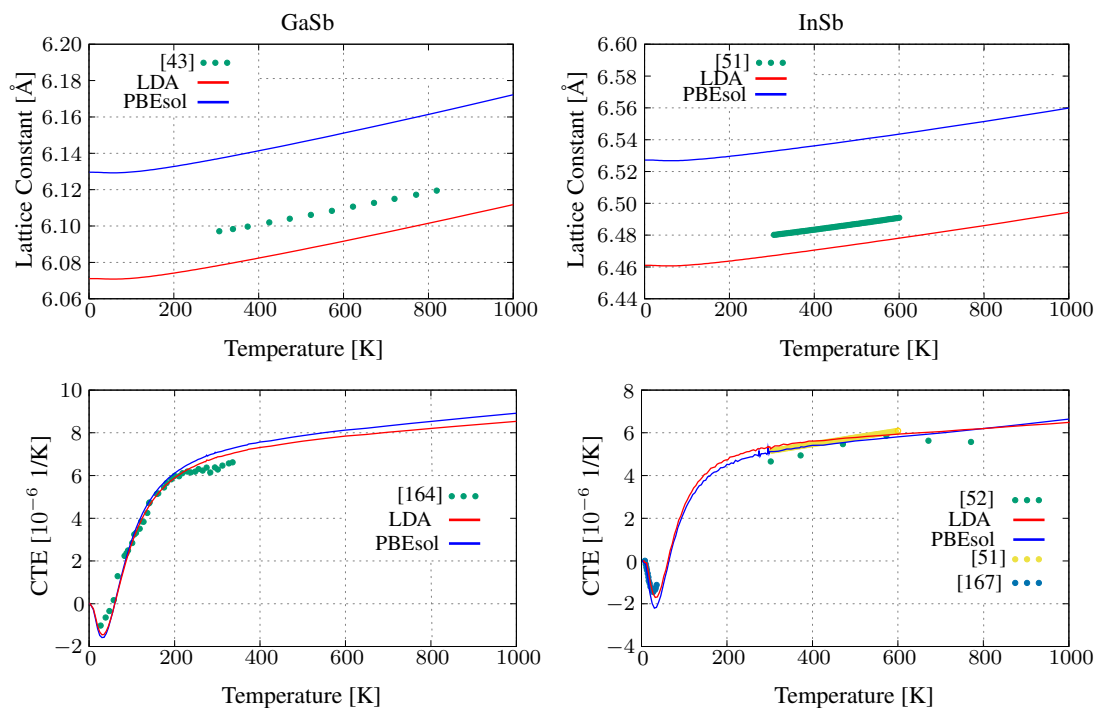


Figure 3.3: (a, b) Calculated temperature-dependent lattice constant of GaSb (left) and InSb (right) with PBEsol (blue), LDA (red). Dotted lines represent the experimental data from Nilsen *et al.* [43] and Breivik *et al.* [51] for GaSb and InSb, respectively, performed by X-ray diffraction measurements. (c, d) Coefficient of thermal expansion (CTE) of GaSb and InSb is provided by using LDA (red) and PBEsol (blue) pseudopotentials. Experimental result of thermal expansion coefficient (green) for GaSb and InSb are provided by Dutta *et al.* [164] and Cai and Wei [52] (green), Breivik *et al.* [51] (orange), Spark and Swenson [167] (purple), respectively.

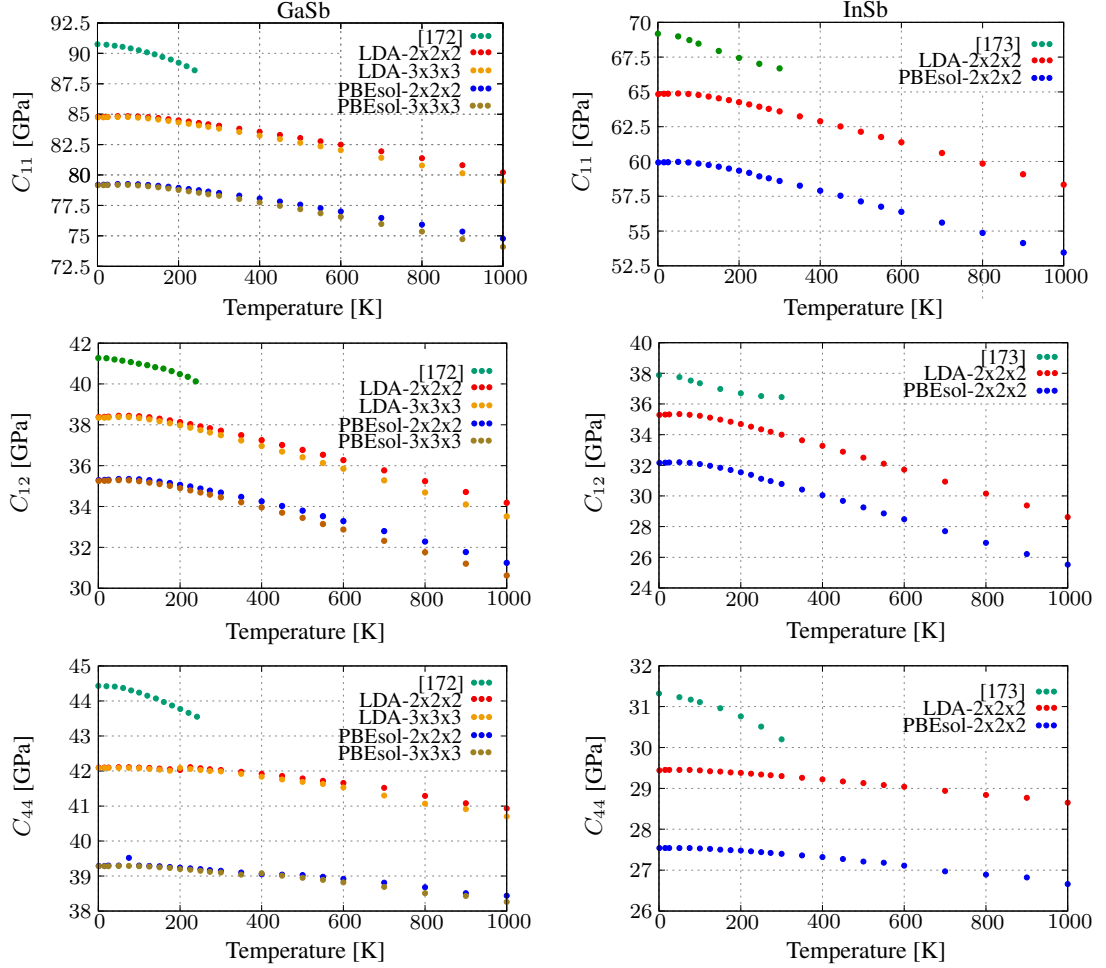


Figure 3.4: (a, b, c, d, e, f) Temperature-dependent second order elastic constants, C_{11} , C_{12} , C_{44} , of GaSb (left) and InSb (right) are provided by using LDA (red) and PBEsol (blue). The supercell size of $3 \times 3 \times 3$ for LDA and PBEsol is only provided for GaSb. There is no significant difference between the two supercell sizes. So, the supercell size of $2 \times 2 \times 2$ is given only for InSb. Experimental data (purple) is taken from Boyle [172] and Slutsky [173].

Table 3.1: Maximum error between DFT results and the experiments in SOEC.

GaSb			
Pseudopotential	C_{11}	C_{12}	C_{44}
LDA	6.62%	7.00%	5.28%
PBEsol	12.73%	14.48%	11.58%
InSb			
Pseudopotential	C_{11}	C_{12}	C_{44}
LDA	6.27%	6.84%	6.00%
PBEsol	13.37%	15.10%	12.07%

to second order elastic constants.

The Poisson ratio, Vicker's hardness and the heat capacity of the two materials are shown in Figure 3.5. InSb was found to be about half as hard as GaSb at low temperatures while both materials display sharply increasing hardness with increasing temperature. At 1000K, the hardness value was found to be about 10.4% and 37.3% larger than the 1K value for GaSb and InSb, respectively. Interestingly, the PBEsol and LDA values display different rates of increase at higher temperatures. In fact, the underestimating trend of PBEsol is reversed as a result of a crossover at high temperatures. Obtaining an increase of hardness values with increasing temperature may be caused by decreasing trend of shear modulus, μ which is given in the denominator of equation 3.9. The decreasing trend of shear modulus is also given in Figure 5.8

Poisson's ratio is expected to decrease with increasing temperature. In fact, a decreasing trend is observed for both materials in Figure 3.5. The heat capacity values of GaSb and InSb are only calculated using LDA are also shown in Figure 3.5 (e) and (f), respectively. For both materials, Passler [174] defined heat capacities by means of a refined version of low-to-high temperature interpolation formula of non-Debye type. In this study, it is also provided analytical descriptions of anharmonicity related differences of isobaric and isochoric parts of heat capacities. Our results show excellent coherence from 1K to 300K. For higher temperatures, the results of Passler follows a slightly increasing trend whereas our results are constant, as expected. Pashinkin *et*

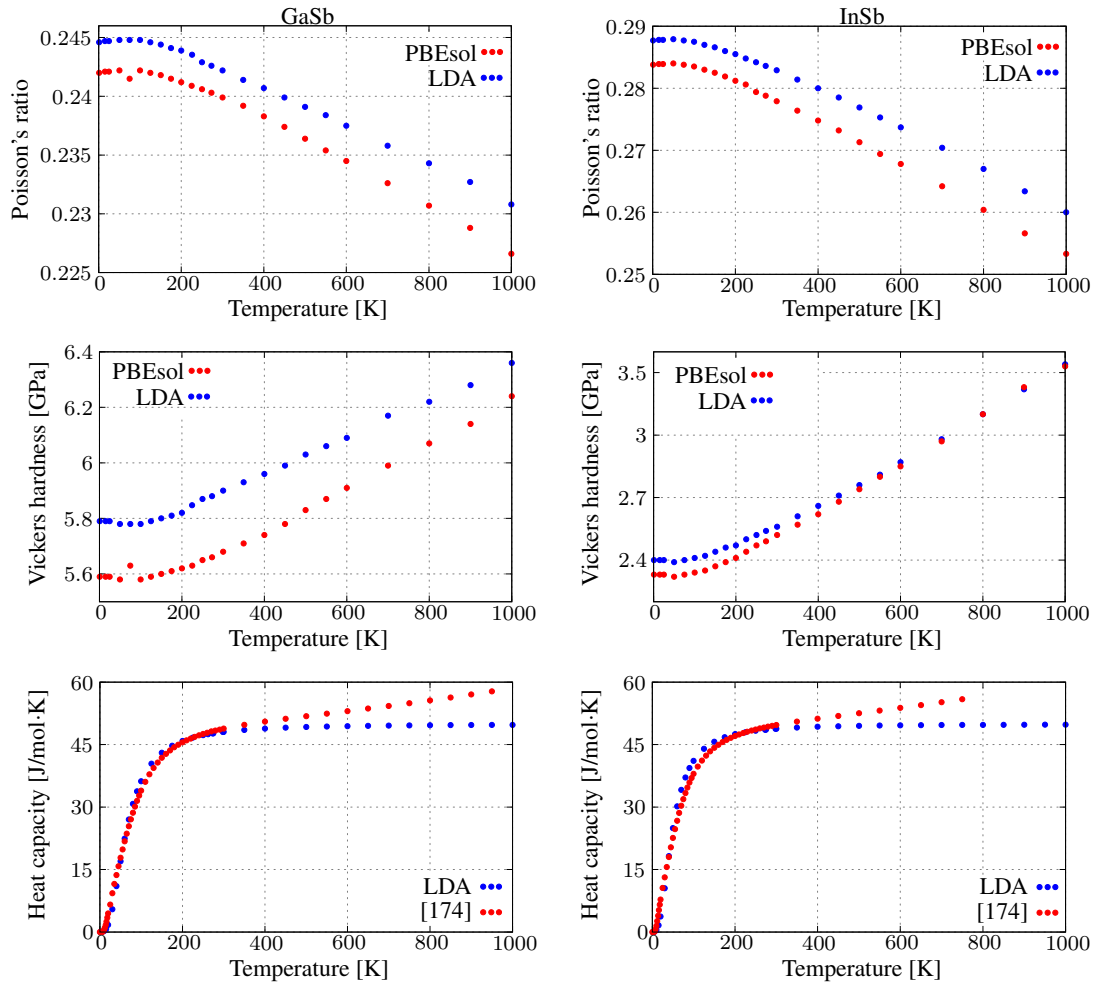


Figure 3.5: (a) Temperature-dependent Poisson's ratio of GaSb is given with LDA (blue) and PBEsol (orange). (b) Temperature-dependent Vicker's hardness of GaSb provided with LDA (blue) and PBEsol (orange). (c) Temperature-dependent Poisson's ratio of InSb. (d) Temperature-dependent Vicker's hardness of InSb. Both of these are provided with LDA (blue) and PBEsol (orange). Heat capacity results of DFT calculations for GaSb and InSb are given in (e) and (f), respectively.

al. [175] provided experimental results of heat capacities of GaSb and InSb which are measured by drop calorimetry. According to the results of this study, heat capacity of GaSb and InSb at 300K is 48.70 J/mol.K and 49.29 J/mol.K respectively. Our DFT results yield 48.04 J/mol.K for GaSb and 48.80J/mol.K for InSb. This amounts to an error of only 1%.

III-V materials are widely used in high-performance optoelectronics applications because of having advantageous properties of direct bandgap, high electron mobility and low exciton binding energy. GaSb and InSb materials are often exposed to large temperature differences during fabrication processes or operation conditions of an optoelectronic device such as IR sensors. In this section, it is presented a complete set of temperature-dependent thermo-elastic material properties for the two materials with the QHA approximation using DFT. In addition, the obtained results are compared with existing experimental and computational studies where possible. Specifically, the calculated values for second-order elastic constants C_{11} , C_{12} , C_{44} , elastic moduli, Vickers hardness, Poisson's ratio, isobaric heat capacity and the Lamé coefficients are reported. The provided results are, overall, in very good agreement with experimental values, in spite of the difficulties associated with the accurate measurement of these values in a large temperature range.

The calculations are conducted making sure that the convergence is achieved with respect to the relevant calculation parameters and two different approximations to the exchange-correlation were used (LDA and PBEsol). The given results are intended to serve as a reference for the variation of important elastic constants over a large temperature change. These variations have been carefully quantified and reported. To render the obtained results more versatile, an analytical expression for the temperature-dependent free energy function is proposed that allows accurate prediction of thermally and mechanically induced stresses for cubic symmetric GaSb and InSb in Section 5.3. In addition, functional fits are provided to the Lamé coefficients, which can now be extracted at any desired temperature.

3.2.2 II-VI compounds

In this part, an extensive numerical investigation is carried out in order to obtain the theoretical limits of the thermoelastic properties of CdTe, HgTe, ZnTe, CdZnTe. Achieved results are compared against the available experimental data and extend their range to cover all relevant temperatures. Temperature dependent opto-electronic material properties of CdZnTe ternary compound such as energy band-gap, refractive index, extinction constant are also provided via *ab initio* DFT simulations. Temperature-dependent lattice constants, thermal expansion coefficients and second order elastic constants of these semiconductors are computed for a wide range of temperatures with the quasi-harmonic approximation (QHA) based DFT calculations. Given equations for free energy, stress, Lamé parameters from equation 5.1 to 5.8 are also valid for calculations of II-VI compounds.

Figure 3.6 displays the temperature-dependent lattice constant and coefficient of thermal expansion of CdTe, HgTe and ZnTe. The numerical values are compared with the available experimental data of Bagot *et al.* [77]. Both LDA and PBEsol follow very similar trends with the experimental coefficient of thermal expansion data. However, LDA provides better agreement with the experimental results for all three binary compounds. As expected, both LDA and PBEsol lattice constants follow the same trend as a function of temperature with LDA yielding smaller values.

Since the SOECs are determined through finite-difference based derivatives, the amount of strain used may have an effect on the numerical values. To test this issue, strain sensitivity of the SOECs of CdTe, ZnTe and HgTe are explored. Strain levels of 2%, 0.5% and 0.1% are applied and the results of SOECs are compared for the LDA and the PBEsol approximation. In Figure 3.7, the LDA behaviour for C_{11} and C_{12} calculations change visibly going from 0.5% to 2% with remarkably good agreement with experiment for CdTe. However, the PBEsol approximation is almost insensitive to strain change from 0.5% to 2%. Conversely, the PBEsol approximation remains unaffected. Going from 0.1% to 0.5%, instead, values calculated within the PBEsol approximation show a significant change. This interesting result indicates that different levels of exchange-correlation approximations show different levels of sensitivity to numerical displacements. In contrast, LDA and PBEsol approximations do not

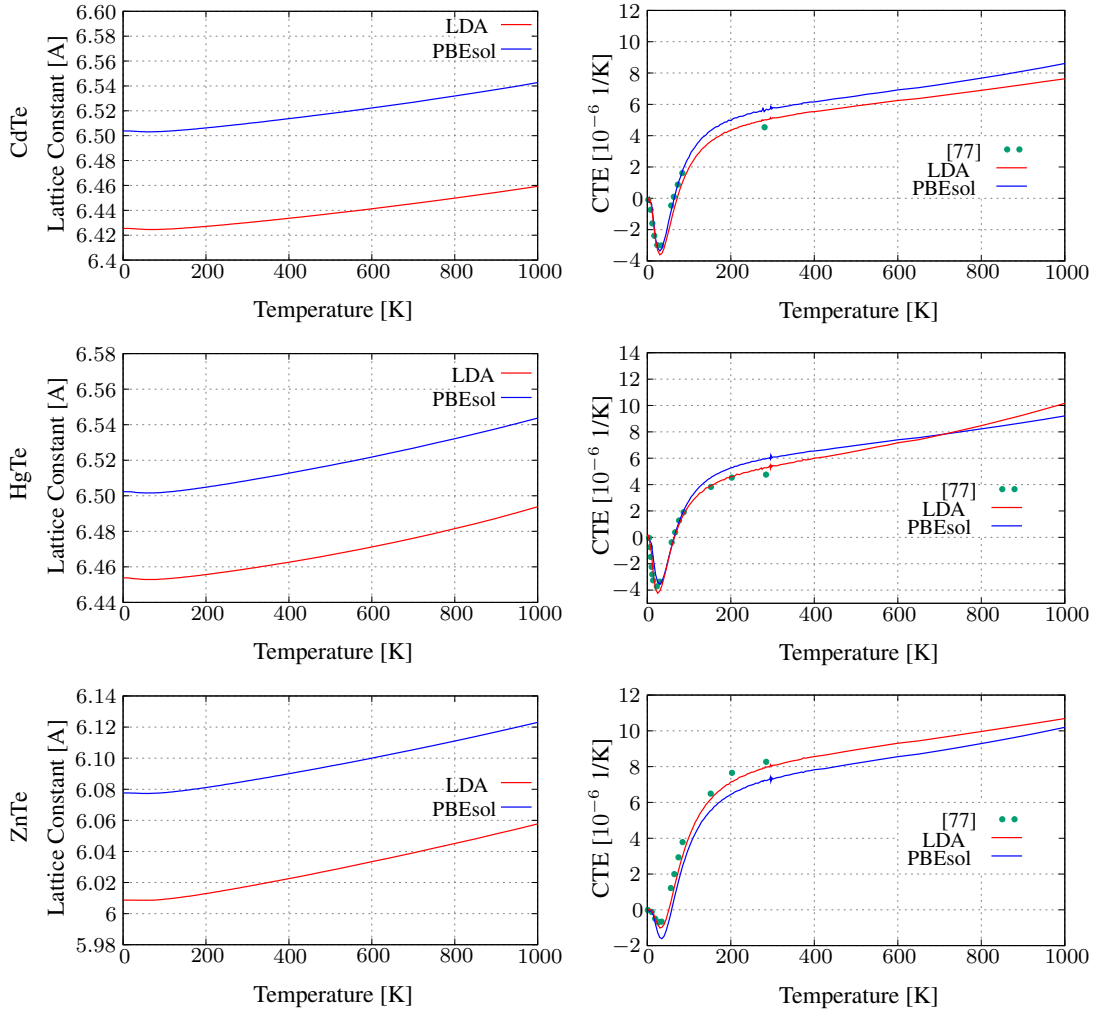


Figure 3.6: (a) Calculated temperature-dependent lattice constant of CdTe with PBEsol (blue), LDA (red). (b) Coefficient of thermal expansion (CTE) of CdTe is provided by using LDA (red) and PBEsol (blue) pseudopotentials. Experimental result of thermal expansion coefficient (green) for CdTe is taken from Bagot et al. [77]. (c) Calculated temperature-dependent lattice constant of HgTe with PBEsol (blue), LDA (red). (d) Coefficient of thermal expansion of HgTe is provided by using LDA (red) and PBEsol (blue). Experimental result of coefficient of thermal expansion of HgTe is also provided by Bagot [77] (green). (e) Lattice constant of ZnTe is given with PBEsol (blue), LDA (red). (f) Thermal expansion coefficient of ZnTe is provided with PBEsol (blue), LDA (red) and compared with available experimental result of Bagot et al. [77].

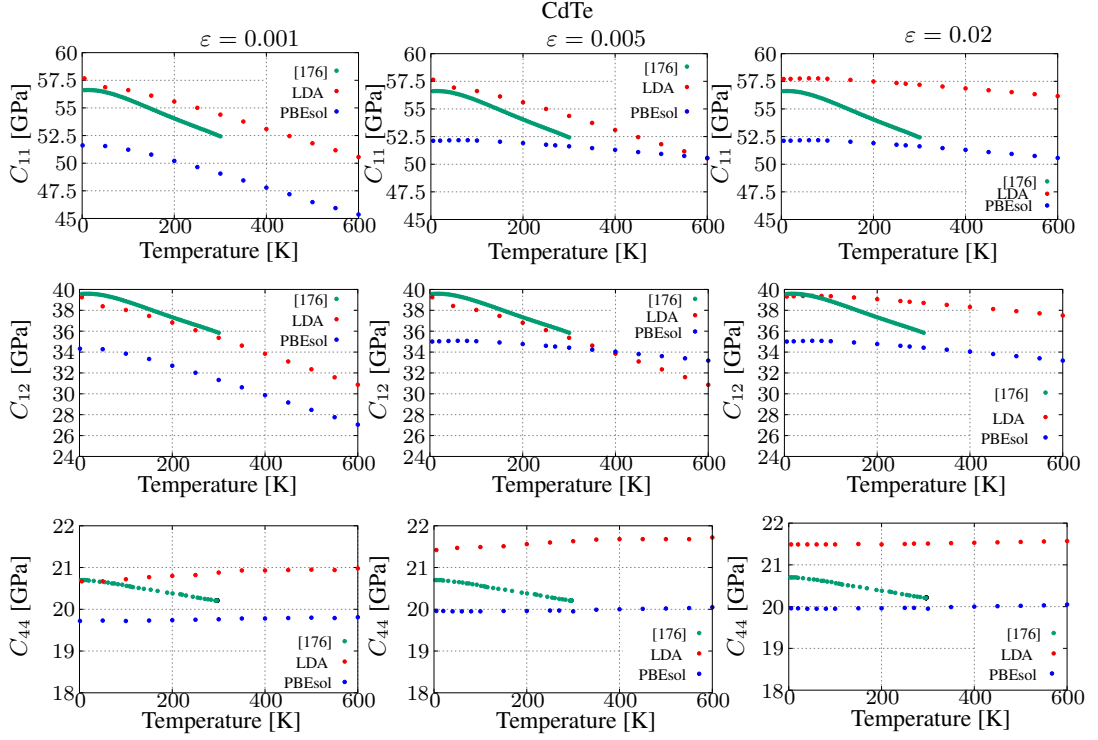


Figure 3.7: Temperature-dependent second order elastic constants of CdTe are provided by using LDA (red) and PBEsol (blue) with 0.1% strain (left column), 0.5% strain (middle column) and 2% strain (right column). Experimental data (purple) is taken from Greenough and Palmer [176].

provide a behaviour change in terms of SOECs for ZnTe and HgTe as given in Figures 3.8 and 3.9, respectively. The calculated SOECs for ZnTe and HgTe remain essentially insensitive to the various strains used in the test. For ZnTe, the experimental data is available only at four different temperatures. The numerical results shows good coherence in magnitude but the slope of second order elastic constants with increasing temperatures is different for the applied strain limits. The amount of distortion or strain is important while determining SOECs. If the applied strain value is too small, changes in the derivatives of the total energy of the cell with respect to distortions, i.e, the stress, may be too small to have good accuracy. On the other hand, if the strain is too large, anharmonicity of the energy may be a problem in terms of accurate determinations of SOECs.

SOECs calculated for a strain of 0.1% are reproduced all in one place for the three materials in Figure 3.10, for ease of comparison. The expected downward trend of all

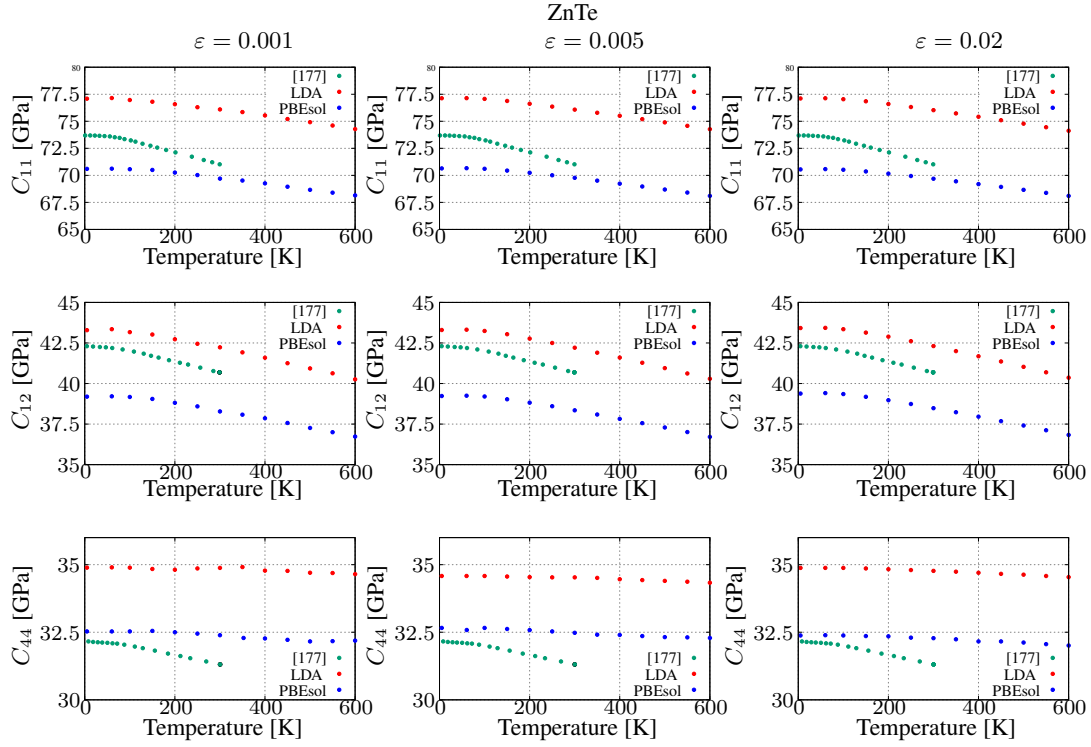


Figure 3.8: Temperature-dependent second order elastic constants of ZnTe are provided by using LDA (red) and PBEsol (blue) with 0.1% strain (left column), 0.5% strain (middle column) and 2% strain (right column). Experimental data (purple) is taken from Lee [177].

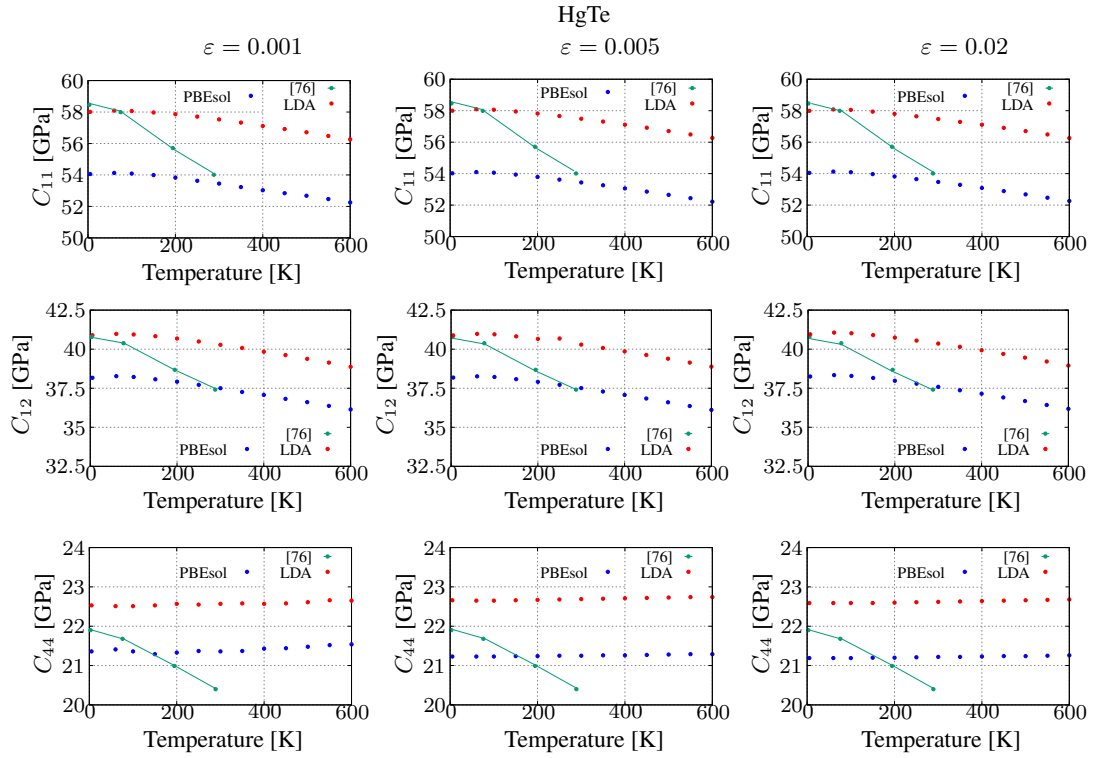


Figure 3.9: Temperature-dependent second order elastic constants of HgTe are provided by using LDA (red) and PBEsol (blue) with 0.1% strain (left column), 0.5% strain (middle column) and 2% strain (right column). Experimental data (purple) is taken from Cottam [76].

elastic coefficients with increasing temperature are observed in all experimental and DFT data presented here. Overall, all of the calculated values agree with experimental findings, with slight but notably difference. In general, LDA and PBEsol represents about a 10% bracket in which the available experimental results stay for the given temperature range. The most significant difference is the slope of the elastic constants, where the experimental elastic constants drop faster than the calculated ones. The reason for this could be attributed to one or more of the effects omitted from our quasiharmonic approach. The contribution of the electronic free energy (due to electronic entropy) is expected to be small, and therefore unlikely to cause this amount of difference. Similarly, the anharmonic effects are omitted in all similar calculations due to their minor contributions at these temperatures [178]. The conditions under which the experimental measurements were taken could be different from our simulated conditions. At higher temperatures, if the sound velocity exceeds the speed of heat transfer, the elastic constants that are measured could be isentropic as opposed to our isothermal values, which assume instant heat transfer [179]. Since the correction to isothermal elastic constants to make them isentropic is linear in temperature with a positive slope, this could potentially account for the difference.

Poisson ratio of the binary compounds of CdTe, HgTe, ZnTe are given in Figure 3.11. Both LDA and PBEsol results show an identical decreasing trend with increasing temperature with slightly different values. For HgTe, however, the difference between the two approximations is very small, both essentially following the exact same graph.

Calculated heat capacity values of the binary compounds are also given in Figure 3.11. Although CdTe, ZnTe and HgTe show very similar characteristics with increasing temperature in terms of heat capacity values, an increase up to 100K in Figure 3.11 (d, e, f) is observed with slightly different slopes. In Figure 3.11 (f), DFT results of ZnTe agree with the experimental results of Gavrichev *et al.* [180, 181]. For HgTe and CdTe, our calculated heat capacities agree with the available experimental results within an error of 5%. [182, 183, 184, 185].

Due to the increased computational cost in CdZnTe ternary compound calculations, the strain dependence of SOECs is not performed. Only PBEsol approximation is ap-

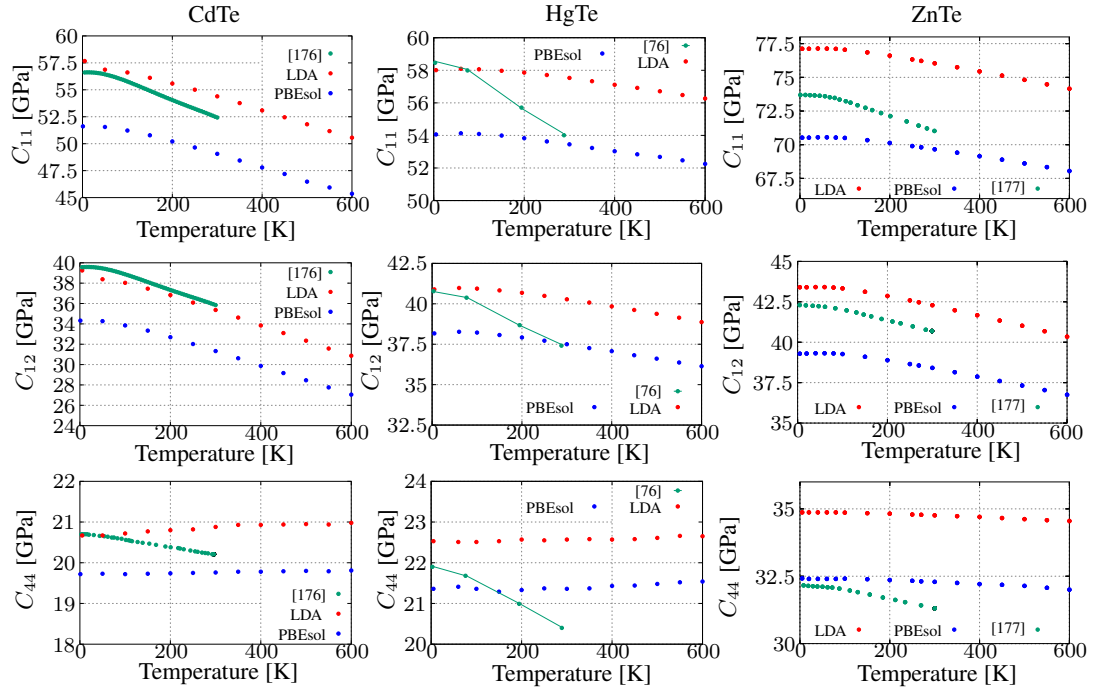


Figure 3.10: (a, d, g) Temperature-dependent second order elastic constants of CdTe are provided by using LDA (red) and PBEsol (blue) with the supercell size of $2 \times 2 \times 2$. Experimental data (purple) is taken from Greenough and Palmer [176]. (b, e, h) For HgTe, the second order elastic constants are provided by using LDA (red) and PBEsol (blue). Experimental data is taken from Cottam and Saunders [76] (green). (c, f, i) Second order elastic constants of ZnTe are provided with LDA and PBEsol. Experimental results of Lee [177] is also provided. LDA estimates approximately 10% larger values of elastic constants. A strain value of 0.001 is used to generate these results.

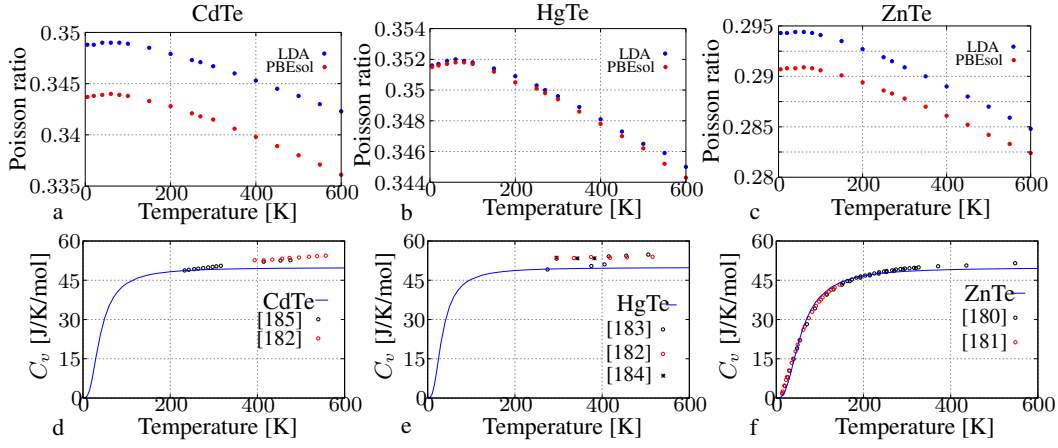


Figure 3.11: (a, b, c) Poisson ratio of CdTe, HgTe and ZnTe in the temperature range from 1K to 600K. (d, e, f) Temperature dependent heat capacity, C_v values of CdTe, HgTe and ZnTe are given in the same temperature interval.

plied on CdZnTe material. C_{11} , C_{12} and C_{44} results for CdZnTe material are given in Figure 3.12 (a, b, c). There is a slight uptrend from 5K to 80K, then a clear downtrend from 80K to 600K in C_{11} , C_{12} results. Similarly to the binary compounds, C_{44} shows very little variation as a function of temperature for CdZnTe. Temperature-dependent second order elastic constants of $Cd_{1-x}Zn_xTe$ with $x = 0.04$ was investigated by Queheillalt and Wadley [186] by a laser-based ultrasonic technique. Second-order polynomial fits of the provided experimental results are given in Figure 3.12 (a, b, c). The experimental results of C_{11} , C_{12} and C_{44} show a downtrend with increasing temperature from 273K to 600K. The behavior of CdZnTe exhibits comparable trends with changing temperature, experimental error margins and potential sources of errors to other investigated materials. The discourse presented for binary compounds is also applicable to CdZnTe.

In Figure 3.12 (d, e, f), Poisson ratio, Vicker's hardness and heat capacity results of DFT are shown and compared with the available experimental data [187, 188, 189]. In spite of the scarcity of available data and differences in the composition, good agreement with experimental work is observed.

Opto-electronic properties of the materials (absorption, quantum efficiency, etc.) greatly impact the performance of the devices which are made of these semiconductor materials. In the literature, the temperature-dependent band gap of the binary compounds

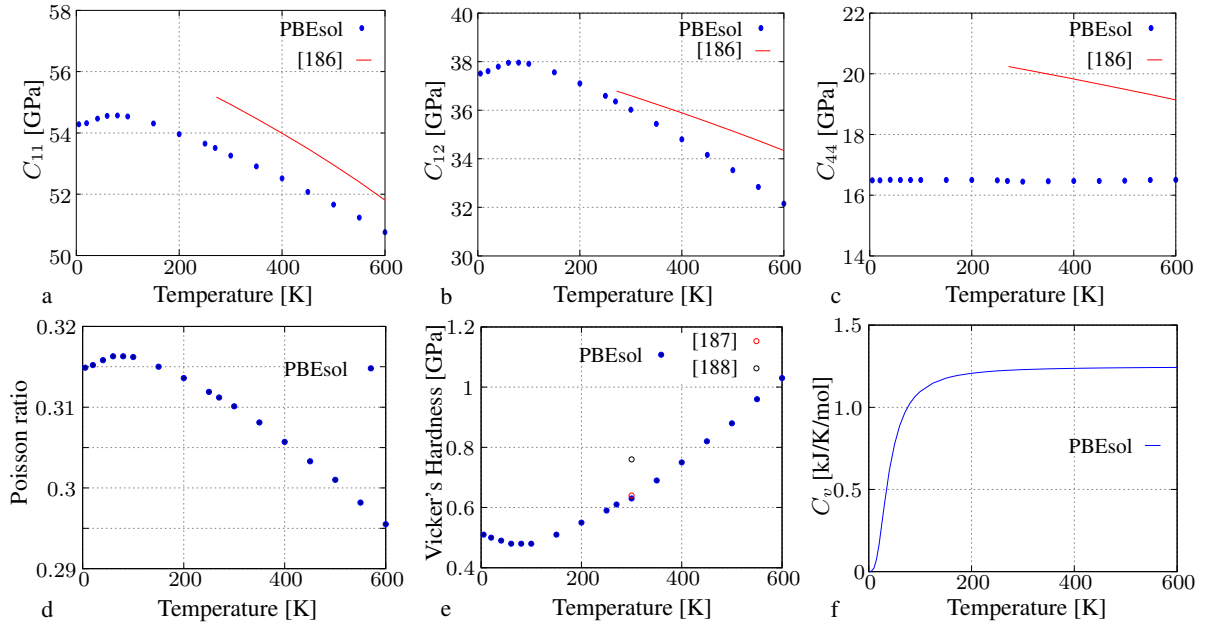


Figure 3.12: Second order elastic constants, a) C_{11} , b) C_{12} , c) C_{44} , d) Poisson ratio, e) Vicker's hardness, f) Heat capacity values of CdZnTe

of XTe (X=Cd, Hg, Zn) were calculated by Tsay et al. [190]. Furthermore, the compositional effects on the CdZnTe energy band-gap are widely investigated in the literature such as the study given by Strzalkowski et. al. [191] where the growth of the CdZnTe is performed by vertical Bridgman-Stockbarger method for different zinc compositions. The composition of the crystal is determined with a method employing SEM/EDS spectrum and the compositional dependence of energy band-gap is calculated based on transmission spectroscopy spectra as 1.515 eV for Cd_{0.96}Zn_{0.04}Te. Moger *et al.* [192] used the thermal co-evaporation method to grow CdZnTe thin films and then analyzed the structural, morphological, and optical properties of these films by several experimental techniques. The compositional dependence of the energy band gap is extracted from seven data points ranging from $x = 0$ to 1 for Cd _{x} Zn _{$1-x$} Te and is fitted with Vegard's law [193, 194] which the energy band gap of Cd_{0.96}Zn_{0.04}Te was calculated to be 1.539 eV at room temperature.

In order to evaluate the temperature-dependent behavior of these materials, the energy band gap, refractive index, and extinction coefficient of the Cd_{0.96}Zn_{0.04}Te ternary alloy are calculated with MBJLDA approximation for temperatures of 5 K, 20 K, 40

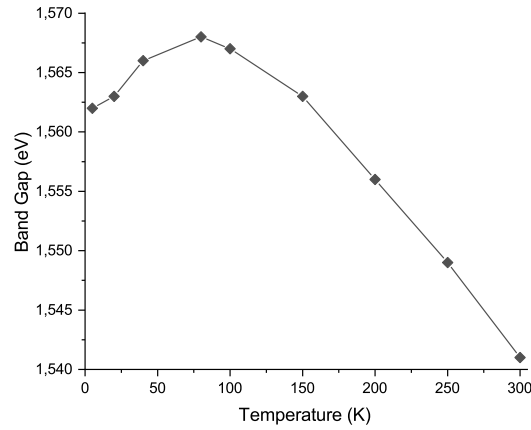


Figure 3.13: Temperature dependent energy band-gap of CdZnTe

K, 80 K, 100 K, 150 K, 200 K, 250 K, and 300 K. The results (see Figure 3.13) show that CdZnTe material has an energy band gap of 1.541 eV for 4% Zn content at room temperature which is in good agreement with the experimental results of the reference [192]. On the other hand, there is an energy difference of 26 meV compared to the result of the reference [191]. This can be attributed to the inadequacy of the conventional single-particle Kohn-Sham approach to represent excited states.

In Figure 3.13, the effect of the temperature on the energy band gap of CdZnTe is given. The rate of change of the band gap as a function of temperature, $-dE_g/dT$, is calculated as 1.2×10^{-4} eV/K. This value is lower than those of CdTe and ZnTe [190] while the behavior is similar.

The calculated optical properties i.e, the refractive index and the extinction function of the CdZnTe are given in Figure 3.14 and 3.15, respectively. The change in the critical points of E_0 and E_1 are shown in both figures' insets. The values of the E_0 and E_1 present a red shift with increasing temperature in the insets of Figure 3.14 and 3.15. The change of the E_1 critical point energies with respect to temperature in the 20 K to 300 K range is 20 meV which is similar but lower than that given in reference [190] (≈ 140 meV) for ZnTe. The room-temperature critical point energy of E_1 is determined from Figure 3.14 as 3.322 eV which is in good agreement with the spectroscopic ellipsometry data (≈ 3.31 eV) taken from the molecular beam epitaxy grown CdZnTe layer [195].

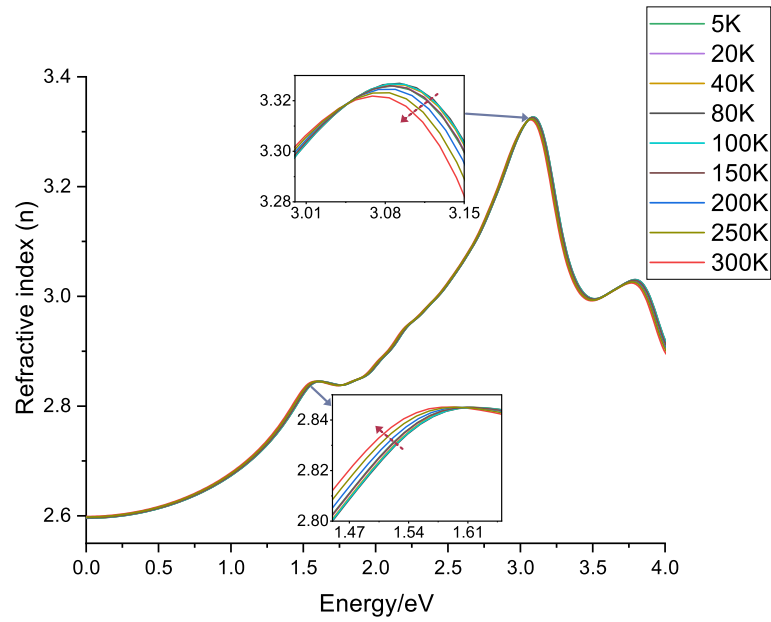


Figure 3.14: Temperature dependent refractive index of CdZnTe

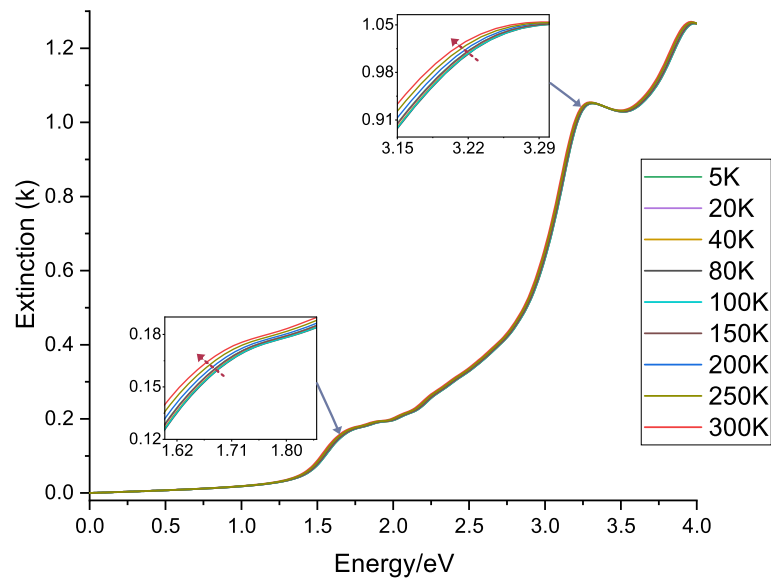


Figure 3.15: Temperature dependent extinction constant of CdZnTe

II-VI materials, which are very important for such technologies as detector production, are routinely produced nowadays with epitaxial methods. Ternary compounds can be used to have desired material properties with proper combinations of materials and growth techniques. Thermo-mechanical stresses and impurities in the crystal structure may deteriorate crystal quality which is detrimental to the opto-electronic properties. During the growth, microfabrication processes of semiconductors, and operation conditions of opto-electronic devices may expose the material to significant temperature gradients. A complete set of temperature-dependent thermo-elastic material properties for XTe binary compounds (X=Cd, Hg, Zn) and the CdZnTe ternary compound is given in this section. The lattice constant and thermal expansion coefficient of the binary compounds are compared with the available experimental data and a good overall agreement is observed with our numerical results. The energy band gap, extinction, and refractive index of the zinc-blend ternary compound are also reported for a temperature regime of 5-300K.

CHAPTER 4

EXPERIMENTAL STUDIES

In this chapter, conducted experimental studies are given. At first, nanoindentation tests are conducted on GaSb material to check elastic modulus and hardness properties. Basically, two different types of GaSb material are used in these experiments according to surface treatment of GaSb i.e, polished or non-polished. Then, a test setup is designed to perform cryocooling experiments on GaSb and CdZnTe materials to observe crack initiation and propagation paths. Integrated assemblies of the semiconductors with stainless steel cooled down to 77K and heated up to room temperature. Developed crack patterns are observed at room temperature via Scanning Electron Microscopy.

4.1 Nanoindentation

The use of nanoindentation is a valuable technique for obtaining mechanical properties of various materials, such as hardness, elasticity, and plasticity behaviors [196, 197, 198, 199]. The advancement of technology in building micro/nano-scale devices has led to a need for more precise and accurate approaches to studying material behavior. Continuum theories and traditional approaches may not be sufficient, as scaling effects can dominate the material behavior, resulting in significant errors in determining material properties at the macroscopic level. This section focuses on the application of nanoindentation tests on GaSb material to provide a baseline for the temperature-dependent thermo-elastic material properties that are obtained by Density Functional Theory (DFT) in this thesis. Nanoindentation is a standard engineering tool that is useful for characterizing the mechanical properties of materials at

the nanoscale, including bulk materials, polymers, composites, and thin films. Other techniques, such as Atomic Force Microscopy (AFM), micro-Raman Spectroscopy, Scanning Electron Microscopy (SEM), and Focused Ion Beam (FIB) techniques, can also be used to determine the deformation mechanism of various semiconductor materials like Ge, Si, GaSb, InP, and others.

A nanoindentation measurement is generally performed with a three sided Berkovich indenter which sinks onto the sample surface. By recording the load, displacement and time during the indentation, local mechanical properties of the material can be accomplished. Oliver-Pharr method [200] provided the procedure of determining elastic modulus and hardness properties via nanoindentation with Berkovich indenter. It became a commonly used method on different investigations, materials, applications. [201, 202, 203].

In our experimental investigations, CSM Instrument Nanoindenter is used in Bilkent-UNAM campus. It is equipped with diamond Berkovich indenter. Typical indentation curve is given in Figure 4.1. Applied force during the indentation is not constant as it seen in typical indentation curve. Loading and unloading sections of the process is labeled as "a" and "b" in Figure 4.1, respectively. The tangent curve at the beginning of the unloading section is defined as "c" at F_{max} . The permanent indentation depth after removal of the test force is defined as h_p . The point of the tangent "c" to curve "b" at maximum load with the indentation depth axis is defined as h_r whereas the depth of contact of the indenter with the sample at F_{max} is given as h_c . The maximum indentation depth at corresponding load F_{max} , is given as h_{max} . The contact stiffness at F_{max} and the geometric constant are represented with S and ϵ , respectively.

The extreme limits of the ideal mechanical behavior of materials can be defined as ideal elastic and rigid plastic. In ideal elastic case, the loading and unloading curves are coincident so that there does not exist permanent deformation at the end of unloading stage. In rigid plastic case, the induced deformation cannot be recovered so that unloading stage will result in a vertical downward line starting at F_{max} . However, elasto-plastic behavior is widely observed on engineering materials whose characteristic behavior is actually given in Figure 4.1.

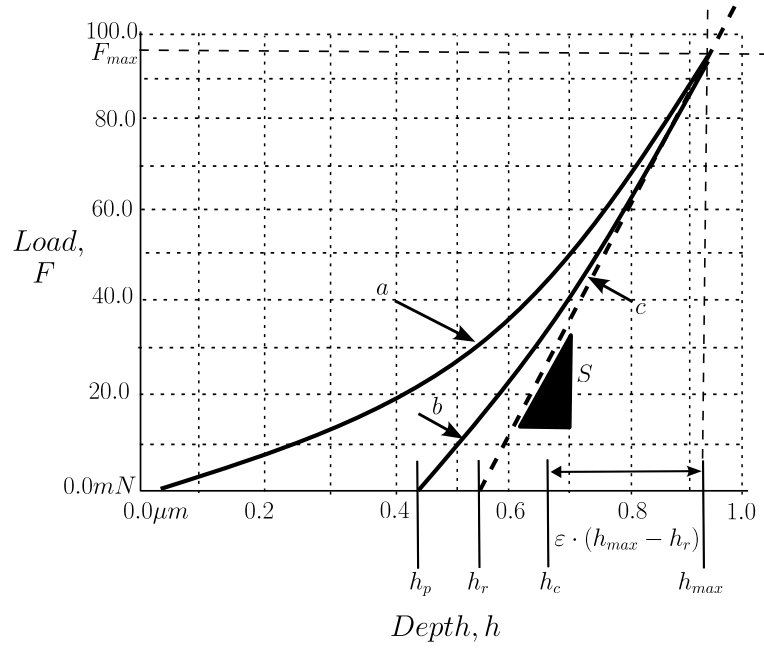


Figure 4.1: Typical indentation curve

Table 4.1: Geometrical parameters according to indenter shape

Indenter Shape	m	ε
Flat Punch	1.0	1.0000
Cone	2.0	0.7268
Sphere	1.5	0.7500

The maximum load and indentation depth of nanoindentation test are obtained from the same acquisition point that is directly on curves. The formulations of geometrical parameters in Figure 4.2 are given as,

$$h_r = h_{max} - \frac{F_{max}}{S} \quad (4.1)$$

$$h_c = h_{max} - \varepsilon \cdot (h_{max} - h_r) \quad (4.2)$$

The permanent indentation depth after removal of the test force, h_p , is determined by linear fit inbetween %15 and %0 of the maximum load according to CSM Instrument's nanoindentation user guide document. The contact stiffness, S, can be obtained by either tangent method or Oliver-Pharr method. In tangent method, S is

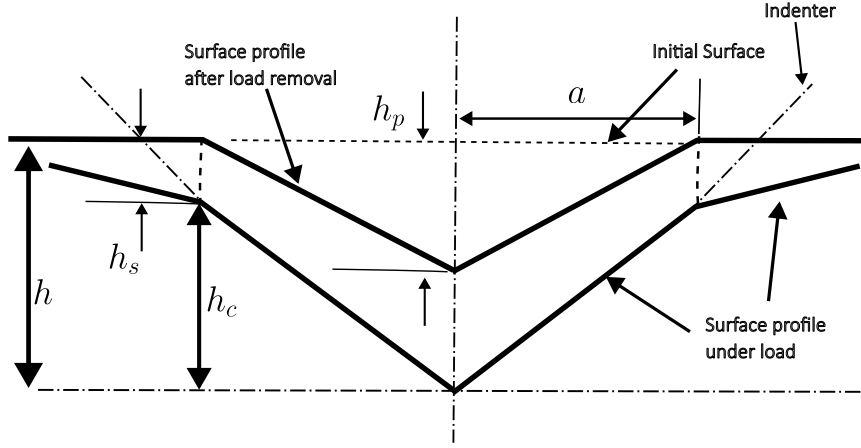


Figure 4.2: Schematic of the indenter-sample contact

determined according to 4.3 by providing a tangent fit which starts at %95 of F_{max} and ends at %70 of F_{max} .

$$S = \frac{dF}{dh} \quad (4.3)$$

In Oliver-Pharr method, power law fit of unloading curve is used to determine stiffness with equations 4.4, 4.5

$$F = F_{max} \cdot \left(\frac{h - h_p}{h_{max} - h_p} \right)^m \quad (4.4)$$

$$S = m \cdot F_{max} \cdot (h_{max} - h_p)^{-1} \quad (4.5)$$

The geometrical parameters m and ε are given with corresponding indenter shapes in Table 5.2. For the elastic modulus, indenter tip properties should be provided in calculations with the depth of contact of the indenter with the sample at maximum load, h_c . The indentation elastic modulus, E_{IT} is given as

$$E_{IT} = \frac{1 - \nu_s^2}{\frac{1}{E_r} - \frac{1 - \nu_i^2}{E_i}} \quad (4.6)$$

where ν_i is Poisson ratio of the indenter (0.07), E_i is the elastic modulus of indenter

(1141 GPa) and ν_s is the Poisson ratio of the sample. E_r is reduced modulus of the indentation contact

$$E_r = \frac{\sqrt{\pi} \cdot S}{2 \cdot \beta \cdot \sqrt{A_p(h_c)}} \quad (4.7)$$

where β is shape dependent geometric factor and $A_p(h_c)$ is the theoretical projected contact area. Standard measurement of hardness, HV is dependent on maximum load and developed contact area, $A_c(h_c)$ as given in 4.8.

$$HV = \frac{F_{max}}{9,81 \cdot A_c(h_c)} \quad (4.8)$$

4.1.1 Test results on GaSb

Elastic modulus and hardness of GaSb has been determined in the temperature range of 1K to 1000K by DFT previously. Nanoindentation experiments are conducted at room temperature on polished and non-polished surface conditioned GaSb samples. Bulk GaSb material surface does not contain any film coating. The dimensions of the prepared sample are $15.0 \times 4.8 \times 0.5 \text{ mm}^3$. The delta slope contact is applied as %80 which is recommended for the hard materials. Low delta slope contacts such as %10 to %20 is desired for soft materials such as epoxies, polymers. A representative load-displacement curve is given in Figure 4.3 for 20mN loading case. The maximum loads of 10 mN and 20 mN are applied during the indentation. Maximum indentation depth is around 500nm for 20mN maximum loading as given in Figure 4.3 whereas it is approximately 320nm for 10mN maximum load case. For each loading, total number of 10 indentation has been performed and box plot results of the indentations for different maximum loads are given in Figure 4.4.

Boxplots basically define a set of five data which are minimum, first quartile, median, third quartile and maximum values. The box limits in Figure 4.4 defines the limits of first and third quartile of elastic modulus values and the horizontal line in the box defines the median of dataset. Besides the experimental studies, the results of DFT calculations performed with LDA and PBEsol approximations are provided as single

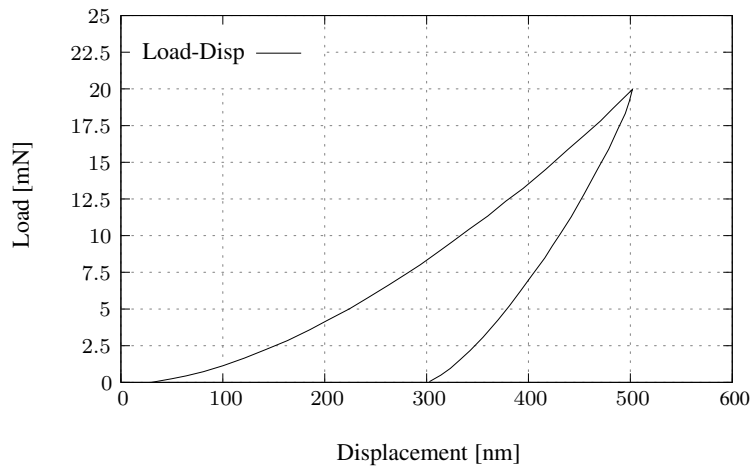


Figure 4.3: Representative load - displacement curve of nanoindentation test on GaSb with maximum applied load of 20mN

lines in the box plot so that comparison of the numerical and experimental results is more comfortable. The results of DFT simulations are covered in detail in Chapter 3.

A typical nanoindentation curve is already given in Figure 4.1. However, the experimental results may not be identical with this behaviour for each and every indentation. For example, a discontinuity during loading phase of indentation that is called as pop in may be observed during nanoindentation. Pop in is defined as a sudden change in load or displacement during the loading of indenter on the sample. Nanoindentation experiments can be performed with two options i.e, one should either control indentation load or displacement. If the indentation is performed with load control, a horizontal plateau or plateau with a positive slope can be observed. On the other hand, if the nanoindentation experiment is performed with displacement control, a vertical drop on force-displacement behavior can be observed. Pop in effect is commonly explained by different topics according to tested materials such as dislocation nucleation for crystalline materials, a result of strain transition near grain boundaries of metals or fracturing of the thin film if a hard brittle film is tested on a ductile substrate material. So, there exist variety of reasons to observe pop in effect. This phenomena is not discussed in detail here and pop in event is not observed on the given data in Figure 4.4.

As seen in Figure 4.4, surface condition of GaSb can affect the elastic modulus

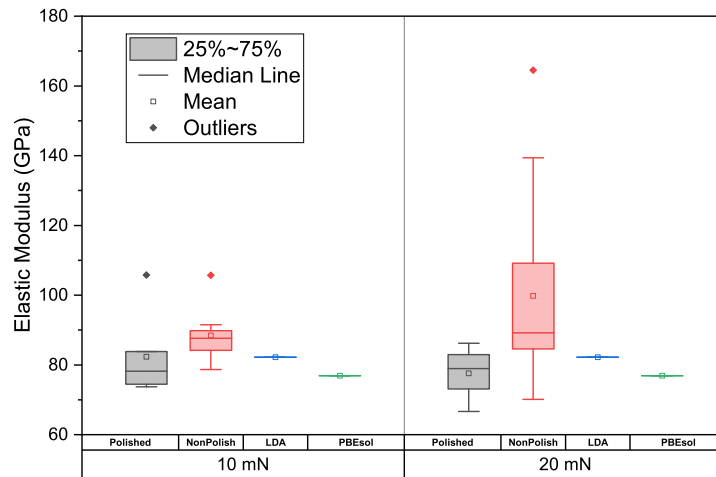
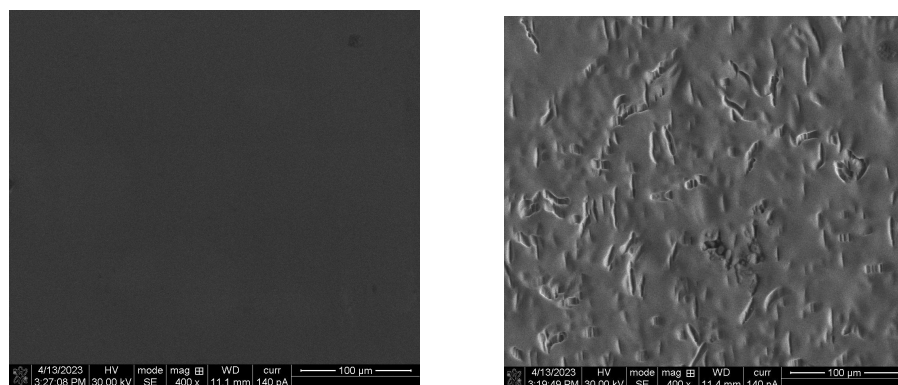


Figure 4.4: Measurements of elastic modulus of polished, non-polished GaSb samples by nanoindentation

results. Results of polished GaSb material shows excellent coherence with the limits of DFT predictions on elastic modulus for both of the maximum indentation loads. On the other hand, non-polished GaSb provides higher elastic modulus with larger scattering of the data. When the maximum indentation load is increased to 20 mN the difference between highest and lowest measured values is more than 90 GPa. Surface conditions of both samples that are captured by SEM are given in Figure 4.5.



(a) Polished surface

(b) Non-polished surface

Figure 4.5: GaSb test sample surfaces

Hardness results are also provided in Figure 4.6. Contrary to the elastic modulus results, both polished and non-polished samples provide good coherence with the room temperature DFT results. For a maximum load of 10 mN and 20 mN, both of the configurations show more scattering data with respect to elastic modulus results. Although DFT results does not stay out of the first and third quartile limits of corresponding boxplots, it is hard to verify that the hardness values determined in a reasonable range due to inconsistent nanoindentation results.

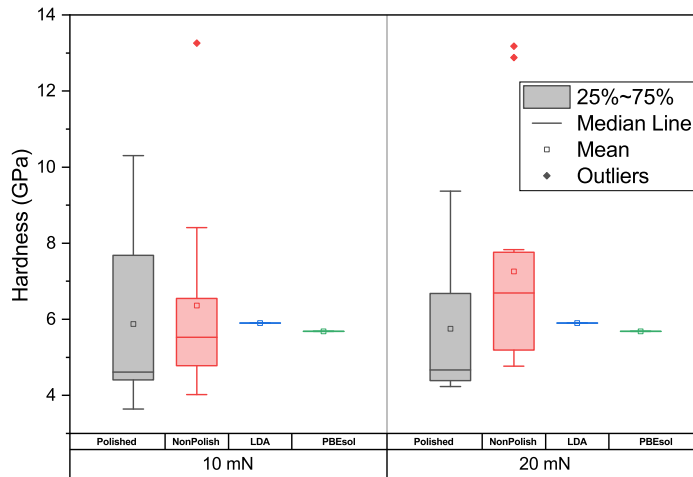


Figure 4.6: Measurements of hardness of polished, non-polished GaSb samples by nanoindentation

Hardness is defined as the resistance of a material to permanent deformation during application of load. This property can show size dependence in materials i.e, the results can vary near the surface with respect to bulk hardness measurements. As it is observed from Figure 4.4 and 4.6, although the elastic modulus measurements by using nanoindentation show great coherence with DFT results, there exists a scattered data for the hardness measurements. The common issue with the hardness determination is the contact area determination which is given in equation (4.8) as $A_c(h_c)$. It is a measured value after indentation. However, the projected contact area, $A_p(h_c)$ in equation (4.7), is a theoretical or calibrated value calculated according to indentation depth, $A_p = f(h)$. The actual contact area can represent a significant difference if the surface is not ideally flat or it shows some topological differences from one

indentation point to another. This may be the cause of scattered data in hardness measurements. Moreover, some materials can exhibit deformation behaviour that can lead to inaccurate contact area determinations. For example, sink-in and pile-up behavior of material during nanoindentation may cause inaccurate contact area determinations [204, 205]. So, an accurate information about the contact area is important while determining a representative hardness value. The experiment involved using two different types of GaSb material based on surface treatment (polished or non-polished) and revealed significant differences in elastic modulus determinations based on surface treatment.

Surface roughness of the samples are also measured with Zygo New View 7100 Optical Profiler which uses scanning white light interferometry to measure and visualize the microstructure and topology of the surfaces. According to given results in Figure 4.7, polished sample has a roughness (rms) value of 0.62nm and peak to valley (PV) value of 19.54nm whereas nonpolished sample has a much greater PV and roughness values of 7820nm and 1031.57nm, respectively.

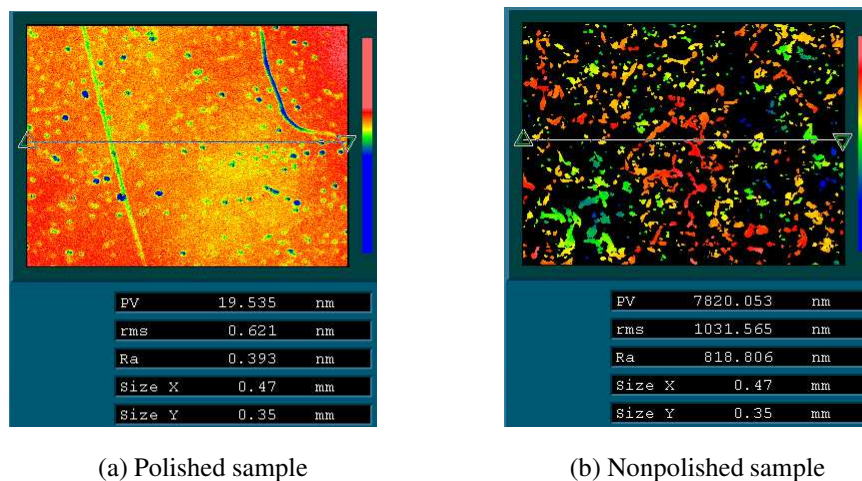


Figure 4.7: Zygo New View 7100 optical profiler measurements on the samples

4.2 Custom Designed Test Setup for Cryocooling

4.2.1 Test setup design

A test setup is designed and produced to perform cryocooling experiments. Aim of obtaining cryogenic temperatures is to mimic IRFPA under its generic operation condition, i.e, at 77K. High vacuum conditions must be satisfied to eliminate convection mode of heat transfer so that obtaining cryogenic temperatures with minimum cooling power can be satisfied. Ease of sample integration, de-integration and reusability of the test setup are also important in terms of effectiveness of the test setup. A schematic structure of the designed test setup is given in Figure 4.8. Test setup is composed of a dry pump, turbo-molecular pump, pressure gage and valve, test envelope which is integrated on a cryocooler, a DC power supply, display unit and required assistive equipments.

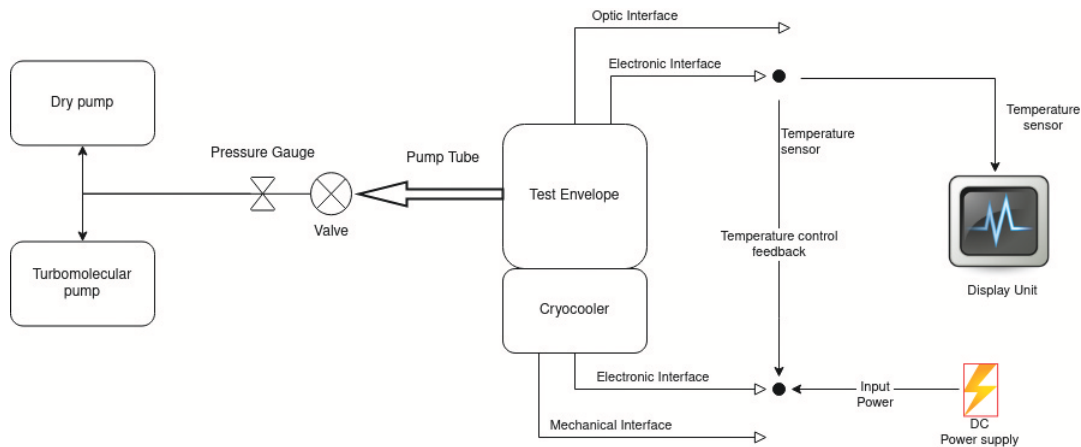


Figure 4.8: Test setup schematic

In the test setup, a rotary type Stirling engine cryocooler [206] has been used to achieve cryogenic temperatures. Pressurized helium is used as cryogenic coolant in the cryocooler. Rotary Stirling cryocooler is integrated with a custom designed test envelope that has two o-ring interfaces to seal interior volume from the exterior as shown in Figure 4.9. Test Envelope is simply a leak tight structure with proper optical and electrical interfaces as shown in Figure 4.8 and 4.9 which indicated as optical window and electrical pins. Mechanical interface of the cryocooler can be

used for mechanical integration and heatsinking.

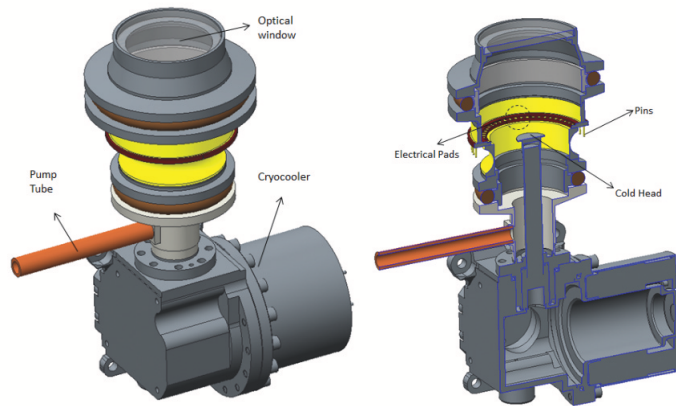


Figure 4.9: Test setup design

Interior volume of the Test Envelope is under vacuum environment by the help of pump tube, dry pump and turbo-molecular pump. A copper pumping tube has been utilized as the vacuum port. The dry pump works as a backup pump and it satisfies the vacuum level inside the housing so that the turbo-molecular pump can start to operate. Viton o-ring material and hermetic material integration processes such as brazing, laser welding has been used in between parts to obtain vacuum integrity of Test Envelope. Standart QF flange features have been used for metal parts which are o-ring sealed. Standart metal clamps have been used to hold metal parts together. The samples that will be tested are placed on a ceramic material that is integrated on top of cold head as shown in Figure 4.9. A temperature sensor which is placed on the ceramic surface is connected to electrical pads via wirebonds as shown in Figure 4.10. Electrical pads are placed on a multilayer ceramic that are used to connect electrical pads to the outer world pins. This way, signal transmittance from the temperature sensor to the outer world and Stirling cryocooler is realized.

Advantages of this setup can be defined as follows;

- Active temperature control of the sample by adjusting the cryocooler operating temperature.

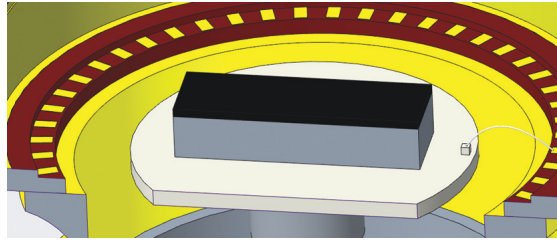


Figure 4.10: Ceramic with an integrated sample on cold head

- Ease of sample mounting or dismounting obtained by using reworkable epoxies and standart QF flanges and clamps.
- Changing optical window without de-integrating any other part, if needed.

Experimental test setup is designed to conduct experiments at cryogenic temperatures. Ceramic material is integrated on cold head with an epoxy material. The sample structure can be integrated on ceramic (white) as shown in Figure 4.10 with thermal interface material. The thermal interface material is not cured so that it does not provide rigid contact between bonded layers. Two temperature diodes are integrated on carrier ceramic, one of them can be observed on Figure 4.10 with a representative wirebond that connects temperature sensor to the electrical pads so that the temperature can be monitored during the experiments. The second temperature diode is used to provide temperature feedback for the cryocooler that is shown in Figure 4.8.

4.2.2 Cryocooling experiments

Cryocooling is required to decrease noise level caused by dark current mechanism of detection layers in IRFPA structure. Generic IRFPA cooled region can be composed of different ceramic, metal, semiconductors that are integrated on each other by using epoxy materials. Due to coefficient of thermal expansion mismatch between constituent materials and great temperature differences, problem of arising thermo-mechanical stresses on IRFPA structures has been previously explained. To mimic thermo-mechanical stress on IRFPA structures, GaSb and CdZnTe semiconductor materials are integrated with stainless steel (SS304) with an epoxy material and integrated on cold head of the custom designed test setup with a thermal interface

material.

4.2.2.1 GaSb - SS304 sample

GaSb and SS304 samples are integrated with an epoxy material. The integrated structure is cooled down to 77K by using a custom designed test setup. The details of the test setup is given in Section 4.2. Temperature of the cold head is controlled with the temperature sensor on the carrier material. After obtaining 77K temperature on cold head, standby time of a minute is waited to ensure semiconductor materials reached steady state. Then, the cryocooler is switched off and waited for reaching temperature of the assembly to room temperature. This assembly is cooled down from room temperature to 77K approximately in 6 minutes. The cooldown of the sample is given in Figure 4.11. Then, a cleaning process of the assembly is performed before inspection with SEM. Rectangular prism geometry is defined for the constituents in dimensions of $15 \times 4.8 \times 0.5 \text{mm}^3$ and $15 \times 4.8 \times 2 \text{mm}^3$ for GaSb and SS304, respectively.

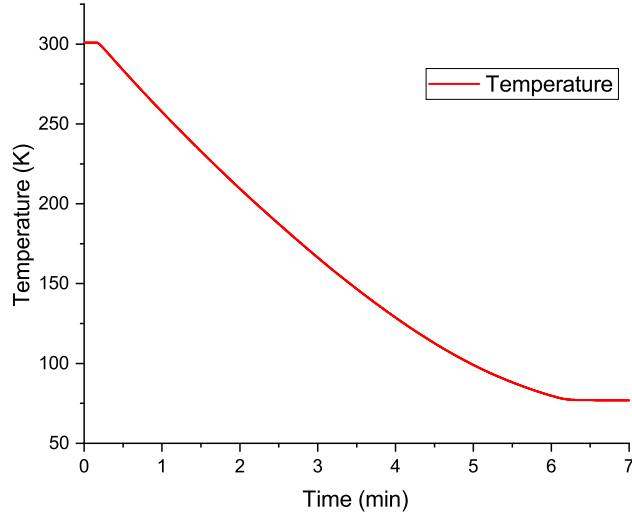
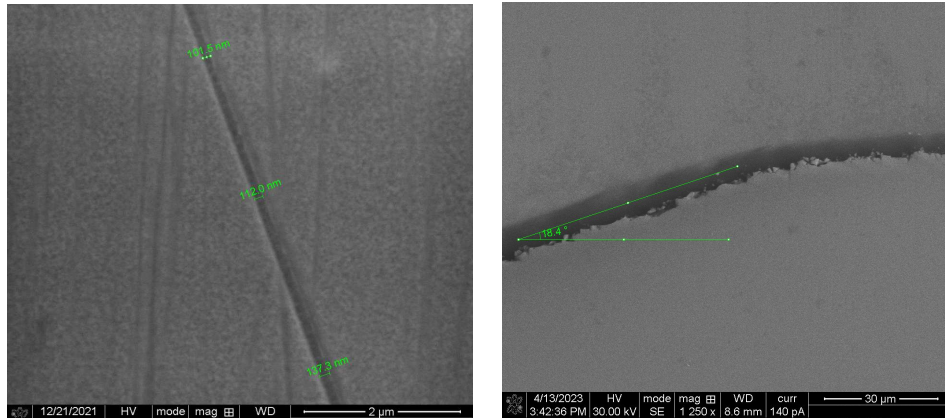


Figure 4.11: Cooldown of the integrated sample

Top surface normal of GaSb sample is on $\langle 100 \rangle$ direction but in plane material orientation was not known. After cryocooling experiment, it is placed in Scanning Electron Microscopy (SEM) and top surface of the sample is investigated. Observed crack pat-



(a) Crack pattern 1

(b) Crack pattern 2

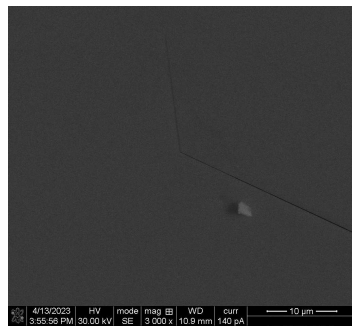
Figure 4.12: Observed cracks on GaSb sample

tern on GaSb is given in Figure 4.12a with a crack width in the range of 100nm to 140nm as observed in Figure 4.12a. In Figure 4.12b, it is observed that the second crack path is changing its direction with an angle of 18.4° . Observation of crack patterns and crack width are obtained with SEM. To determine the cleavage planes of single crystal materials, electron back scattering diffraction (EBSD) method can be used to determine fatigue assessments and crystal misorientation of materials as well as single crystals [207, 208].

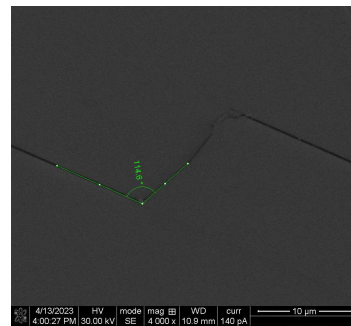
In plane material orientation of the investigated GaSb sample was not controlled during crystal growth phase. So, the crack propagation direction cannot be specified according to in-plane crystal directions of GaSb. Crack propagation on GaSb as a straight line makes an angle between horizontal axis. As it is observed from the results of phase field theory, for example in Figure 6.6, the crack propagation path on GaSb material can be different with respect to changing in plane material orientation which is also valid for other cubic crystals. The constructed structure is analyzed with finite element method on Section 5.1.

4.2.2.2 CdZnTe - SS304 sample

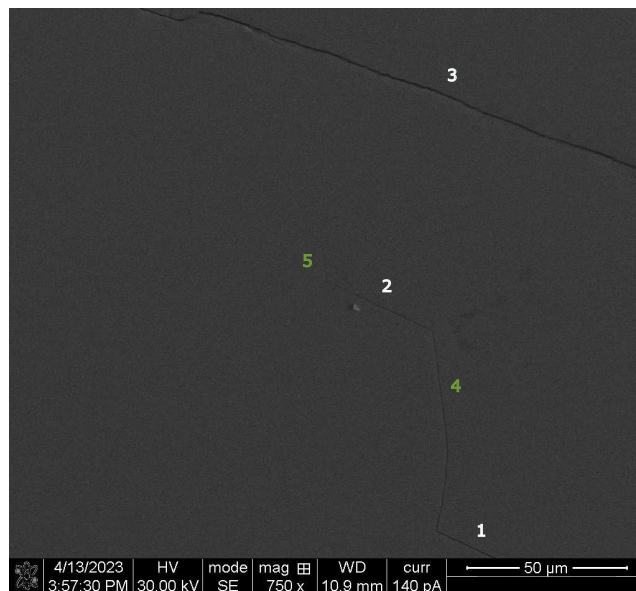
$\text{Cd}_{(1-x)}\text{Zn}_x\text{Te}$ with $x = 0.04$ ternary compound with top surface normal of $\langle 211 \rangle$ direction is commonly used in HgCdTe IRFPA detectors as a substrate material [209, 210]. By applying the exactly same geometric structure and procedure given in Section 4.2.2.1 for CdZnTe instead of GaSb, crack pattern on the ternary compound is able to be observed. CdZnTe is integrated on SS304 sample with an epoxy material. The temperature profile given in Figure 4.11 is also valid for the test of CdZnTe. The top surface of CdZnTe is inspected with SEM at room temperature. The observed crack pattern on CdZnTe material is provided in Figure 4.13.



(a) Crack pattern 1



(b) Crack pattern 2



(c) Crack pattern 3

Figure 4.13: Observed crack on CdZnTe sample

The crack pattern on CdZnTe given in Figure 4.13a shows an angle of 122.5° between two observed directions. A broad capture of observed cracks in Figure 4.13a is given in Figure 4.13c. Two set of paralel cracks are observed in wide view, i.e, crack number 1, 2 and 3 represent paralel crack set 1 whereas crack number 4 and 5 represent paralel set 2. The angle between observed zig-zag crack in Figure 4.13b measured as 114.8° . Zig-zag crack pattern of crack propagation can be observed for cubic anisotropic materials. According to in-plane material orientation or loading type and direction, cubic anisotropic materials may exhibit zig-zag or unidirectional pattern for crack propagation [102]. A decreasing crack width and sharpness is observed by SEM when the crack is propagating and loosing its energy and it almost vanishes at the top end as seen in Figure 4.13b. In contrast to observed crack on GaSb sample in Figure 4.12b, the crack width smaller on CdZnTe material.

The given results in Section 4.2.2.1 and 4.2.2.2 are the first attempts to observe crack propagation paths on GaSb and CdZnTe materials in the literature. Material orientation of both of the materials were not controlled during crystal growth processes because this is not a requirement in IRFPA applications. SEM images from the top surface are provided to observe crack propagation paths on the materials. Although the crack propagation path directly depends on in-plane material orientation, there are other factors such as void defects, precipitations, processing parameters during crystal growth, surface roughness, thermal history of the material that can affect crack initiation and propagation on a single crystal material. In general, minizing the defect density and controlling the microstructure of the material during production can help to improve resistance to crack propagation.

CHAPTER 5

THERMO-ELASTIC STRESS ANALYSIS OF IRFPA WITH FEM

5.1 Thermo-Mechanic Stress Determination on Bimaterial Assembly

The effect of temperature-dependent material properties is introduced with finite element analysis (FEA) on a GaSb-SS304 assembly. Motivation of this study is to show maximum von Mises stress results regarding the usage of different material properties, i.e, temperature-dependent material properties and material properties at 300K.

Coefficient of thermal expansion and elastic modulus of GaSb material are determined by DFT studies and given in Section 3.2.1. Room temperature properties of GaSb given in Table 5.1 are used. The room temperature properties of GaSb are also extracted from DFT results. The used material properties of SS304 are also provided in Table 5.1.

Table 5.1: Material Properties of GaSb and SS304 at 300K

Material	CTE (1/K)	Elastic Modulus (GPa)	Poisson ratio
GaSb	6.87E-06	82.20	0.2422
SS304	17.3E-06	193	0.2900

Rectangular prism geometry is defined for the constituents in dimensions of $15 \times 4.8 \times 0.5 \text{ mm}^3$ and $15 \times 4.8 \times 2 \text{ mm}^3$ for GaSb and SS304, respectively. Due to symmetry, a quarter of the structure is modeled. Anisotropy in GaSb material is omitted in FEA study. Mesh is given in Figure 5.1a and defined path for von Mises stress is provided in Figure 5.1b. The given path is starting on the neutral axis and elongates till the

diagonal edge.

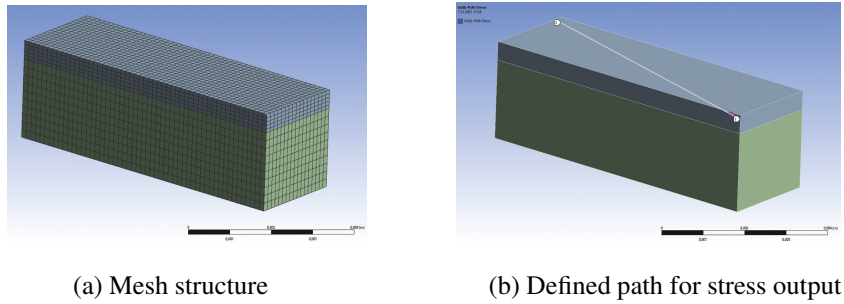


Figure 5.1: a) Mesh structure, b) Defined path on GaSb midplane

Previously determined temperature dependent material properties of GaSb are given. Although heat capacity and coefficient of thermal expansion values are provided with continuous lines in Figure 3.5 and 3.6 respectively, discrete values of material properties for the corresponding temperatures are given in ANSYS R2021.

On symmetry surfaces, displacements in surface normal directions are constrained. All three displacements on bottom vertex of neutral axis of the assembly are also constrained with fixed support. Then, thermal condition of cooling is given on both of the materials from 300K to 77K. Temperature gradient on the structure is not main driving force of this problem so it is omitted. Maximum von Mises stress on the path given in Figure 5.1b is taken as the only output for comparison.

Path stress results on GaSb by using material properties at 300K and by using temperature dependent material properties between 1K and 300K show great differences. Obtained maximum von Mises stress level by using temperature dependent data is 117.61 MPa whereas it is 91.59 MPa when the room temperature material data is used. If the maximum von Mises stress is normalized with respect to the analysis performed by room temperature material data, the maximum von Mises stress difference along the defined path shows 28.41% difference and it is linear except the edge which can be seen in Figure 5.2b.

A simple representation of material property effect on thermo-mechanical stress determination is given in GaSb-SS304 bimaterial assembly. Geometry, constituent material properties are important to determine accurate stress predictions. However, in

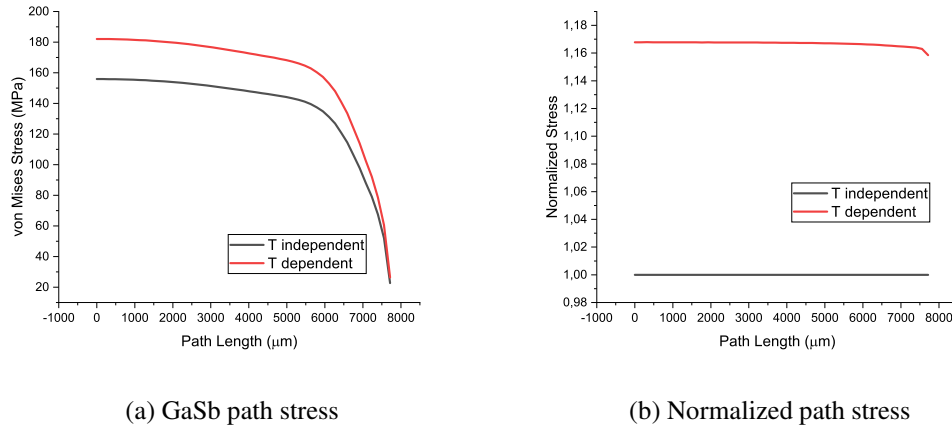


Figure 5.2: The effect of material property definition on von Mises stress determinations via FEM of the two configuration, i.e, materials properties provided only at 300K and temperature dependent material property for 1K-300K temperature range

cooled region of IRFPA structures, there exist different geometries and materials. To observe the effect of temperature dependent material properties much better, performed finite element analysis in this section is repeated on a representative IRFPA assembly structure.

5.2 Thermo-Mechanic Stress Determination on IRFPA Assembly

As an extension of bimaterial assembly, thermo-mechanic stress determination of a representative IRFPA structure is performed. Finite element model consists of five different materials as given in Figure 5.3a. At the bottom, cold finger cap, a metal part is defined as part 1. Carrier which is placed on the metal part is given as 2. Silicon readout integrated circuit, underfill/interconnect material and GaSb semiconductor material that represents the IRFPA are provided with numbers 3,4 and 5 respectively. Interconnects and underfill materials are assumed as a homogeneous layer in the model. Frictionless support is defined on symmetry surfaces such that displacements across the symmetry surfaces are constrained. Bottom vertex of part 1 is fixed in three directions. At the bottom of the cold finger cap material, (part 1), footprint of cold finger tube which is a quarter hollow cylinder as given in Figure 5.3b is fixed in

z-direction (surface normal), but it is not constrained in x-y directions.

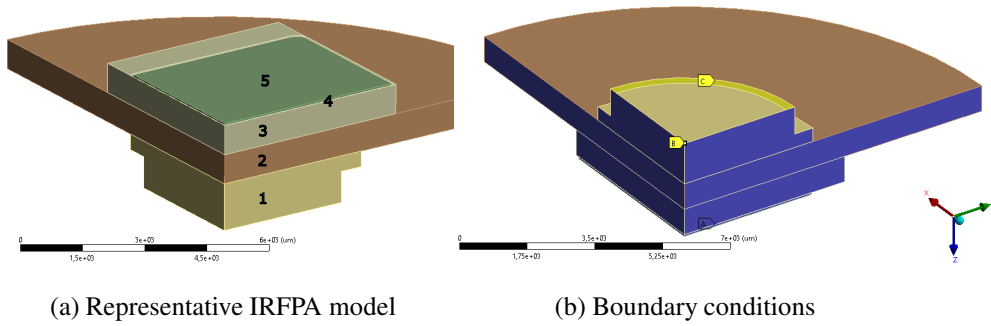


Figure 5.3: IRFPA model and regarding boundary conditions on the structure

Two finite element analysis are performed with exactly the same model geometry, boundary conditions and mesh. Material properties of parts 1,2,3 and 4 are not changed within these simulations. The only difference between the analyses was providing either temperature dependent or single point (at 300K) material properties of IRFPA material. Initial temperature of the whole assembly is 298K. Thermal loading of cooling the assembly to 77K is applied on the structure. Bonded contact is defined between the constituent materials such that delamination or separation is not allowed. The temperature gradient on the assembly is neglected due to utilization of thermally conductive materials and thin layers on the assembly. Driving force in these analysis is the coefficient of thermal expansion mismatch and great temperature difference that IRFPA material must withstand for thousands of thermal cycles.

Table 5.2: Geometric dimensions of parts

Part #	Dimensions in millimeter
1	$\phi = 6.86, t = 0.8$
	$\phi = 8.0, t = 0.4$
2	$\phi = 18.5, t = 0.75$
3	$5 \times 5 \times 0.75$
4	$5.05 \times 5.05 \times 0.005$
5	$4.87 \times 3.91 \times 0.05$

Geometries of the constituent parts are given in Table 5.2. As it is observed, the

material thicknesses is not larger than 1 mm and it is $5\mu\text{m}$ and $50\mu\text{m}$ for underfill and GaSb layers, respectively. Total number of 893402 nodes and 524147 elements are used in the analyses. Very fine mesh is used on the analyses but the computational time is still low in steady state mechanical analysis.

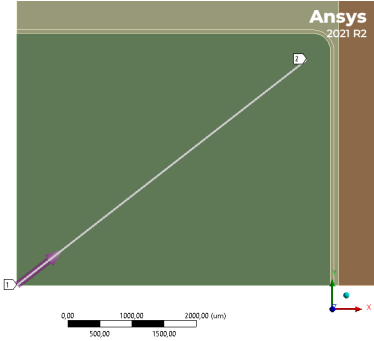
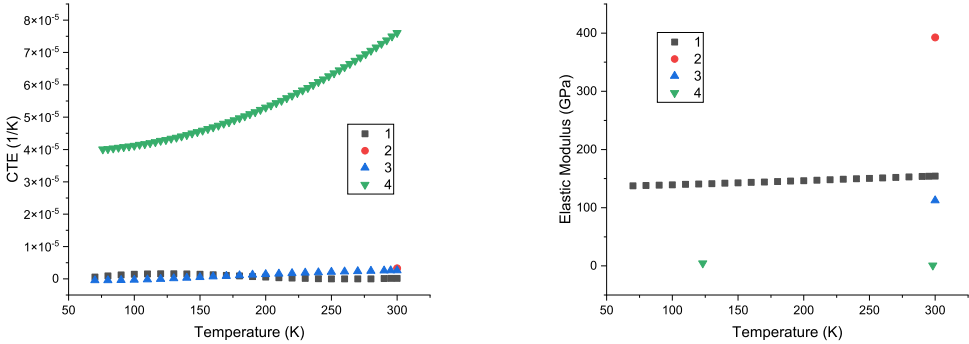


Figure 5.4: Defined path on midplane of GaSb

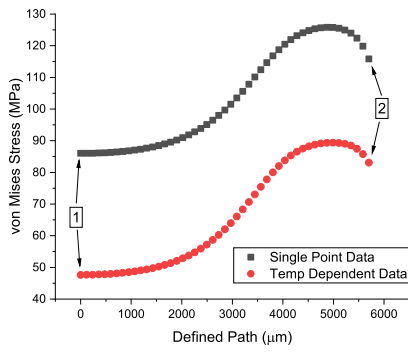


(a) Thermal expansion coefficients of the parts

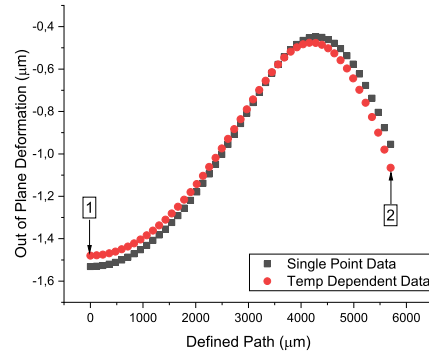
(b) Elastic modulus of the parts

Figure 5.5: Thermal expansion coefficient and elastic modulus parameters of the constituent materials on IRFPA assembly.

To determine the stress and displacement outputs on IRFPA semiconductor layer, a path is defined on midplane of GaSb layer which is given in Figure 5.4. Defined path starts from center axis of the structure and elongates to diagonal edge of GaSb. Single point and temperature material properties of GaSb are already provided in Section 5.1. For the remaining parts, thermal expansion coefficient, elastic modulus and Poisson ratio are given in Figures 5.5a, 5.5b and Table 5.3, respectively.



(a) Von Mises stress on GaSb midplane



(b) Z-axis deformation of GaSb layer

Figure 5.6: Effect of temperature dependent data on von Mises stress and out of plane deformation for defined path.

Table 5.3: Poisson ratio of the parts

Part 1	Part 2	Part 3	Part 4
0.400	0.228	0.280	0.317

Developed thermo-mechanical stress is determined along the defined path given in Figure 5.4. According to results of the two analyses that are obtained with either single point temperature data or temperature dependent material data of GaSb, von Mises stress results are given in Figure 5.6a. Out of plane deformation of GaSb top surface is given in Figure 5.6b.

Using temperature dependent material data for GaSb material provides 44.7% improvement in von Mises stress determinations. In contrast, out of plane surface deformation on top surface of GaSb behaves very similar in these two cases. It is a clear evident that when the IRFPA structure is exposed to cyclic thermal loading during the device lifetime, using right material properties can significantly affect the thermo-mechanic stress response so the lifetime estimation of the structure. In the Section 5.1 and 5.2, it is showed that thermo-mechanic stress evaluation accuracies are improved with the use of temperature dependent material properties with 44.7% and 28.41% accordingly. The improvement margins could be even higher depending on

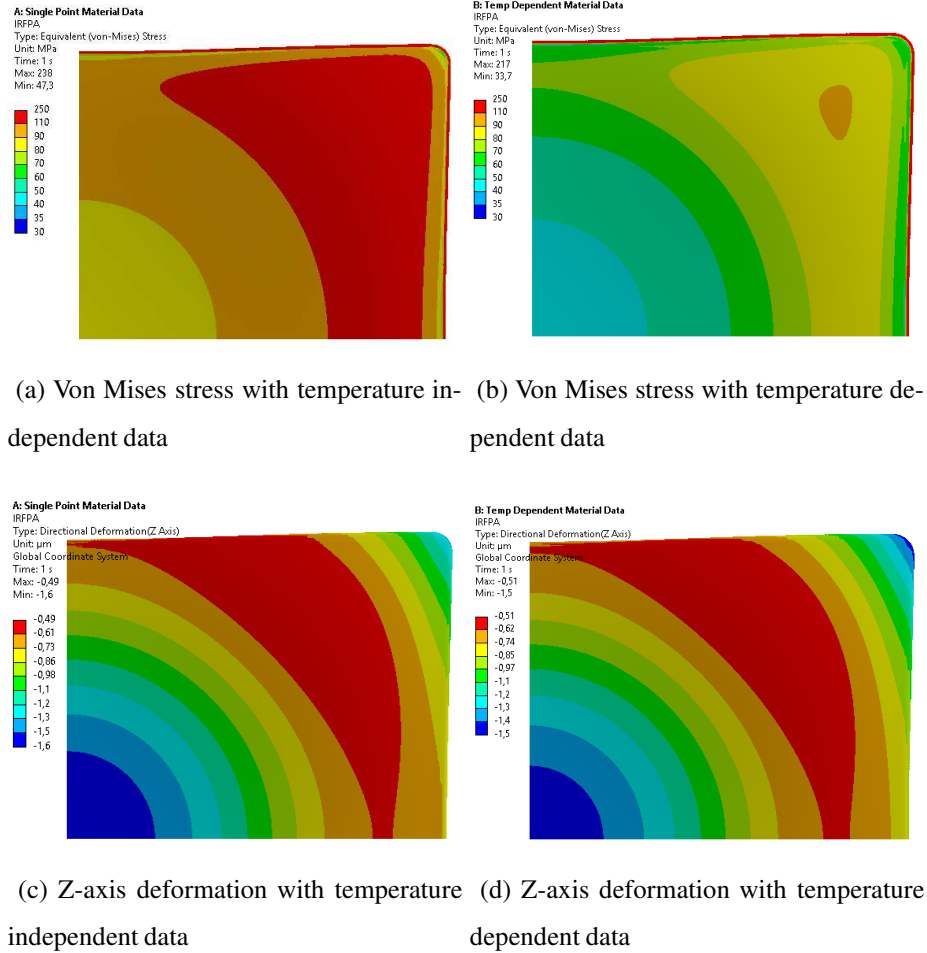


Figure 5.7: Effect of single point material data and temperature dependent data. a), b) represents the effect on von Mises stress, c), d) represents the out of plane deformation results.

the constituent materials of the assembly.

5.3 Free Energy Function and Stress Expression

In this section, free energy function and stress expression for cubic anisotropic materials are derived. Free energy function is divided into two parts, i.e, isotropic and anisotropic parts. Mechanical part of the free energy is derived for cubic symmetric materials and the definitions of stress expression, elasticity tensor are also provided. Then, free energy of a anisotropic thermo-elastic solid for cubic symmetry is given.

For GaSb and InSb materials, a polynomial fit is provided for Lamé parameters and cubic anisotropy parameter which can be used in cubic symmetric free energy determinations of these materials. R-square parameter which shows the quality of the fits, is greater than 0.99 for all of the performed curve fittings.

5.3.1 Cubic anisotropy

The mechanical part of the free energy function for a crystal with cubic symmetry is described as

$$\Psi(\boldsymbol{\varepsilon}, \mathbf{M}_i, \theta) = \Psi_{\text{iso}}(\boldsymbol{\varepsilon}, \theta) + \Psi_{\text{sym}}(\boldsymbol{\varepsilon}, \mathbf{M}_i, \theta) \quad (5.1)$$

where $\mathbf{M}_i = \mathbf{a}_i \otimes \mathbf{a}_i$ with $i = \{1, 2, 3\}$ are the structural tensors associated with the cube faces possessing unit normals \mathbf{a}_i . Herein, we have decomposed the free energy function into isotropic and additional stiffness terms in cube orientations due to cubic symmetry. The isotropic part of the free energy function reads

$$\Psi_{\text{iso}}(\boldsymbol{\varepsilon}, \theta) = \frac{\lambda(\theta)}{2} (\text{tr } \boldsymbol{\varepsilon})^2 + \mu(\theta) \boldsymbol{\varepsilon} : \boldsymbol{\varepsilon} \quad (5.2)$$

where $\lambda(\theta)$ and $\mu(\theta)$ are the temperature-dependent Lamé parameters. Herein $(:)$ is the double contraction operator such that for two second order tensors \mathbf{A} and \mathbf{B} , the double contraction reads

$$\mathbf{A} : \mathbf{B} = A_{ij} B_{ij} \quad (5.3)$$

The additional term of the free energy function due to cubic symmetry reads

$$\Psi_{\text{sym}}(\boldsymbol{\varepsilon}, \mathbf{M}_i, \theta) = \sum_{i=1}^3 \frac{\gamma(\theta)}{2} (\boldsymbol{\varepsilon} : \mathbf{M}_i)^2 \quad (5.4)$$

with $\gamma(\theta)$ as the additional modulus term due to cubic crystal structure. The stress expression then has the following form

$$\boldsymbol{\sigma} = \lambda(\theta) \text{tr } \boldsymbol{\varepsilon} \mathbf{1} + 2\mu(\theta) \boldsymbol{\varepsilon} + \sum_{i=1}^3 \gamma(\theta) (\boldsymbol{\varepsilon} : \mathbf{M}_i) \mathbf{M}_i. \quad (5.5)$$

The fourth order elasticity tensor can be derived from the stress tensor as follows

$$\mathbb{C} = \lambda(\theta) \mathbf{1} \otimes \mathbf{1} + 2\mu(\theta) \mathbb{I} + \sum_{i=1}^3 \gamma(\theta) \mathbb{E}_i, \quad (5.6)$$

where \mathbb{I} is the fourth-order identity tensor $\mathbb{I}_{ijkl} = \delta_{ik}\delta_{jl} + \delta_{il}\delta_{jk}$ and $\mathbb{E}_i = \mathbf{M}_i \otimes \mathbf{M}_i$ is the structural tensor associated with the cube faces. The elasticity tensor of a cubic symmetric crystal in matrix notation with the Voigt convention reads

$$\hat{\mathbb{C}} = \begin{bmatrix} C_{11} & C_{12} & C_{12} & & & \\ C_{12} & C_{11} & C_{11} & & & \\ C_{12} & C_{12} & C_{11} & & & \\ & & & C_{44} & & \\ & & & & C_{44} & \\ & & & & & C_{44} \end{bmatrix}. \quad (5.7)$$

By comparing (5.6) and (5.7), we conclude that

$$\gamma = C_{11} - 2C_{44} - C_{12} \quad \mu = C_{44} \quad \lambda = C_{12}. \quad (5.8)$$

Herein, μ and λ are the shear modulus and the first Lamé constant, respectively. Due to crystal symmetry, the number of nonzero independent elements are reduced significantly. The rank-four tensor notation can then be conveniently reduced to rank-two notation. For cubic crystals, the relation between the three independent nonzero rank-two and rank-four elastic constants is

$$C_{11} = C_{iiii} \quad \text{and} \quad C_{12} = C_{iijj} \quad i \neq j$$

where $i, j = 1, 2, 3$. In this short-hand notation, also known as the Voigt notation, the so-called engineering strain must be used ($\epsilon_{ii} = \epsilon_i$ ($i = 1, 2, 3$), $\epsilon_4 = 2\epsilon_{23}$, $\epsilon_5 = 2\epsilon_{31}$, $\epsilon_6 = 2\epsilon_{12}$). The parameter γ vanishes for isotropic elastic materials leading to $2C_{44} = C_{11} - C_{12}$. For further information regarding admissible set of symmetries for the elasticity tensor and the resulting number of independent elastic constants, it is referred to Chadwick *et al.* [211].

5.3.2 Thermo-elastic cubic anisotropy

To define free energy for a cubic anisotropic thermo-elastic solid, the free energy, Ψ is rewritten by including isotropic (5.2 and cubic symmetry (5.4) parts as follows

$$\Psi(\boldsymbol{\varepsilon}, \theta) = \frac{\lambda(\theta)}{2}(\text{tr } \boldsymbol{\varepsilon})^2 + \mu(\theta)\boldsymbol{\varepsilon} : \boldsymbol{\varepsilon} + \sum_{i=1}^3 \frac{\gamma(\theta)}{2}(\boldsymbol{\varepsilon} : \mathbf{M}_i)^2 + \beta(\theta - \theta_0) \text{tr } \boldsymbol{\varepsilon} - \frac{c}{2\theta_0}(\theta - \theta_0)^2 \quad (5.9)$$

with β , stress-temperature modulus for isotropy, and specific heat, c is positive ($c > 0$). λ , μ , and γ are the Lamé coefficients and the anisotropic coefficients that describe the mechanical properties of the material. The term $\frac{\lambda(\theta)}{2}(\text{tr } \boldsymbol{\varepsilon})^2$ represents the volumetric (dilatational) part of the mechanical energy, while $\mu(\theta)\boldsymbol{\varepsilon} : \boldsymbol{\varepsilon}$ represents the deviatoric part of the mechanical energy. The term $\frac{\gamma(\theta)}{2}(\boldsymbol{\varepsilon} : \mathbf{M}_i)^2$ represents the contribution of the material's anisotropy, where \mathbf{M}_i are the three orthogonal axes of the crystal lattice. $\beta(\theta - \theta_0)\text{tr } \boldsymbol{\varepsilon}$ represents the contribution of thermal expansion to the free energy. $-\frac{c}{2\theta_0}(\theta - \theta_0)^2$ represents the contribution of thermal energy to the free energy. Overall, this expression in (5.9) represents a free energy function that accounts for both mechanical anisotropy and thermal effects in a solid material. Then, the stress expression then has the following form

$$\boldsymbol{\sigma} = \lambda(\theta) \text{tr } \boldsymbol{\varepsilon} \mathbf{1} + 2\mu(\theta)\boldsymbol{\varepsilon} + \sum_{i=1}^3 \gamma(\theta)(\boldsymbol{\varepsilon} : \mathbf{M}_i)\mathbf{M}_i + \beta(\theta - \theta_0)\mathbf{1}. \quad (5.10)$$

The entropy, η and heat flux, \mathbf{q} can be given as

$$\eta = -\frac{\partial \Psi}{\partial \theta} = -\beta \text{tr } \boldsymbol{\varepsilon} + \frac{c}{\theta_0}(\theta - \theta_0), \quad (5.11)$$

$$\mathbf{q} = -k\nabla\theta, \quad (5.12)$$

where thermal conductivity, k must be positive, $k > 0$. It is assumed that thermal conductivity of the solid is isotropic. Moreover, the heat source or heatsink vector in thermoelasticity that describes any internal heat generation or absorption due to material deformation is omitted in this framework.

Table 5.4: Rational curve fitting parameters as stated in (5.8),(5.13) for elastic constants of GaSb with goodness of fit parameter of R-sq.

Elastic constants of GaSb			
	$\mu(\theta)$	$\lambda(\theta)$	$\gamma(\theta)$
n_1	$+2.846E - 5$	$+2.633E - 7$	$+1.792E - 6$
n_2	$-1.002E - 1$	$-5.927E - 3$	$+1.740E - 3$
n_3	$+5.759E + 1$	$+3.909E + 1$	$-3.815E + 1$
n_4	$+1.956E + 6$	$+7.035E + 3$	$-2.076E + 4$
d_1	$+4.647E + 4$	$+1.834E + 2$	$+5.493E + 2$
R-sq	$+9.959E - 1$	$+9.999E - 1$	$+9.934E - 1$

5.3.3 The Lamé and γ parameters of GaSb and InSb

According to obtained results of second order elastic constants by DFT, the Lamé parameters (μ, λ) including the additional modulus term due to cubic symmetry (γ) as given in (5.8) for GaSb and InSb materials are obtained from 1K to 1000K. The results can be seen in Figure 5.8. A rational curve fitting for temperature dependence of elastic constants with a numerator degree of three and denominator degree of one

$$f(\theta) = \frac{n_1\theta^3 + n_2\theta^2 + n_3\theta + n_4}{\theta + d_1} \quad (5.13)$$

is fitted to the simulation results obtained. The parameters for the elastic constants of GaSb are depicted in Table 5.4.

Lamé parameters of GaSb can be defined with R-square value of larger than 0.99 for all the cases. Sum of squared errors (SSE) which is another goodness of fit parameter is 0.011, 0.033, 0.051 for the estimation of μ, λ, γ parameters. For InSb, the Lamé fit parameters are provided in Table 5.5. R-sq values of these fits are also greater than 0.99. SSE values of 0.00056, 0.0034, 0.0025 occurs while determining μ, λ, γ parameters of InSb.

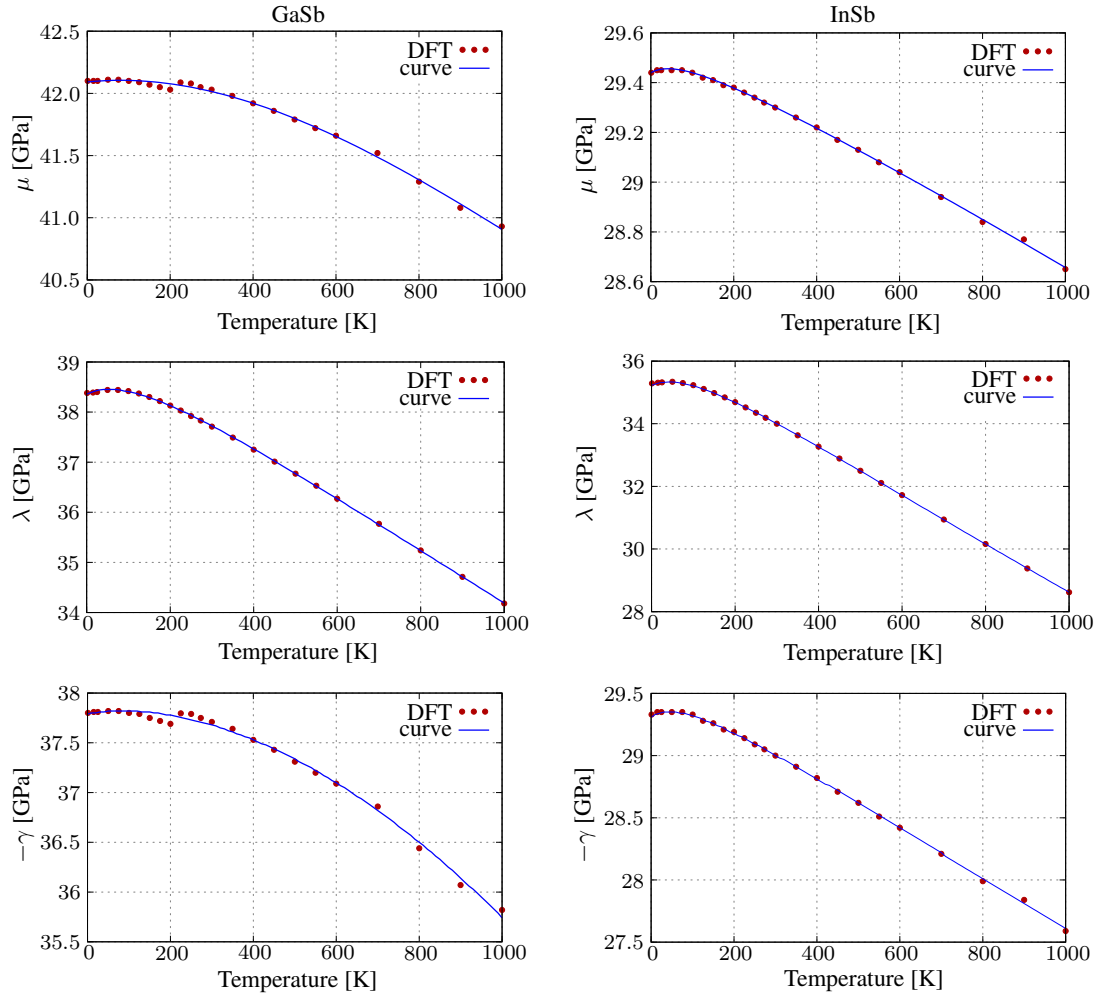


Figure 5.8: Shear modulus μ , first Lamé parameter λ and the cubic symmetry parameter γ for (left) GaSb and (right) InSb are determined according to (5.8) by using the second order elastic constants C_{11} , C_{12} , C_{44} , and depicted (red) dots. The rational curves according to the parameters provided in Tables 5.4 and 5.5 for GaSb and InSb, respectively, are depicted with (blue) lines,

Table 5.5: Rational curve fitting parameters of InSb according to (5.8),(5.13) with goodness of fit, R-sq.

Elastic constants of InSb			
	$\mu(\theta)$	$\lambda(\theta)$	$\gamma(\theta)$
n_1	$-5.246E - 8$	$+6.648E - 7$	$-4.944E - 8$
n_2	$-8.960E - 4$	$-9.065E - 3$	$+2.161E - 3$
n_3	$+2.953E + 1$	$+3.609E + 1$	$-2.954E + 1$
n_4	$+2.818E + 3$	$+4.966E + 0$	$-3.063E + 3$
d_1	$+9.572E + 1$	$+1.410E + 0$	$+1.045E + 2$
R-sq	$+9.996E - 1$	$+9.999E - 1$	$+9.996E - 1$

CHAPTER 6

PHASE FIELD THEORY

6.1 Introduction

The results of DFT analysis provide thermal expansion coefficient, lattice constant, second order elastic constants as well as Vicker's hardness, Poisson ratio etc. Semiconductor compounds may expose to thermo mechanical stresses due to different conditions such as microfabrication processes, operation and storage conditions. In this study, the investigated single crystals by DFT generally have brittle behavior at room temperature as well as at cryogenic temperatures. The mechanical behavior of III-V and II-VI single crystals can also be affected by factors such as temperature, loading rate, doping etc. Since single crystal silicon is widely used in solar cell and MEMS industries, thermo-mechanical and fracture properties of this material is of great importance to build MEMS based microphones, accelerometers, pressure sensors etc [212]. However, there does not exist a study that covers fracture of III-V and II-V semiconductor compounds with experiments and numerical investigations. In this section, a phase field model is developed such that it covers cubic anisotropic behaviour of single crystal compounds and obtaining the fracture patterns of GaSb material with case studies. So, a complete framework including material property determinations by DFT and numerical investigations of crack initiation and propagation will be given for specific single crystal semiconductors.

Cohesive Zone Method (CZM) [88, 89, 90] and eXtended Finite Element Method (XFEM) [85, 86, 87] are widely used on crack propagation, delamination problems of broad range of materials. Phase Field Model (PFM) represents the fracture pro-

cess as a continuous field, which enables the simulation of gradual crack growth and crack coalescence. In contrast, CZM and XFEM represent the fracture process as a discontinuous field, which can make it difficult to model gradual crack growth and coalescence. PFM can simulate complex crack patterns, including branching and merging, without requiring a priori knowledge of the crack path. There are also some limitations and challenges associated with phase field fracture modeling, such as the need for complex parameter calibration and the computational expense of the method. In this thesis, PFM is used to simulate crack initiation and propagation studies.

6.2 Basics of the Phase Field Model of Fracture

The mechanical response and phase field response of a fracture problem are respectively governed by the crack phase field, represented by d , and the deformation map, represented by φ . A framework will be presented to include anisotropy for cubic symmetric crystals, which includes the semiconductor compounds belonging to the III-V and II-VI group materials that exhibit cubic symmetry. To account for this anisotropy class, a proposed phase field model is required.

Let $\mathcal{B} \subset \mathcal{R}^3$ be the reference (undeformed) configuration of a material body with 3D space dimension and $\partial\mathcal{B}$ its boundary with material point $\mathbf{X} \in \mathcal{B}$. The continuum body is at reference configuration at time $t_0 \in \mathcal{T} \subset \mathbb{R}$ and it is in deformed configuration at time $t \in \mathcal{T} \subset \mathbb{R}$. The spatial configuration is represented by $\mathcal{S} \subset \mathbb{R}^3$. The deformation field maps each material point, $\mathbf{X} \in \mathcal{B}$ in Lagrangian configuration onto its Eulerian, deformed, counterpart $\mathbf{x} \in \mathcal{S}$

$$\varphi_t(\mathbf{X}) : \begin{cases} \mathcal{B} \times \mathcal{T} & \rightarrow \mathcal{S} \\ (\mathbf{X}, t) & \mapsto \mathbf{x} = \varphi(\mathbf{X}, t) \end{cases} \quad (6.1)$$

Crack phase field defines the material state as intact ($d = 0$), fractured ($d = 1$) or damaged ($0 < d < 1$)

$$d : \begin{cases} \mathcal{B} \times \mathcal{T} & \rightarrow [0, 1] \\ (\mathbf{X}, t) & \mapsto d(\mathbf{X}, t) \end{cases} \quad (6.2)$$

Deformation gradient, \mathbf{F} , describes the mapping of unit Lagrangian line element $d\mathbf{X}$ onto its Eulerian counterpart $d\mathbf{x} = \mathbf{F}d\mathbf{X}$. Gradient operators, $\nabla(\bullet)$ and $\nabla_x(\bullet)$ define the gradient with respect to reference \mathbf{X} and spatial \mathbf{x} coordinates, respectively. The mapping between infinitesimal reference volume element onto related spatial volume element is performed with the Jacobian ($J = \det \mathbf{F} > 0$). Left and right Cauchy-Green tensors are given as follows

$$\mathbf{C} = \mathbf{F}^T \mathbf{g} \mathbf{F}, \quad \mathbf{b} = \mathbf{F} \mathbf{G}^{-1} \mathbf{F}^T, \quad (6.3)$$

with the covariant reference and spatial metric tensors $\mathbf{G} = \delta_{IJ} \mathbf{E}^I \otimes \mathbf{E}^J$ and $\mathbf{g} = \delta_{ij} \mathbf{e}^i \otimes \mathbf{e}^j$, respectively, where δ_{IJ} and δ_{ij} are Kronecker delta functions in the Cartesian coordinate system. The free energy function of isotropic solids can be determined by three invariants I_1, I_2, I_3

$$I_1 = \text{tr } \mathbf{b}, \quad I_2 = \frac{1}{2} [I_1^2 - \text{tr}(\mathbf{b}^2)], \quad I_3 = \det \mathbf{b} \quad (6.4)$$

Anisotropy is defined with directional dependence of the property in solid mechanics. As opposed to isotropy that means homogeneous behaviour of a property in all directions, anisotropy provides information about the nature of the material. For example, if the strength of a material has a bias toward one particular direction then the material is said to have uniaxial anisotropy which is the case for unidirectional reinforced polymer matrix composites. The matrix material is generally isotropic. By adding fibers, uniaxial anisotropy can be produced according to desired material behaviour.

For unidirectional anisotropy, a single unit reference vector, f_0 and its spatial counterpart, f need to be defined as such

$$\mathbf{f} = \mathbf{F} \mathbf{f}_0 \quad (6.5)$$

together with single Lagrangian and Eulerian structure tensor

$$\mathbf{A} = \mathbf{f}_0 \otimes \mathbf{f}_0 \quad \text{and} \quad \mathbf{A}_f = \mathbf{f} \otimes \mathbf{f} \quad (6.6)$$

For cubic anisotropy, orthogonal basis system needs to be identified with three directional anisotropy. So, unit reference vectors and their spatial counterparts as well as Lagrangian and Eulerian structure tensors need to be multiplied with a factor of three for cubic anisotropy.

$$\mathbf{f}_{1e} = F \mathbf{f}_1, \quad \mathbf{f}_{2e} = F \mathbf{f}_2, \quad \mathbf{f}_{3e} = F \mathbf{f}_3 \quad (6.7)$$

Related second order structure tensors are also given as

$$\mathbf{A}_1 = \mathbf{f}_1 \otimes \mathbf{f}_1, \quad \mathbf{A}_2 = \mathbf{f}_2 \otimes \mathbf{f}_2, \quad \mathbf{A}_3 = \mathbf{f}_3 \otimes \mathbf{f}_3 \quad (6.8)$$

where f_i and f_{ie} for $i = 1, 2, 3$ are Lagrangian and Eulerian vectors, respectively. \mathbf{A}_i for $i = 1, 2, 3$ represent structural tensors of cubic anisotropy.

A discontinuity occurs between intact and broken states of the material for a sharp crack as described in Figure 6.1a. Definition of crack for second order phase field modeling is given in Figure 6.1b. C_0 continuous profile of crack representation is used where the damage field, d provides information about material state, i.e, $d = 0$ (intact), $0 < d < 1$, (damaged) and $d = 1$ (broken). Length scale parameter is represented by l and regularization profile of the exponential function is used with $d = \exp[-|x|/l]$.

Coupled solution of mechanical field and crack phase field is performed in phase field analysis. Dirichlet and Neumann type boundary conditions of mechanical field which are represented in Figure 6.2a are given as $\varphi = \bar{\varphi}$ and $P \cdot N = \bar{T}$ respectively. On the other hand, Neumann type of boundary condition for crack phase field that is provided in Figure 6.2b is given as $\mathcal{L} \nabla d \cdot N = 0$. Sharp crack surface at time t is defined by

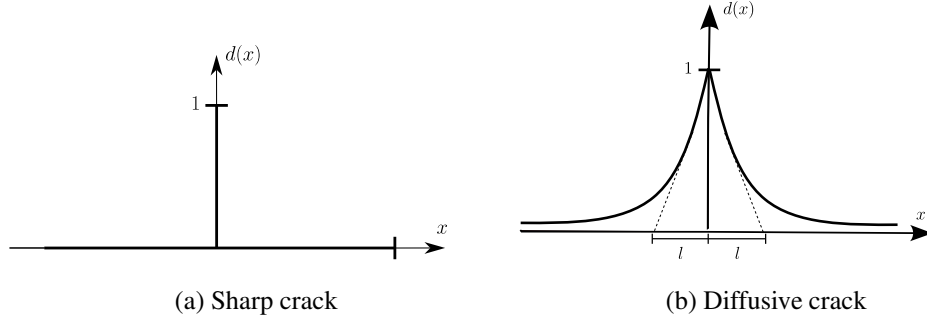


Figure 6.1: Definitions of crack with damage field, d where $d = 0$ represents intact state and $d = 1$ is broken state (a) Sharp crack, (b) Diffusive crack

$\Gamma(d) \subset \mathbb{R}^2$ in the solid \mathcal{B} with a surface integral $\Gamma(d) = \int_{\Gamma} dA$. Phase field model represents the sharp crack surface with a volume integral instead of surface integral by creating a regularized crack surface $\Gamma_l(d)$ such that

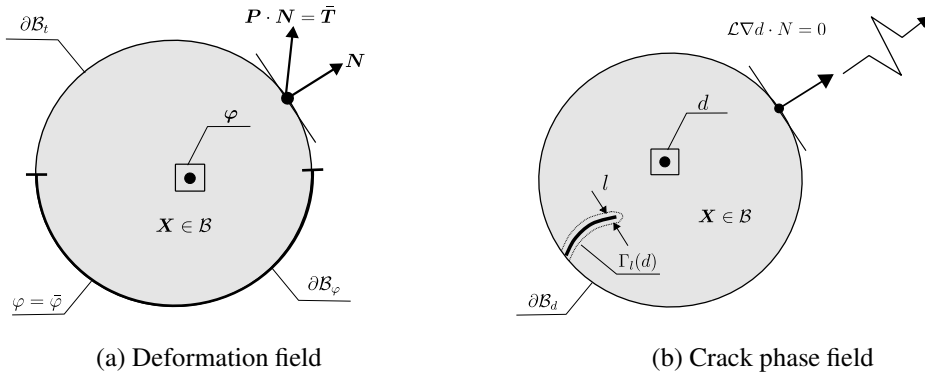


Figure 6.2: Deformation field and crack phase field

$$\Gamma_l(d) = \int_{\mathcal{B}} \gamma(d, \nabla d) dV \quad (6.9)$$

where $\gamma(d, \nabla d)$ represents the isotropic crack surface density function

$$\gamma(d, \nabla d) = \frac{1}{2l} (d^2 + l^2 \nabla d \cdot \nabla d) \quad (6.10)$$

that satisfies the condition of $\gamma(d, \mathbf{Q} \nabla d) = \gamma(d, \nabla d), \forall \mathbf{Q} \in \mathcal{O}(3)$. The tensor, \mathbf{Q} , represents the rotations in the orthogonal group, $\mathcal{O}(3)$. Length scale parameter that

controls width of the crack is represented by l . Regularized crack surface functional can be extended to cover anisotropy classes as such

$$\Gamma_l(d) = \int_{\mathcal{B}} \gamma(d, \nabla d; \mathcal{L}) dV \quad (6.11)$$

where anisotropic crack surface density is

$$\gamma(d, \nabla d; \mathcal{L}) = \frac{1}{2l} (d^2 + \nabla d \cdot \mathcal{L} \nabla d) \quad (6.12)$$

with the condition $\gamma(d, \mathbf{Q} \nabla d) = \gamma(d, \nabla d), \forall \mathbf{Q} \in \mathcal{G} \subset \mathcal{O}(3)$. \mathcal{G} stands for a symmetry group as a subset of $\mathcal{O}(3)$. According to given formulation of the crack surface density function, the second order anisotropic structural tensor, \mathcal{L} can be defined according to desired material symmetry condition. For example, unidirectional anisotropy with the isotropic part can be stated as follows

$$\mathcal{L} = \underbrace{l^2 \mathbf{I}}_{\text{Isotropic part}} + \underbrace{l^2 \omega_{f_0} \mathbf{f}_0 \otimes \mathbf{f}_0}_{\text{Anisotropic part}} \quad (6.13)$$

where ω_{f_0} represents the anisotropy parameter that controls the strength of the anisotropy.

6.2.1 Euler-Lagrange equations of the phase field model

Boundary of the problem domain can be divided into Dirichlet and Neumann-type boundaries such that $\partial \mathcal{B} = \partial \mathcal{B}^d \cup \partial \mathcal{B}^q$ and $\partial \mathcal{B}^d \cap \partial \mathcal{B}^q = \emptyset$. The minimization principle can be stated as

$$d(\mathbf{X}) = \text{Arg} \left\{ \inf_{d \in \mathcal{W}} \Gamma_l(d) \right\} \quad (6.14)$$

with the Dirichlet type boundary condition

$$\mathcal{W} = \left\{ d \mid d(\mathbf{X}) \in \mathcal{B} \wedge d = \tilde{d} \text{ on } \partial \mathcal{B}^d \right\} \quad (6.15)$$

Intact state of the material is described as $\tilde{d} = 0$ and broken state is represented with $\tilde{d} = 1$. The Euler-Lagrange equations are obtained after investigating the minimization principle as

$$\begin{aligned} \frac{1}{\Gamma}[d - \text{Div}(\nabla d)] &= 0 \text{ in } \mathcal{B}, \\ \nabla d \cdot \mathbf{N} &= 0 \text{ on } \partial\mathcal{B}, \end{aligned} \quad (6.16)$$

In equation 6.16, \mathbf{N} represents the unit normal outward on the boundary surface in the reference configuration. Divergence term interpolates the damage field between fresh and cracked states.

To determine anisotropic fracture with the surface density function includes a second order structural tensor \mathbf{M} , the first order phase field approach can be defined as

$$\begin{aligned} \frac{1}{\Gamma}[d - \text{Div}(\mathbf{M}\nabla d)] &= 0 \text{ in } \mathcal{B}, \\ \mathbf{M}\nabla d \cdot \mathbf{N} &= 0 \text{ on } \partial\mathcal{B}, \end{aligned} \quad (6.17)$$

At first, the crack surface density function is defined isotropic as given in equation 6.10 whereas material anisotropy for cubic symmetry is defined with elastic material parameter, $\gamma(\theta)$ in the anisotropic part of the free energy which will be held later on.

6.3 Governing Equations of Anisotropic Fracture

6.3.1 Finite strain setting

Viscous rate-type potential, Π_η is given as

$$\Pi_\eta = \mathcal{E} + \mathcal{D}_\eta - \mathcal{P} \quad (6.18)$$

where \mathcal{E} represents the rate of energy storage functional, \mathcal{D}_η is viscous regularized dissipation functional and \mathcal{P} is the external power functional.

The rate of energy storage functional that includes work conjugate variables to ϕ and d are the first Piola-Kirchoff stress tensor, \mathbf{P} and the scalar energetic force f given as

follows

$$\mathcal{E}(\dot{\boldsymbol{\varphi}}; \dot{d}) = \int_{\mathcal{B}} (\mathbf{P} : \dot{\mathbf{F}} - f\dot{d}) dV, \quad (6.19)$$

where

$$\mathbf{P} = \partial_{\mathbf{F}} \Psi(\mathbf{g}, \mathbf{F}, \mathbf{A}_f; d), \quad f = -\partial_d \Psi(\mathbf{g}, \mathbf{F}, \mathbf{A}_f; d) \quad (6.20)$$

As given in equation 6.20, first Piola-Kirchoff stress tensor and scalar energetic force can be defined with respect to free energy function ψ . The free energy function provides the degrading free energy of the continuum with a quadratic degradation function $g(d) = (1 - d)^2$, i.e

$$\Psi(\mathbf{g}, \mathbf{F}, \mathbf{A}_f; d) := g(d) \Psi_0(\mathbf{g}, \mathbf{F}, \mathbf{A}_f) \quad (6.21)$$

In equation 6.21, the degradation of free energy of the intact material is defined with evolving the damage field according to growth conditions

$$g'(d) \leq 0 \quad \text{with} \quad g(0) = 1, g(1) = 0, g'(1) = 0 \quad (6.22)$$

Viscous regularized dissipation functional, \mathcal{D}_η , is given as

$$\mathcal{D}_\eta(\dot{d}, \beta; d) = \int_{\mathcal{B}} \left[\beta \dot{d} - \frac{1}{2\eta} \langle \chi(\beta; d, \nabla d) \rangle^2 \right] dV, \quad (6.23)$$

with the artificial viscosity $\eta \geq 0$ regulates the scalar viscous over-stress χ that reads

$$\chi(\beta; d, \nabla d) = \beta - g_c [\delta_d \gamma(d, \nabla d)] \quad (6.24)$$

The Macaulay brackets filter out the positive values, $\chi > 0$ and g_c represents the critical fracture energy. The external power acting on the body is given as follows

$$\mathcal{P}(\dot{\varphi}) = \int_{\mathcal{B}} \rho_0 \bar{\gamma} \cdot \dot{\varphi} dV + \int_{\partial \mathcal{B}_t} \bar{\mathbf{T}} \cdot \dot{\varphi} dA, \quad (6.25)$$

where, ρ_0 , $\bar{\gamma}$ and $\bar{\mathbf{T}}$ represent the material density, the prescribed body force and surface traction, respectively. Mixed variational principle of the evolution problem can be proposed with the rate-type potential Π_η as follows

$$\{\dot{\varphi}, \dot{d}, \beta\} = \text{Arg} \left\{ \inf_{\dot{\varphi} \in \mathcal{W}_{\dot{\varphi}}} \inf_{\dot{d} \in \mathcal{W}_{\dot{d}}} \sup_{\beta \geq 0} \Pi_\eta \right\} \quad (6.26)$$

with the admissible domains for the primary variables

$$\begin{aligned} \mathcal{W}_{\dot{\varphi}} &= \{\dot{\varphi} \mid \dot{\varphi} = \mathbf{0} \quad \text{on} \quad \partial \mathcal{B}_\varphi\} \\ \mathcal{W}_{\dot{d}} &= \{\dot{d} \mid \dot{d} = 0 \quad \text{on} \quad \partial \mathcal{B}_d\} \end{aligned} \quad (6.27)$$

Strong form of the field equations reduces to

$$\begin{aligned} 1: \quad \text{Div} \mathbf{P} + \rho_0 \bar{\gamma} &= \mathbf{0} \\ 2: \quad \eta \dot{d} &= 2(1-d) \bar{\mathcal{H}} - d + \text{Div}(\nabla d) \end{aligned} \quad (6.28)$$

Balance of linear momentum and evolution equation of crack phase field are represented by the first and second equation of 6.28, respectively. $\bar{\mathcal{H}}$ indicates the crack driving source such that

$$\bar{\mathcal{H}} = \frac{\Psi_0}{g_c/l} \quad (6.29)$$

6.3.2 Small strain setting

The displacement field $\mathbf{u} = \mathbf{x} - \mathbf{X}$ is described at a material point $\mathbf{X} \in \mathcal{B} \subset \mathbb{R}^3$ and at time $t \in \mathcal{T}$, i.e.,

$$\mathbf{u}(\mathbf{X}, t) : \begin{cases} \mathcal{B} \times \mathcal{T} & \rightarrow \mathbb{R}^3 \\ (\mathbf{X}, t) & \mapsto \mathbf{u}(\mathbf{X}, t) \end{cases} \quad (6.30)$$

In small strain setting, the rate of energy functional is given with the stress tensor $\boldsymbol{\sigma}$ which is the work conjugate variable of the small strain measure $\boldsymbol{\varepsilon} = \text{sym } \nabla \mathbf{u}$.

$$\mathcal{E}(\dot{\mathbf{u}}; \dot{d}) = \int_{\mathcal{B}} (\boldsymbol{\sigma} : \dot{\boldsymbol{\varepsilon}} - f \dot{d}) dV, \quad (6.31)$$

The energetic force, f stands in equation 6.30 as the work conjugate of the damage variable d . These two variables are expressed as

$$\sigma = \partial_{\boldsymbol{\varepsilon}} \Psi(\boldsymbol{\varepsilon}, \mathbf{A}; d), \quad f = -\partial_d \Psi(\boldsymbol{\varepsilon}, \mathbf{A}; d) \quad (6.32)$$

Free energy function of Ψ defines a degrading continuum with the effective free energy function of the intact solid, Ψ_0 as follows

$$\Psi(\boldsymbol{\varepsilon}, \mathbf{A}; d) := g(d) \Psi_0(\boldsymbol{\varepsilon}, \mathbf{A}) \quad (6.33)$$

The viscous regularized dissipation functional 6.23 and scalar viscous over stress function 6.24 remain unchanged for small strain setting as well. The external power term can be written as

$$\mathcal{P}(\dot{\mathbf{u}}) = \int_{\mathcal{B}} \rho_0 \bar{\boldsymbol{\gamma}} \cdot \dot{\mathbf{u}} dV + \int_{\partial \mathcal{B}_t} \bar{\mathbf{T}} \cdot \dot{\mathbf{u}} dA \quad (6.34)$$

where, ρ_0 , $\bar{\boldsymbol{\gamma}}$ and $\bar{\mathbf{T}}$ represent the material density, the prescribed body force and surface traction, respectively. A mixed variational principle of the evolution problem can be defined as follows

$$\{\dot{\mathbf{u}}, \dot{d}, \beta\} = \text{Arg} \left\{ \inf_{\dot{\mathbf{u}} \in \mathcal{W}_{\dot{\mathbf{u}}}} \inf_{\dot{d} \in \mathcal{W}_{\dot{d}}} \sup_{\beta \geq 0} \Pi_{\eta} \right\} \quad (6.35)$$

with the admissible domains for primary variables

$$\begin{aligned} \mathcal{W}_{\dot{\mathbf{u}}} &= \{\dot{\mathbf{u}} \mid \dot{\mathbf{u}} = \mathbf{0} \quad \text{on} \quad \partial \mathcal{B}_u\} \\ \mathcal{W}_{\dot{d}} &= \{\dot{d} \mid \dot{d} = 0 \quad \text{on} \quad \partial \mathcal{B}_d\} \end{aligned} \quad (6.36)$$

Then, the variation potential Π_η with respect to field $\{\dot{\mathbf{u}}, \dot{d}, \beta\}$ and algebraic manipulations [95] leads to strong form of the field equations

$$\begin{aligned} 1 : \quad \text{Div } \sigma + \rho_0 \bar{\gamma} &= \mathbf{0} \\ 2 : \quad \eta \dot{d} &= 2(1-d)\bar{\mathcal{H}} - d + \text{Div}(\nabla d) \end{aligned} \quad (6.37)$$

6.3.3 Constitutive model for cubic anisotropy

Free energy function of a cubic anisotropic solid can be decomposed into two parts, i.e, isotropic and anisotropic parts. Isotropic solids can be defined with three invariant, I_1, I_2, I_3 that are given in equation 6.4 in terms of left Cauch-Green deformation tensor. For unidirectional anisotropy, the stored energy can be obtained in terms of first three invariants with the addition of fourth invariant I_4 . For cubic anisotropy, the unidirectional anisotropy can be extended to three orthogonal directions. The extended fourth invariant, I_{4i} can be stated as

$$I_{4i} = \mathbf{f}_i \cdot \mathbf{g} \mathbf{f}_i \text{ for } i = 1, 2, 3 \quad (6.38)$$

where \mathbf{f}_i represents the three orthogonal anisotropy directions of cubic symmetry.

The mechanical part of the free energy function for a single crystal with cubic symmetry is described as

$$\Psi_0(g, \mathbf{F}, \mathbf{M}_i) := \Psi_0^{\text{iso}}(J, I_1) + \Psi_0^{\text{ani}}(I_{4i}) \quad (6.39)$$

where $\mathbf{M}_i = \mathbf{f}_i \otimes \mathbf{f}_i$ with $i = \{1, 2, 3\}$ are the structural tensors associated with the three orthogonal unit normal vectors \mathbf{f}_i corresponding to the cubic anisotropy. Herein, we have decomposed the free energy function into isotropic and additional stiffness terms in cube orientations due to cubic symmetry. The isotropic part of the free energy function reads

$$\Psi_0^{\text{iso}}(J, I_1) := \frac{\lambda(\theta)}{2} (\ln J)^2 + \frac{\mu(\theta)}{2} (I_1 - 2 \ln J - 3) \quad (6.40)$$

where $\lambda(\theta)$ and $\mu(\theta)$ are the temperature-dependent Lamé parameters. For the anisotropic part one can use

$$\Psi_0^{\text{ani}}(I_{4i}) := \sum_{i=1}^3 \frac{\gamma(\theta)}{4} (I_{4i} - 1)^2 \quad (6.41)$$

with $\gamma(\theta)$ as the additional modulus term due to cubic crystal structure. The fourth invariant, I_{4i} has three components, i.e, $i = 1, 2, 3$ corresponding to three orthogonal vectors of cubic symmetry. The Kirchoff stress tensor τ , can also be introduced as such

$$\tau := \mathbf{P}\mathbf{F}^T = 2\partial_g\Psi = g(d)\tau_0, \quad \tau_0 = 2\partial_g\Psi_0 \quad (6.42)$$

with a monotonic degradation function, $g(d)$. The given definitions in 6.39, 6.40 and 6.41 are used to obtain Kirchoff stress given in 6.42 so that

$$\tau_0 = \lambda \ln J \mathbf{g}^{-1} + \mu (\mathbf{b} - \mathbf{g}^{-1}) + \sum_{i=1}^3 \gamma(\theta) (I_{4i} - 1) \mathbf{f}_i \otimes \mathbf{f}_i \quad (6.43)$$

Please note that

$$\partial_g J = \frac{1}{2} J \mathbf{g}^{-1}, \quad \partial_g I_1 = \mathbf{b}, \quad \partial_g I_{4i} = \mathbf{f}_i \otimes \mathbf{f}_i \quad (6.44)$$

Elasticity tensor and effective elasticity tensors are defined as

$$\mathbb{C} := 4\partial_{gg}^2\Psi = g(d)\mathbb{C}_0, \quad \mathbb{C}_0 = 4\partial_{gg}^2\Psi_0, \quad (6.45)$$

with explicit definition expression for \mathbb{C}_0

$$\mathbb{C}_0 = \lambda \mathbf{g}^{-1} \otimes \mathbf{g}^{-1} + 2(\mu - \lambda \ln J) \mathbb{I}_{g^{-1}} + \sum_{i=1}^3 2\gamma(\theta) \mathbb{M}_i \quad (6.46)$$

where the symmetric fourth order identity tensor $\mathbb{I}_{g^{-1}}$ can be represented in indicial notation $(\mathbb{I}_{g^{-1}})^{ijkl} = (\delta^{ik}\delta^{jl} + \delta^{il}\delta^{jk})/2$ and the fourth order structure tensors

$$\mathbb{M}_i := \mathbf{M}_i \otimes \mathbf{M}_i \quad (6.47)$$

6.3.4 Linearization of the constitutive model

The linearized form of the free energy function is represented as follows

$$\Psi(\boldsymbol{\varepsilon}, \mathbf{M}_i, \theta) = \Psi_{\text{iso}}(\boldsymbol{\varepsilon}, \theta) + \Psi_{\text{ani}}(\boldsymbol{\varepsilon}, \mathbf{M}_i, \theta) \quad (6.48)$$

Isotropic and anisotropic parts of the free energy take the forms

$$\Psi_{\text{iso}}(\boldsymbol{\varepsilon}, \theta) = \frac{\lambda(\theta)}{2} (\text{tr } \boldsymbol{\varepsilon})^2 + \mu(\theta) \boldsymbol{\varepsilon} : \boldsymbol{\varepsilon} \quad (6.49)$$

The additional term of the free energy function due to cubic symmetry reads

$$\Psi_{\text{ani}}(\boldsymbol{\varepsilon}, \mathbf{M}_i, \theta) = \sum_{i=1}^3 \frac{\gamma(\theta)}{4} (\boldsymbol{\varepsilon} : \mathbf{M}_i)^2 \quad (6.50)$$

with $\gamma(\theta)$ as the additional modulus term due to cubic crystal structure. The stress expression then has the following form

$$\boldsymbol{\sigma} = \lambda(\theta) \text{tr } \boldsymbol{\varepsilon} \mathbf{1} + 2\mu(\theta) \boldsymbol{\varepsilon} + \sum_{i=1}^3 \frac{\gamma(\theta)}{2} (\boldsymbol{\varepsilon} : \mathbf{M}_i) \mathbf{M}_i. \quad (6.51)$$

The fourth order elasticity tensor can be derived from the stress tensor as follows

$$\mathbb{C} = \lambda(\theta) \mathbf{1} \otimes \mathbf{1} + 2\mu(\theta) \mathbb{I} + \sum_{i=1}^3 \frac{\gamma(\theta)}{2} \mathbb{M}_i, \quad (6.52)$$

where \mathbb{I} is the fourth-order identity tensor $\mathbb{I}_{ijkl} = \delta_{ik}\delta_{jl} + \delta_{il}\delta_{jk}$ and $\mathbb{M}_i = \mathbf{M}_i \otimes \mathbf{M}_i$ is the structural tensor associated with the cube faces. The elasticity tensor of a cubic symmetric crystal in matrix notation with the Voigt convention reads

$$\hat{\mathbb{C}} = \begin{bmatrix} C_{11} & C_{12} & C_{12} & & & \\ C_{12} & C_{11} & C_{11} & & & \\ C_{12} & C_{12} & C_{11} & & & \\ & & & C_{44} & & \\ & & & & C_{44} & \\ & & & & & C_{44} \end{bmatrix}. \quad (6.53)$$

By comparing (6.52) and (6.53), we conclude that

$$\gamma = C_{11} - 2C_{44} - C_{12} \quad \mu = C_{44} \quad \lambda = C_{12}. \quad (6.54)$$

Herein, μ and λ are the shear modulus and the first Lamé constant, respectively

The parameter γ vanishes for isotropic elastic materials leading to $2C_{44} = C_{11} - C_{12}$. Chadwick *et al.* [211] provide additional insight into the acceptable range of symmetries for the elasticity tensor and the consequent count of autonomous elastic constants.

6.3.5 Energy based anisotropic failure criterion

As given in equation 6.39, free energy functions are decomposed into two parts. So, critical fracture energies can also be decomposed into isotropic and anisotropic parts which are represented by g_c^{iso} and g_c^{ani} , respectively. These critical fracture energies can be defined with a proportionality constant, α such that

$$g_c^{\text{iso}} = \alpha g_c^{\text{ani}}$$

As a result, crack driving source term in equation 6.29 can be defined as

$$\overline{\mathcal{H}}^{\text{iso}} = \frac{\Psi_0^{\text{iso}}}{g_c^{\text{iso}}/l}, \quad \overline{\mathcal{H}}^{\text{ani}} = \frac{\Psi_0^{\text{ani}}}{g_c^{\text{ani}}/l} \quad (6.55)$$

that leads to rate-independent evolution of the phase field

$$(1 - d)\mathcal{H} = d - \frac{1}{2} \text{Div}(\nabla d) \quad (6.56)$$

along with the specific form of the dimensionless crack driving source term

$$\begin{aligned} \mathcal{H}(t) &= \max_{s \in [0, t]} [\langle \overline{\mathcal{H}}(s) - 1 \rangle] \\ \overline{\mathcal{H}} &= \overline{\mathcal{H}}^{\text{iso}} + \overline{\mathcal{H}}^{\text{ani}} \end{aligned} \quad (6.57)$$

In equation 6.57, an irreversible and positive crack driving source is defined where the Macaulay brackets filter out the positive values for $\mathcal{H}(s) - 1$ that indicates the material will be intact until the failure surface is reached.

$$\underbrace{\eta \dot{d}}_{\text{Crack evolution}} = \underbrace{(1-d)\mathcal{H}}_{\text{Driving force}} - \underbrace{\left[d - \frac{1}{2} \text{Div}(\nabla d) \right]}_{\text{Geometric resistance}}, \quad (6.58)$$

The rate dependent case can be defined with the crack driving force and geometric resistance terms. For the rate independent case, there must be balance between the crack driving force and the geometric resistance. In the upcoming case studies, isotropic geometric resistance for crack propagation is used. However, the material free energy is defined for cubic anisotropy.

6.4 Representative numerical examples

6.4.1 Effect of length scale parameter

Length scale parameter which determines bread of the crack represented by l . The effect of this parameter is investigated on a square plate with planar dimensions of $10 \times 10mm^2$ with a thickness of $1mm$ that contains a notch starting on left edge and propagating to the center of the body is defined as given in Figure 6.3. The top edge of the plate at $y = 10$ is exposed to linear displacement, u , whereas it is fixed in three directions at $y = 0$. The material is defined as cubic anisotropic with the structural directors f_1 , f_2 and f_3 . The structural director of f_1 is inclined (θ) with respect to x-axis of a fixed cartesian coordinate system.

As a cubic symmetric material, a III-V group semiconductor compound, GaSb material is defined for the analysis. Previously determined temperature dependent thermo-elastic material properties of GaSb by using DFT are used in this study. Second order elastic constants as well as Lamé parameters of GaSb are defined with the following polynomial in equation 5.13.

To determine the effect of length scale parameter, element size of $0.25mm$, h_e , is used

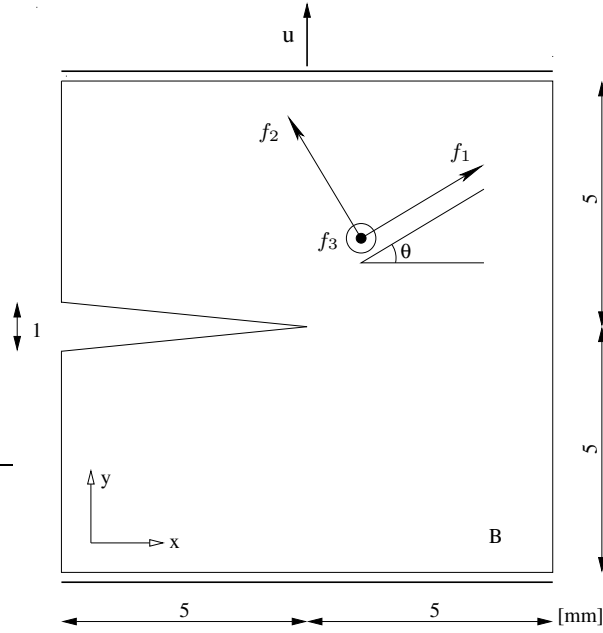


Figure 6.3: Square plate with a single notch has 1mm thickness with the applied boundary conditions

in analysis. When the length scale parameter effect is investigated, a horizontal material orientation ($\theta = 0$) is used with the material parameters of GaSb at $\theta = 298\text{K}$. Length scale parameters of $l = 0.3, 0.6, 1.2, 2.4\text{mm}$'s are applied on the geometry defined in Figure 6.3. As observed in crack evolution equation 6.58, geometric crack resistance is isotropic. However, the crack driving force is anisotropic due to defined free energy function is composed of isotropic and anisotropic parts. The changing length scale parameter is not defined with different crack orientations in this study. According to obtained results, an obvious smearing difference is observed when the length scale parameter is increased. When the length scale parameter is increased, effected material zone by an initiated crack increases as observed from Figure 6.4. Using too large length scale parameter may result in crack merging, branching more easily in case of having multiple cracks in the specified geometry.

6.4.2 Uniaxial tension of a notched plate

For a representative case study, the geometry given in Figure 6.3 is used with different material orientation angles, θ . Material parameters of GaSb are defined according to

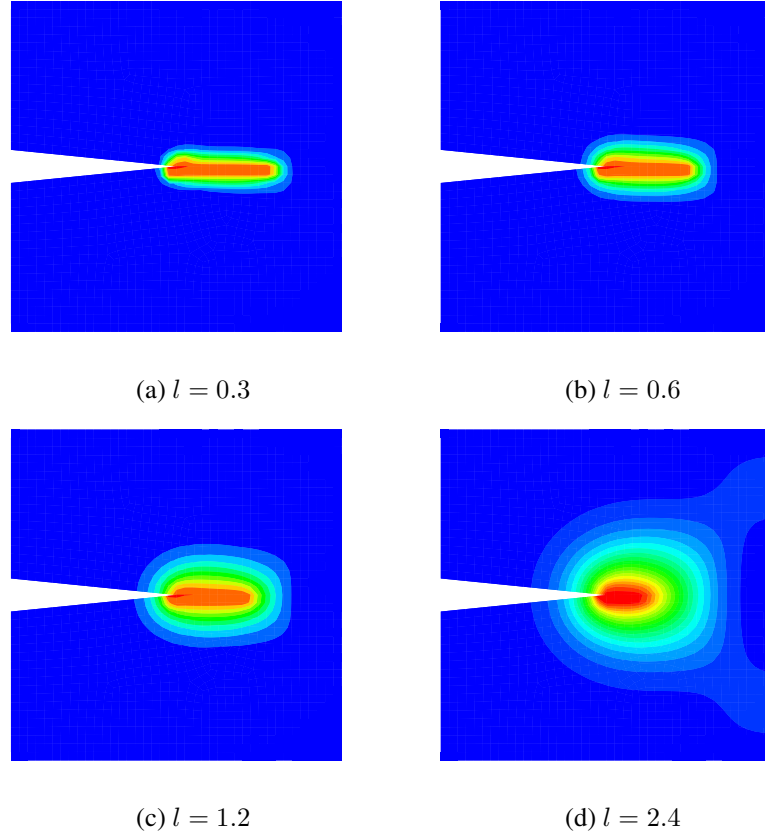


Figure 6.4: Effect of length scale parameter on crack (a) $l = 0.3$, (b) $l = 0.6$, (c) $l = 1.2$, (d) $l = 2.4$

given polynomial in 5.13 and Table 5.4. The critical isotropic free energy, g_c^{iso} is defined as $1E - 03$ [MPa mm] with critical fracture energy proportionality constant of $\alpha = 5E - 05$. Note that if $\alpha = 1$, then isotropic free energy and anisotropic free energy of fracture will be equal. A finite element discretization is done with 1534 elements on the whole domain. A constant element size of 0.25mm is used and the length scale parameter $l = 0.6$, is chosen such that it is greater than 2 times of the element size.

Load–displacement behavior of the notched plate given in Figure 6.3 is investigated for different material orientations θ . Provided results in Figure 6.5 shows that when θ increases from 0° to 45° , the damage in the material observed earlier with the given input configuration. However, the maximum load that can be applied before the material degradation increases when θ increases. Specifically, $\theta = 15^\circ$, 30° and 45° orientations can withstand 30.71%, 78.92% and 104.26% higher maximum loads with

respect to 0° orientation, respectively. If the critical free energy threshold, g_c is increased, the absolute values of maximum loads before the material degradation is expected to be higher.

Crack propagation paths are analyzed for different material orientations and the results are given in Figure 6.6. The dashed lines given in Figure 6.6 represents f_1 vector which makes the angle θ with the horizontal axis whereas the solid lines represents the vector, f_2 . For 0° , 45° and 90° , a horizontal crack propagation is observed on the notched geometry. When the material orientation has an angle with the horizontal x-axis, the crack is propagating on horizontal direction for a while, then its direction is changed depending on the given in-plane material orientation. If the material orientation angle is smaller than $\theta < 45^\circ$, developed crack follows the dashed line or f_1 direction. When $\theta > 45^\circ$, the crack eventually follows the second direction $-f_2$ or the solid line. For $\theta = 60^\circ$ and $\theta = 75^\circ$, the crack is following $-f_2$ direction which is symmetric with respect to the dashed line in Figure 6.6 c) and b), respectively. In this model, the critical free energy, g_c is defined as a scalar field because it is given isotropic. However, another alternative could be defining orientation dependent critical free energy to model anisotropic fracture, $g_c(\theta)$.

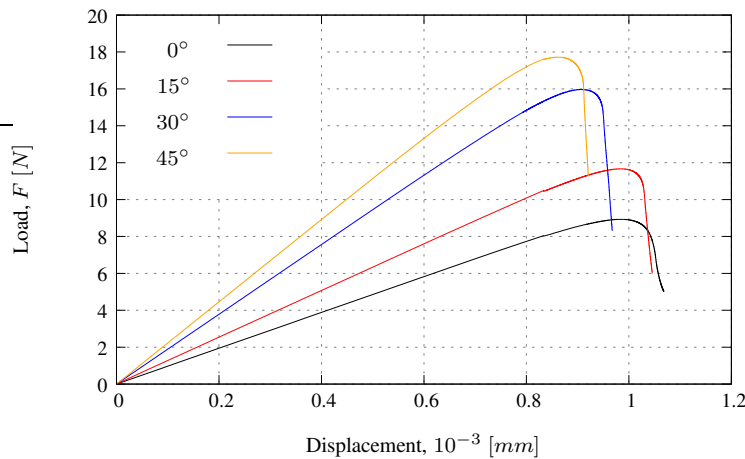


Figure 6.5: Force displacement results of different in plane material orientations

A phase field model is provided for cubic anisotropy and the effect of the length scale parameter is covered for 0° material orientation. Then, the effect of material orientation on crack propagation path is investigated. Force-displacement results of the case study for different material orientations are also analyzed.

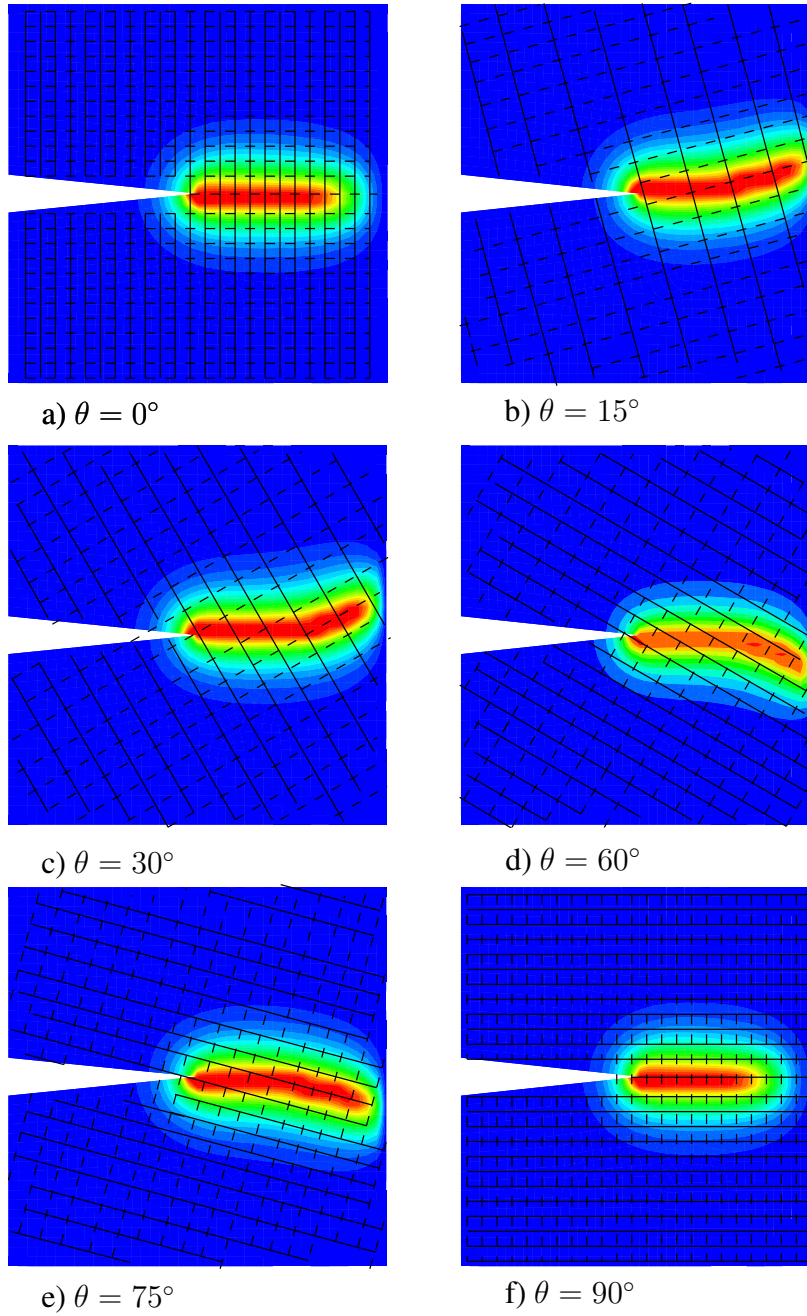


Figure 6.6: Effect of material orientation on crack propagation

CHAPTER 7

CONCLUDING REMARKS

This thesis represents the first attempt to obtain temperature dependent thermo-elastic material properties of III-V and II-VI semiconductor materials with quasi-harmonic approximation in Density Functional Theory. The investigated materials are widely used in broad range of applications for which these materials can be exposed to different temperatures due to operation/storage conditions, microfabrication and growth processes. Experimental studies for different semiconductor materials show good coherence with obtained results by DFT. Thermal expansion coefficient results obtained by LDA show excellent coherence for all binary compounds. PBEsol provides similar trends in comparison to LDA but with slight differences. Second-order elastic constant results provide very similar behavior for both LDA and PBEsol approximations for all of the investigated semiconductors. Experimental results of second order elastic constants can be represented within 10% by investigated DFT studies. Lattice constant, Poisson ratio, heat capacity and Vicker's hardness of different semiconductor materials from III-V and II-VI groups are established within quasi harmonic approximation on a wide temperature limits. Effect of supercell size and strain level on second order elastic constants is investigated on different materials. It is shown that supercell size of $2 \times 2 \times 2$ provides better efficiency in terms of computational power and time requirement without reducing accuracy. Strain dependency analysis on binary compounds of II-VI semiconductors provided that strain level of 0.1% shows excellent results in second order elastic constant determinations of CdTe whereas the results are insensitive for HgTe and ZnTe materials with both LDA and PBEsol approximations. Opto-electronic material properties of $\text{Cd}_{0.96}\text{Zn}_{0.04}\text{Te}$, i.e, refractive index, energy band-gap and extinction constant, are determined in a temperature interval of 1-300K. Moreover, second order elastic constants, Poisson ratio,

Vicker's hardness and heat capacity of CdZnTe are also obtained with PBEsol.

A benchmark study that shows the effect of using temperature dependent material properties on thermo-mechanical stress estimations resulted an improvement of determined von Mises stress level on GaSb with 28.4% for GaSb-SS304 rectangular prism shaped bimaterial assembly. In IRFPA structure, there is more complex geometry and the number of constituent materials is higher. A representative IRFPA assembly structure is defined that consists of five different parts and cryocooling of the assembly from room temperature to 77K is analyzed. Coefficient of thermal expansion mismatch driven problem developed thermo-mechanical stresses on sensing IRFPA layer that was GaSb in this case. An improvement of 44.7% on maximum von Mises stress of IRFPA (GaSb) layer is observed that is clearly higher than the analyzed bimaterial assembly. The free energy expression is proposed such that cubic anisotropy is covered. Temperature-dependent Lamé parameters, $\lambda(\theta)$ and $\mu(\theta)$ together with cubic symmetry parameter, $\gamma(\theta)$ are determined in terms of second order elastic constants. For the given temperature limits, curve fitting is applied for GaSb and InSb materials to fit Lamé parameters and cubic symmetry parameter, $\gamma(\theta)$ with a polynomial function. Thermal field is added in the free energy definition such that coupled-field problems can use this free energy expressions in the future.

Experimental study to determine elastic modulus and Vicker's hardness of GaSb is conducted by using nanoindentation method. It is observed that surface condition of the material shows great importance while determining elastic modulus of GaSb. Experimental results of elastic modulus and Vickers's hardness are compared with room temperature DFT result and good coherence is observed. Vicker's hardness results show more deviations with respect to elastic modulus experimental result. Main reason of this difference between elastic modulus and Vicker's hardness can be caused by the contact area determinations. The theoretical or calibrated contact area is used to determine elastic modulus whereas the developed contact area is used to calculate Vicker's hardness. Theoretically calculated developed contact area may cause great oscillations in the obtained nanoindentation results especially for non-polished GaSb surface. A test setup that consists of vacuum envelope, rotary Stirling cryocooler, turbomolecular and dry pump with proper interfaces is designed. This custom designed

test setup is used to cooldown of GaSb and CdZnTe semiconductor compounds to 77K. Before the cryocooling experiments, these semiconductors are integrated with stainless steel by using epoxy material. Due to developed thermo-mechanical stress, crack initiation and propagation is observed on both of the samples. Induced cracks on both of the materials are observed with scanning electron microscopy at room temperature. With these experiments, both unidirectional and zig-zag patterned cracks are reported with different crack propagation angles.

A preliminary study of crack initiation and propagation on cubic crystals is performed with Phase Field Theory. The developed free energy function for cubic symmetry is used in this theory. Obtained material parameters of GaSb by DFT are used as material inputs of phase field fracture simulations. A notched geometry is investigated under uniaxial tension with a fixed end as given in Figure 6.3. It is observed that the crack propagation paths differ with respect to changing in plane material orientation.

The proposed framework from DFT simulations to experimental verification of material parameters and crack initiation/propagation investigations with the defined test setup and phase field simulations can be applied to different semiconductors. Elastic modulus and Vicker's hardness verifications on GaSb can be performed at different temperatures with a more sophisticated instrument by nanoindentation. Stress-strain behavior of semiconductors for elasto-plastic region can be determined with molecular dynamics simulations or with DFT by using relatively large amount of computational power and time. To observe plastic behavior of a single crystal material, it will be required to define more than ten times of the unit cell structure which may not be feasible by DFT. So, molecular dynamics simulations can be a better alternative to work on plastic and fracture characteristic of single crystals.

As a future implementation of the provided test setup, the test setup design can be improved for application or testing of a material for specific purpose under thermo-mechanical loading by cryocooling and coefficient of thermal expansion mismatch. Moreover, thermal cycling can be applied between room temperature and cryogenic temperatures on a desired assembly. So thermo-mechanical fatigue lifetime experi-

ments can be performed. With proper modifications, this test setup can be used not only for mechanical characterization of materials but also for opto-electronic tests of IRFPA structures.

For another future work alternative, phase field fracture model can be improved by providing the thermal field together with mechanical and crack phase field so that coupled thermo-mechanical fracture can be simulated. Crack initiation and propagation due to cryocooling and coefficient of thermal expansion mismatch of constituent materials can be simulated. Higher order phase field methods can be developed for specifically proposed materials such that one of the experimental outcomes of this thesis can be compared with another numerical result as well.

REFERENCES

- [1] A. Manickavasagan and H. Jayasuriya, *Imaging with electromagnetic spectrum: applications in food and agriculture*. Springer, 2014.
- [2] G. Mosby Jr, B. J. Rauscher, C. Bennett, E. S. Cheng, S. Cheung, A. Cillis, D. Content, D. Cottingham, R. Foltz, J. Gygax, *et al.*, “Properties and characteristics of the nancy grace roman space telescope h4rg-10 detectors,” *Journal of Astronomical Telescopes, Instruments, and Systems*, vol. 6, no. 4, pp. 046001–046001, 2020.
- [3] M. Lee, M. Yoo, J. Cho, S. Lee, J. Kim, C. Lee, D. Kang, C. Zwenger, and R. Lanzone, “Study of interconnection process for fine pitch flip chip,” in *2009 59th Electronic Components and Technology Conference*, pp. 720–723, IEEE, 2009.
- [4] J. H. Lau, “Recent advances and new trends in flip chip technology,” *Journal of Electronic Packaging*, vol. 138, no. 3, p. 030802, 2016.
- [5] Z. Zhang and C. Wong, “Recent advances in flip-chip underfill: materials, process, and reliability,” *IEEE transactions on advanced packaging*, vol. 27, no. 3, pp. 515–524, 2004.
- [6] P. Palaniappan, D. F. Baldwin, P. J. Selman, J. Wu, and C. Wong, “Correlation of flip chip underfill process parameters and material properties with in-process stress generation,” *IEEE Transactions on Electronics Packaging Manufacturing*, vol. 22, no. 1, pp. 53–62, 1999.
- [7] E. Brinksmeier, J. Aurich, E. Govekar, C. Heinzl, H.-W. Hoffmeister, F. Klocke, J. Peters, R. Rentsch, D. Stephenson, E. Uhlmann, *et al.*, “Advances in modeling and simulation of grinding processes,” *CIRP annals*, vol. 55, no. 2, pp. 667–696, 2006.
- [8] X. Chen and W. B. Rowe, “Analysis and simulation of the grinding process.

- part ii: Mechanics of grinding,” *International Journal of Machine Tools and Manufacture*, vol. 36, no. 8, pp. 883–896, 1996.
- [9] Z. Huang, N. Geyer, P. Werner, J. De Boor, and U. Gösele, “Metal-assisted chemical etching of silicon: a review: in memory of prof. ulrich gösele,” *Advanced materials*, vol. 23, no. 2, pp. 285–308, 2011.
- [10] P. A. Olsson, “First principles investigation of the finite temperature dependence of the elastic constants of zirconium, magnesium and gold,” *Computational Materials Science*, vol. 99, pp. 361–372, 2015.
- [11] T. Shao, B. Wen, R. Melnik, S. Yao, Y. Kawazoe, and Y. Tian, “Temperature dependent elastic constants and ultimate strength of graphene and graphyne,” *The Journal of chemical physics*, vol. 137, no. 19, p. 194901, 2012.
- [12] C. Malica and A. Dal Corso, “Quasi-harmonic temperature dependent elastic constants: applications to silicon, aluminum, and silver,” *Journal of Physics: Condensed Matter*, vol. 32, no. 31, p. 315902, 2020.
- [13] M. Khanzadeh and G. Alahyarizadeh, “A dft study on pressure dependency of tic and zrc properties: Interconnecting elastic constants, thermodynamic, and mechanical properties,” *Ceramics International*, vol. 47, no. 7, pp. 9990–10005, 2021.
- [14] R. Wang, S. Wang, X. Wu, and Y. Yao, “First-principles calculations on temperature-dependent elastic constants of rare-earth intermetallic compounds: Yag and ycu,” *Physica B: Condensed Matter*, vol. 406, no. 20, pp. 3951–3955, 2011.
- [15] P. Ravindran, L. Fast, P. A. Korzhavyi, B. Johansson, J. Wills, and O. Eriksson, “Density functional theory for calculation of elastic properties of orthorhombic crystals: Application to tisi 2,” *Journal of Applied Physics*, vol. 84, no. 9, pp. 4891–4904, 1998.
- [16] H. H. Pham, M. E. Williams, P. Mahaffey, M. Radovic, R. Arroyave, and T. Cagin, “Finite-temperature elasticity of fcc Al: Atomistic simulations and ultrasonic measurements,” *Physical Review B*, vol. 84, no. 6, p. 064101, 2011.

- [17] U. Argaman and G. Makov, “First-principles study of the temperature dependence of the elastic constants of hcp titanium,” *Computational Materials Science*, vol. 184, p. 109917, 2020.
- [18] M. Łopuszyński and J. A. Majewski, “Ab initio calculations of third-order elastic constants and related properties for selected semiconductors,” *Physical Review B*, vol. 76, no. 4, p. 045202, 2007.
- [19] I. V. Lebedeva, A. S. Minkin, A. M. Popov, and A. A. Knizhnik, “Elastic constants of graphene: Comparison of empirical potentials and dft calculations,” *Physica E: Low-dimensional Systems and Nanostructures*, vol. 108, pp. 326–338, 2019.
- [20] M. Behet, B. Stoll, W. Brysch, and K. Heime, “Growth of GaSb and InSb by low-pressure plasma MOVPE,” *Journal of Crystal Growth*, vol. 124, no. 1-4, pp. 377–382, 1992.
- [21] N. Udayashankar and H. Bhat, “Growth and characterization of indium antimonide and gallium antimonide crystals,” *Bulletin of Materials Science*, vol. 24, no. 5, pp. 445–453, 2001.
- [22] A. Rogalski, *Infrared detectors*. CRC press, 2000.
- [23] J. Wheeler, D. Armstrong, W. Heinz, and R. Schwaiger, “High temperature nanoindentation: The state of the art and future challenges,” *Current Opinion in Solid State and Materials Science*, vol. 19, no. 6, pp. 354–366, 2015.
- [24] W. Kang and M. T. A. Saif, “In situ study of size and temperature dependent brittle-to-ductile transition in single crystal silicon,” *Advanced Functional Materials*, vol. 23, no. 6, pp. 713–719, 2013.
- [25] R. Golezorkhtabar, P. Pavone, J. Spitaler, P. Puschnig, and C. Draxl, “Elastic: A tool for calculating second-order elastic constants from first principles,” *Computer Physics Communications*, vol. 184, no. 8, pp. 1861–1873, 2013.
- [26] H. Wang and M. Li, “Ab initio calculations of second-, third-, and fourth-order elastic constants for single crystals,” *Physical Review B*, vol. 79, no. 22, p. 224102, 2009.

- [27] J. Zhao, J. Winey, and Y. Gupta, “First-principles calculations of second- and third-order elastic constants for single crystals of arbitrary symmetry,” *Physical Review B*, vol. 75, no. 9, p. 094105, 2007.
- [28] J. R. Ray, M. C. Moody, and A. Rahman, “Molecular dynamics calculation of elastic constants for a crystalline system in equilibrium,” *Physical Review B*, vol. 32, no. 2, p. 733, 1985.
- [29] D. Squire, A. Holt, and W. Hoover, “Isothermal elastic constants for argon. theory and Monte Carlo calculations,” *Physica*, vol. 42, no. 3, pp. 388–397, 1969.
- [30] D. E. Hooks, K. J. Ramos, C. A. Bolme, and M. J. Cawkwell, “Elasticity of crystalline molecular explosives,” *Propellants, Explosives, Pyrotechnics*, vol. 40, no. 3, pp. 333–350, 2015.
- [31] H. Yao, L. Ouyang, and W.-Y. Ching, “Ab initio calculation of elastic constants of ceramic crystals,” *Journal of the American Ceramic Society*, vol. 90, no. 10, pp. 3194–3204, 2007.
- [32] A. Montazeri and H. Rafii-Tabar, “Multiscale modeling of graphene- and nanotube-based reinforced polymer nanocomposites,” *Physics Letters A*, vol. 375, no. 45, pp. 4034–4040, 2011.
- [33] J. Johnson, L. Samoska, A. Gossard, J. Merz, M. Jack, G. Chapman, B. Baumgratz, K. Kosai, and S. Johnson, “Electrical and optical properties of infrared photodiodes using the InAs/Ga_{1-x}In_xSb superlattice in heterojunctions with GaSb,” *Journal of Applied Physics*, vol. 80, no. 2, pp. 1116–1127, 1996.
- [34] M. Kitchin, M. Shaw, E. Corbin, J. Hagon, and M. Jaros, “Optical properties of imperfect strained-layer InAs/Ga_{1-x}In_xSb/AlSb superlattices with infrared applications,” *Physical Review B*, vol. 61, no. 12, p. 8375, 2000.
- [35] N. Bouarissa, S. Siddiqui, and M. Boucenna, “Lattice vibration and polaron properties of InSb under pressure,” *Crystal Research and Technology*, vol. 52, no. 7, p. 1700018, 2017.

- [36] M. P. Lumb, S. Mack, K. J. Schmieder, M. González, M. F. Bennett, D. Scheiman, M. Meitl, B. Fisher, S. Burroughs, K.-T. Lee, *et al.*, “GaSb-based solar cells for full solar spectrum energy harvesting,” *Advanced energy materials*, vol. 7, no. 20, p. 1700345, 2017.
- [37] Y. Shoji, R. Tamaki, and Y. Okada, “Multi-stacked GaSb/GaAs Type-II quantum nanostructures for application to intermediate band solar cells,” *AIP Advances*, vol. 7, no. 6, p. 065305, 2017.
- [38] R. Gu, J. Antoszewski, W. Lei, I. Madni, G. Umana-Membrenao, and L. Faraone, “MBE growth of HgCdTe on GaSb substrates for application in next generation infrared detectors,” *Journal of Crystal Growth*, vol. 468, pp. 216–219, 2017.
- [39] A. M. Hoang, A. Dehzangi, S. Adhikary, and M. Razeghi, “High performance bias-selectable three-color Short-wave/Mid-wave/Long-wave Infrared Photodetectors based on Type-II InAs/GaSb/AlSb superlattices,” *Scientific reports*, vol. 6, no. 1, pp. 1–7, 2016.
- [40] J. Sun, M. Peng, Y. Zhang, L. Zhang, R. Peng, C. Miao, D. Liu, M. Han, R. Feng, Y. Ma, *et al.*, “Ultra-high hole mobility of Sn-catalyzed GaSb nanowires for high speed infrared photodetectors,” *Nano Letters*, vol. 19, no. 9, pp. 5920–5929, 2019.
- [41] Y. Al-Douri, H. Abid, and H. Aourag, “Correlation between the bulk modulus and the transition pressure in semiconductors,” *Materials letters*, vol. 59, no. 16, pp. 2032–2034, 2005.
- [42] H. Salehi, H. A. Badehian, and M. Farbod, “First principle study of the physical properties of semiconducting binary antimonide compounds under hydrostatic pressures,” *Materials science in semiconductor processing*, vol. 26, pp. 477–490, 2014.
- [43] T. A. Nilsen, M. Breivik, G. Myrvågnes, and B.-O. Fimland, “Thermal expansion of GaSb measured by temperature dependent x-ray diffraction,” *Journal of Vacuum Science & Technology B, Nanotechnology and Microelectronics: Ma-*

- terials, Processing, Measurement, and Phenomena*, vol. 28, no. 3, pp. C3I17–C3I20, 2010.
- [44] D. Varshney, G. Joshi, M. Varshney, and S. Shriya, “Pressure induced structural phase transition and elastic properties in BSb, AlSb, GaSb and InSb compounds,” *Physica B: Condensed Matter*, vol. 405, no. 7, pp. 1663–1676, 2010.
- [45] E. Pease, L. Dawson, L. Vaughn, P. Rotella, and L. Lester, “2.5–3.5 μm optically pumped GaInSb/AlGaInSb multiple quantum well lasers grown on AlInSb metamorphic buffer layers,” *Journal of applied physics*, vol. 93, no. 6, pp. 3177–3181, 2003.
- [46] G. Nash, S. Smith, S. Coomber, S. Przeslak, A. Andreev, P. Carrington, M. Yin, A. Krier, L. Buckle, M. Emeny, *et al.*, “Midinfrared GaInSb/AlGaInsb quantum well laser diodes grown on GaAs,” *Applied Physics Letters*, vol. 91, no. 13, p. 131118, 2007.
- [47] A. Rogalski, “Infrared detectors: status and trends,” *Progress in quantum electronics*, vol. 27, no. 2-3, pp. 59–210, 2003.
- [48] S. Ozer and C. Besikci, “Assessment of InSb photodetectors on Si substrates,” *Journal of Physics D: Applied Physics*, vol. 36, no. 5, p. 559, 2003.
- [49] Q. Meng, X. Zhang, Y. Lü, and J. Si, “Calculation and verification of thermal stress in InSb focal plane arrays detector,” *Optical and Quantum Electronics*, vol. 49, no. 12, p. 402, 2017.
- [50] X. Zhang, Q. Meng, L. Zhang, and Y. Lv, “Modeling and deformation analyzing of InSb focal plane arrays detector under thermal shock,” *Infrared Physics & Technology*, vol. 63, pp. 28–34, 2014.
- [51] M. Breivik, T. A. Nilsen, and B.-O. Fimland, “Temperature dependent lattice constant of InSb above room temperature,” *Journal of crystal growth*, vol. 381, pp. 165–168, 2013.
- [52] X. Cai and J. Wei, “Temperature dependence of the thermal properties of InSb materials used in data storage,” *Journal of Applied Physics*, vol. 114, no. 8, p. 083507, 2013.

- [53] S. Kasap and A. Willoughby, *Mercury Cadmium Telluride: Growth, Properties and Applications*. John Wiley & Sons, 2011.
- [54] D. J. Hall, L. Buckle, N. T. Gordon, J. Giess, J. E. Hails, J. W. Cairns, R. M. Lawrence, A. Graham, R. S. Hall, C. Maltby, *et al.*, “Long-wavelength infrared focal plane arrays fabricated from hgcdte grown on silicon substrates,” in *Infrared Technology and Applications XXX*, vol. 5406, pp. 317–322, International Society for Optics and Photonics, 2004.
- [55] L. He, X. Fu, Q. Wei, W. Wang, L. Chen, Y. Wu, X. Hu, J. Yang, Q. Zhang, R. Ding, *et al.*, “Mbe hgcdte on alternative substrates for fpa applications,” *Journal of electronic materials*, vol. 37, no. 9, pp. 1189–1199, 2008.
- [56] A. Rohatgi, R. Sudharsanan, S. Ringel, and M. MacDougal, “Growth and process optimization of cdte and cdznte polycrystalline films for high efficiency solar cells,” *Solar Cells*, vol. 30, no. 1-4, pp. 109–122, 1991.
- [57] S. Chander, A. De, and M. Dhaka, “Towards cdznte solar cells: An evolution to post-treatment annealing atmosphere,” *Solar Energy*, vol. 174, pp. 757–761, 2018.
- [58] C. Szeles, “Cdznte and cdte materials for x-ray and gamma ray radiation detector applications,” *physica status solidi (b)*, vol. 241, no. 3, pp. 783–790, 2004.
- [59] Y. Eisen and A. Shor, “Cdte and cdznte materials for room-temperature x-ray and gamma ray detectors,” *Journal of crystal growth*, vol. 184, pp. 1302–1312, 1998.
- [60] S. Kumar, A. Kapoor, A. Nagpal, S. Sharma, D. Verma, A. Kumar, R. Raman, and P. Basu, “Effect of substrate dislocations on the hg in-diffusion in cdznte substrates used for hgcdte epilayer growth,” *Journal of crystal growth*, vol. 297, no. 2, pp. 311–316, 2006.
- [61] T. Aoki, Y. Chang, G. Badano, J. Zhao, C. Grein, S. Sivananthan, and D. J. Smith, “Defect characterization for epitaxial hgcdte alloys by electron microscopy,” *Journal of crystal growth*, vol. 265, no. 1-2, pp. 224–234, 2004.

- [62] Z. Tsybrii, Y. Bezsmolnyy, K. Svezhentsova, M. Vuichyk, I. Lysiuk, M. Apatska, M. Smolii, N. Dmytruk, S. Bunchuk, K. Andreeva, *et al.*, “HgCdTe/cdZnTe lpe epitaxial layers: From material growth to applications in devices,” *Journal of Crystal Growth*, vol. 529, p. 125295, 2020.
- [63] S. Zhang and X.-N. Hu, “Effect of thermal stress on the performance of HgCdTe/Si diodes and FPAs,” *Semiconductor science and technology*, vol. 27, no. 11, p. 115009, 2012.
- [64] P. Gergaud, A. Jonchere, B. Amstatt, X. Baudry, D. Brellier, and P. Ballet, “X-ray diffraction investigation of thermoelastic properties of HgCdTe/cdZnTe structures,” *Journal of electronic materials*, vol. 41, no. 10, pp. 2694–2699, 2012.
- [65] T. Skauli, R. Haakenaasen, and T. Colin, “Thermal expansion behaviour of CdHgTe epitaxial layers on CdZnTe substrates,” *Journal of crystal growth*, vol. 241, no. 1-2, pp. 39–44, 2002.
- [66] R. Jacobs, L. Almeida, J. Markunas, J. Pellegrino, M. Groenert, M. Jaime-Vasquez, N. Mahadik, C. Andrews, S. Qadri, T. Lee, *et al.*, “Relevance of thermal mismatch in large-area composite substrates for HgCdTe heteroepitaxy,” *Journal of electronic materials*, vol. 37, no. 9, pp. 1480–1487, 2008.
- [67] M. Martyniuk, R. Sewell, C. Musca, J. Dell, and L. Faraone, “Determination of HgCdTe elasto-plastic properties using nanoindentation,” *Journal of electronic materials*, vol. 35, no. 6, pp. 1197–1205, 2006.
- [68] M. Shkir, V. Ganesh, S. AlFaify, A. Black, E. Dieguez, and G. Bhagavan-narayana, “VGF bulk growth, crystalline perfection and mechanical studies of CdZnTe single crystal: A detector grade materials,” *Journal of Alloys and Compounds*, vol. 686, pp. 438–446, 2016.
- [69] R. Irwan, H. Huang, H. Zheng, and H. Wu, “Mechanical properties and material removal characteristics of soft-brittle HgCdTe single crystals,” *Materials Science and Engineering: A*, vol. 559, pp. 480–485, 2013.
- [70] N. Tit and A. Al-Zarouni, “The electronic properties of the strained CdTe/ZnTe

(001) superlattices,” *Journal of Physics: Condensed Matter*, vol. 14, no. 34, p. 7835, 2002.

- [71] M. Schall, M. Walther, and P. U. Jepsen, “Fundamental and second-order phonon processes in cdte and znte,” *Physical Review B*, vol. 64, no. 9, p. 094301, 2001.
- [72] H. Singh, P. Singh, A. Thakur, T. Singh, and J. Sharma, “Nanocrystalline $\text{zn}_{1-x}\text{te}_x$ ($x=0, 5, 20, 30, 40, 50$) thin films: Structural, optical and electrical properties,” *Materials Science in Semiconductor Processing*, vol. 75, pp. 276–282, 2018.
- [73] F. E. H. Hassan, B. Al Shafaay, H. Meradji, S. Ghemid, H. Belkhir, and M. Korrek, “Ab initio study of the fundamental properties of hgse, hgte and their $\text{hg}_{1-x}\text{se}_x$ alloys,” *Physica Scripta*, vol. 84, no. 6, p. 065601, 2011.
- [74] A. Merad, M. Kanoun, G. Merad, J. Cibert, and H. Aourag, “Full-potential investigation of the electronic and optical properties of stressed cdte and znte,” *Materials chemistry and physics*, vol. 92, no. 2-3, pp. 333–339, 2005.
- [75] S. Mnasri, S. A.-B. Nasrallah, N. Sfina, N. Bouarissa, and M. Said, “Electronic, lattice vibration and mechanical properties of cdte, znte, mnste, mgte, hgte and their ternary alloys,” *Semiconductor science and technology*, vol. 24, no. 9, p. 095008, 2009.
- [76] R. Cottam and G. Saunders, “The elastic behaviour of mercury telluride,” *Journal of Physics and Chemistry of Solids*, vol. 36, no. 3, pp. 187–192, 1975.
- [77] D. Bagot, R. Granger, and S. Rolland, “Thermal expansion coefficient and bond strength in $\text{hg}_{1-x}\text{cd}_x\text{te}$ and $\text{hg}_{1-x}\text{zn}_x\text{te}$,” *physica status solidi (b)*, vol. 177, no. 2, pp. 295–308, 1993.
- [78] A. Strauss, “The physical properties of cadmium telluride,” *Revue de Physique Appliquée*, vol. 12, no. 2, pp. 167–184, 1977.
- [79] M. Kanoun, W. Sekkal, H. Aourag, and G. Merad, “Molecular-dynamics study of the structural, elastic and thermodynamic properties of cadmium telluride,” *Physics Letters A*, vol. 272, no. 1-2, pp. 113–118, 2000.

- [80] M. Yamada, K. Yamamoto, and K. Abe, “Elastic and photoelastic constants of zn₂te measured by brillouin scattering,” *Journal of Physics D: Applied Physics*, vol. 10, no. 10, p. 1309, 1977.
- [81] T. Alper and G. Saunders, “The elastic constants of mercury telluride,” *Journal of Physics and Chemistry of Solids*, vol. 28, no. 9, pp. 1637–1642, 1967.
- [82] S. Bai, D. Tian, and F. Kong, “Innovative thermo-mechanical design for large format cryogenic infrared focal plane assembly,” in *AOPC 2021: Infrared Device and Infrared Technology*, vol. 12061, pp. 356–361, SPIE, 2021.
- [83] W. Zhang, Z. Ye, and X. Chen, “A fea study on thermal stress of hgcdte infrared focal plane arrays detector,” in *Infrared Technology and Applications XLIV*, vol. 10624, p. 106241X, International Society for Optics and Photonics, 2018.
- [84] L. Duperrex, R. Pesci, P. Le Boterf, and O. Maillart, “Simulation and measurement of residual stress and warpage in a hgcdte-based infrared detector at 100 k,” *Materials Science and Engineering: A*, vol. 813, p. 141148, 2021.
- [85] N. Sukumar, D. Srolovitz, T. Baker, and J.-H. Prevost, “Brittle fracture in polycrystalline microstructures with the extended finite element method,” *International Journal for Numerical Methods in Engineering*, vol. 56, no. 14, pp. 2015–2037, 2003.
- [86] N. Sukumar, N. Moës, B. Moran, and T. Belytschko, “Extended finite element method for three-dimensional crack modelling,” *International journal for numerical methods in engineering*, vol. 48, no. 11, pp. 1549–1570, 2000.
- [87] D. Wilson, W. Wan, and F. P. Dunne, “Microstructurally-sensitive fatigue crack growth in hcp, bcc and fcc polycrystals,” *Journal of the Mechanics and Physics of Solids*, vol. 126, pp. 204–225, 2019.
- [88] G. I. Barenblatt, “The formation of equilibrium cracks during brittle fracture. general ideas and hypotheses. axially-symmetric cracks,” *Journal of applied mathematics and mechanics*, vol. 23, no. 3, pp. 622–636, 1959.
- [89] H. D. Espinosa and P. D. Zavattieri, “A grain level model for the study of failure initiation and evolution in polycrystalline brittle materials. part i: Theory and

numerical implementation,” *Mechanics of Materials*, vol. 35, no. 3-6, pp. 333–364, 2003.

- [90] H. D. Espinosa and P. D. Zavattieri, “A grain level model for the study of failure initiation and evolution in polycrystalline brittle materials. part ii: Numerical examples,” *Mechanics of Materials*, vol. 35, no. 3-6, pp. 365–394, 2003.
- [91] V. Azzi and S. W. Tsai, “Anisotropic strength of composites,” *Experimental mechanics*, vol. 5, no. 9, pp. 283–288, 1965.
- [92] R. Hill, *The mathematical theory of plasticity*, vol. 11. Oxford university press, 1998.
- [93] S. W. Tsai and E. M. Wu, “A general theory of strength for anisotropic materials,” *Journal of composite materials*, vol. 5, no. 1, pp. 58–80, 1971.
- [94] A. A. Griffith, “Vi. the phenomena of rupture and flow in solids,” *Philosophical transactions of the royal society of london. Series A, containing papers of a mathematical or physical character*, vol. 221, no. 582-593, pp. 163–198, 1921.
- [95] C. Miehe, F. Welschinger, and M. Hofacker, “Thermodynamically consistent phase-field models of fracture: Variational principles and multi-field fe implementations,” *International journal for numerical methods in engineering*, vol. 83, no. 10, pp. 1273–1311, 2010.
- [96] C. Miehe, M. Hofacker, and F. Welschinger, “A phase field model for rate-independent crack propagation: Robust algorithmic implementation based on operator splits,” *Computer Methods in Applied Mechanics and Engineering*, vol. 199, no. 45-48, pp. 2765–2778, 2010.
- [97] C. Miehe, F. Aldakheel, and A. Raina, “Phase field modeling of ductile fracture at finite strains: A variational gradient extended plasticity damage theory,” *International Journal of Plasticity*, vol. 84, pp. 1–32, 2016.
- [98] C. Miehe, H. Dal, L.-M. Schänzel, and A. Raina, “A phase-field model for chemo-mechanical induced fracture in lithium-ion battery electrode particles,” *International Journal for Numerical Methods in Engineering*, vol. 106, no. 9, pp. 683–711, 2016.

- [99] C. Miehe and S. Mauthe, “Phase field modeling of fracture in multi-physics problems. part iii. crack driving forces in hydro-poro-elasticity and hydraulic fracturing of fluid-saturated porous media,” *Computer Methods in Applied Mechanics and Engineering*, vol. 304, pp. 619–655, 2016.
- [100] C. Miehe, M. Hofacker, L.-M. Schänzel, and F. Aldakheel, “Phase field modeling of fracture in multi-physics problems. part ii. coupled brittle-to-ductile failure criteria and crack propagation in thermo-elastic–plastic solids,” *Computer Methods in Applied Mechanics and Engineering*, vol. 294, pp. 486–522, 2015.
- [101] C. Miehe, L.-M. Schänzel, and H. Ulmer, “Phase field modeling of fracture in multi-physics problems. part i. balance of crack surface and failure criteria for brittle crack propagation in thermo-elastic solids,” *Computer Methods in Applied Mechanics and Engineering*, vol. 294, pp. 449–485, 2015.
- [102] B. Li, C. Peco, D. Millán, I. Arias, and M. Arroyo, “Phase-field modeling and simulation of fracture in brittle materials with strongly anisotropic surface energy,” *International Journal for Numerical Methods in Engineering*, vol. 102, no. 3-4, pp. 711–727, 2015.
- [103] S. Teichtmeister, D. Kienle, F. Aldakheel, and M.-A. Keip, “Phase field modeling of fracture in anisotropic brittle solids,” *International Journal of Non-Linear Mechanics*, vol. 97, pp. 1–21, 2017.
- [104] T.-T. Nguyen, J. Réthoré, J. Yvonnet, and M.-C. Baietto, “Multi-phase-field modeling of anisotropic crack propagation for polycrystalline materials,” *Computational Mechanics*, vol. 60, no. 2, pp. 289–314, 2017.
- [105] J. Clayton and J. Knap, “Phase field modeling of directional fracture in anisotropic polycrystals,” *Computational Materials Science*, vol. 98, pp. 158–169, 2015.
- [106] O. Gültekin, H. Dal, and G. A. Holzapfel, “A phase-field approach to model fracture of arterial walls: theory and finite element analysis,” *Computer methods in applied mechanics and engineering*, vol. 312, pp. 542–566, 2016.

- [107] M. Ambati, T. Gerasimov, and L. De Lorenzis, “Phase-field modeling of ductile fracture,” *Computational Mechanics*, vol. 55, no. 5, pp. 1017–1040, 2015.
- [108] H. Dal, O. Gültekin, F. Aksu Denli, and G. A. Holzapfel, “Phase-field models for the failure of anisotropic continua,” *PAMM*, vol. 17, no. 1, pp. 91–94, 2017.
- [109] F. A. Denli, O. Gültekin, G. A. Holzapfel, and H. Dal, “A phase-field model for fracture of unidirectional fiber-reinforced polymer matrix composites,” *Computational Mechanics*, vol. 65, no. 4, pp. 1149–1166, 2020.
- [110] C. V. Verhoosel and R. de Borst, “A phase-field model for cohesive fracture,” *International Journal for numerical methods in Engineering*, vol. 96, no. 1, pp. 43–62, 2013.
- [111] L. De Lorenzis, A. McBride, and B. D. Reddy, “Phase-field modelling of fracture in single crystal plasticity,” *GAMM-Mitteilungen*, vol. 39, no. 1, pp. 7–34, 2016.
- [112] J. Clayton and J. Knap, “Phase-field analysis of fracture-induced twinning in single crystals,” *Acta Materialia*, vol. 61, no. 14, pp. 5341–5353, 2013.
- [113] A. Abdollahi and I. Arias, “Phase-field modeling of the coupled microstructure and fracture evolution in ferroelectric single crystals,” *Acta Materialia*, vol. 59, no. 12, pp. 4733–4746, 2011.
- [114] C. A. Traynor, J. B. Anderson, and B. M. Boghosian, “A quantum monte carlo calculation of the ground state energy of the hydrogen molecule,” *The Journal of chemical physics*, vol. 94, no. 5, pp. 3657–3664, 1991.
- [115] J. B. Anderson, “A random-walk simulation of the schrödinger equation: $H+3$,” *The Journal of Chemical Physics*, vol. 63, no. 4, pp. 1499–1503, 1975.
- [116] W. Foulkes, L. Mitas, R. Needs, and G. Rajagopal, “Quantum monte carlo simulations of solids,” *Reviews of Modern Physics*, vol. 73, no. 1, p. 33, 2001.
- [117] J. D. Watts and R. J. Bartlett, “Economical triple excitation equation-of-motion coupled-cluster methods for excitation energies,” *Chemical Physics Letters*, vol. 233, no. 1-2, pp. 81–87, 1995.

- [118] J. A. Moriarty, “Density-functional formulation of the generalized pseudopotential theory. ii,” *Physical Review B*, vol. 26, no. 4, p. 1754, 1982.
- [119] G. Bachelet, D. Hamann, and M. Schlüter, “Pseudopotentials that work: From h to pu,” *Physical Review B*, vol. 26, no. 8, p. 4199, 1982.
- [120] N. Troullier and J. L. Martins, “Efficient pseudopotentials for plane-wave calculations,” *Physical review B*, vol. 43, no. 3, p. 1993, 1991.
- [121] D. J. Singh and L. Nordstrom, *Planewaves, Pseudopotentials, and the LAPW method*. Springer Science & Business Media, 2006.
- [122] P. Hohenberg and W. Kohn, “Inhomogeneous electron gas,” *Physical review*, vol. 136, no. 3B, p. B864, 1964.
- [123] W. Kohn and L. J. Sham, “Self-consistent equations including exchange and correlation effects,” *Physical review*, vol. 140, no. 4A, p. A1133, 1965.
- [124] A. Canning, L. Wang, A. Williamson, and A. Zunger, “Parallel empirical pseudopotential electronic structure calculations for million atom systems,” *Journal of Computational Physics*, vol. 160, no. 1, pp. 29–41, 2000.
- [125] M. Ferhat, A. Zaoui, M. Certier, and B. Khelifa, “Applicability of the empirical pseudopotential method to semiconductors with d valence electrons,” *Physics Letters A*, vol. 216, no. 1-5, pp. 187–190, 1996.
- [126] J. Barthelat, P. Durand, and A. Serafini, “Non-empirical pseudopotentials for molecular calculations: I. the psibmol algorithm and test calculations,” *Molecular Physics*, vol. 33, no. 1, pp. 159–180, 1977.
- [127] J. H. Skone, M. Govoni, and G. Galli, “Nonempirical range-separated hybrid functionals for solids and molecules,” *Physical Review B*, vol. 93, no. 23, p. 235106, 2016.
- [128] J. P. Perdew, “Accurate density functional for the energy: Real-space cutoff of the gradient expansion for the exchange hole,” *Physical Review Letters*, vol. 55, no. 16, p. 1665, 1985.
- [129] J. P. Perdew, A. Ruzsinszky, G. I. Csonka, O. A. Vydrov, G. E. Scuseria, L. A. Constantin, X. Zhou, and K. Burke, “Restoring the density-gradient expansion

- for exchange in solids and surfaces,” *Physical review letters*, vol. 100, no. 13, p. 136406, 2008.
- [130] R. Peverati and D. G. Truhlar, “Improving the accuracy of hybrid meta-gga density functionals by range separation,” *The Journal of Physical Chemistry Letters*, vol. 2, no. 21, pp. 2810–2817, 2011.
- [131] L. Simón and J. M. Goodman, “How reliable are dft transition structures? comparison of gga, hybrid-meta-gga and meta-gga functionals,” *Organic & biomolecular chemistry*, vol. 9, no. 3, pp. 689–700, 2011.
- [132] Y. Zhao and D. G. Truhlar, “Density functional theory for reaction energies: test of meta and hybrid meta functionals, range-separated functionals, and other high-performance functionals,” *Journal of Chemical Theory and Computation*, vol. 7, no. 3, pp. 669–676, 2011.
- [133] P. Giannozzi, S. Baroni, N. Bonini, M. Calandra, R. Car, C. Cavazzoni, D. Ceresoli, G. L. Chiarotti, M. Cococcioni, I. Dabo, *et al.*, “Quantum espresso: a modular and open-source software project for quantum simulations of materials,” *Journal of physics: Condensed matter*, vol. 21, no. 39, p. 395502, 2009.
- [134] P. Giannozzi, O. Andreussi, T. Brumme, O. Bunau, M. B. Nardelli, M. Calandra, R. Car, C. Cavazzoni, D. Ceresoli, M. Cococcioni, *et al.*, “Advanced capabilities for materials modelling with quantum espresso,” *Journal of Physics: Condensed Matter*, vol. 29, no. 46, p. 465901, 2017.
- [135] S. Scandolo, P. Giannozzi, C. Cavazzoni, S. de Gironcoli, A. Pasquarello, and S. Baroni, “First-principles codes for computational crystallography in the quantum-espresso package,” *Zeitschrift für Kristallographie-Crystalline Materials*, vol. 220, no. 5-6, pp. 574–579, 2005.
- [136] E. Wimmer, M. Christensen, V. Eyert, W. Wolf, D. Reith, X. Rozanska, C. Freeman, and P. Saxe, “Computational materials engineering: Recent applications of VASP in the MedeA® software environment,” *Journal of the Korean Ceramic Society*, vol. 53, no. 3, pp. 263–272, 2016.

- [137] S. J. Clark, M. D. Segall, C. J. Pickard, P. J. Hasnip, M. I. Probert, K. Refson, and M. C. Payne, “First principles methods using castep,” *Zeitschrift für kristallographie-crystalline materials*, vol. 220, no. 5-6, pp. 567–570, 2005.
- [138] R. Car and M. Parrinello, “Unified approach for molecular dynamics and density-functional theory,” *Physical review letters*, vol. 55, no. 22, p. 2471, 1985.
- [139] X. Gonze, B. Amadon, P.-M. Anglade, J.-M. Beuken, F. Bottin, P. Boulanger, F. Bruneval, D. Caliste, R. Caracas, M. Côté, *et al.*, “Abinit: First-principles approach to material and nanosystem properties,” *Computer Physics Communications*, vol. 180, no. 12, pp. 2582–2615, 2009.
- [140] G. A. Holzapfel, *Nonlinear Solid Mechanics. A Continuum Approach for Engineering*. John Wiley & Sons, 2000.
- [141] J. E. Marsden and T. J. Hughes, *Mathematical foundations of elasticity*. Courier Corporation, 1994.
- [142] R. W. Ogden, *Non-linear elastic deformations*. Courier Corporation, 1997.
- [143] D. Noda, T. Aoki, Y. Nakanishi, and Y. Hatanaka, “Growth of cdznte and cdsete crystals for p–i–n radiation detectors,” *Journal of crystal growth*, vol. 214, pp. 1121–1124, 2000.
- [144] H. Malkas, S. Kaya, and E. Yilmaz, “Effects of substrate temperature on the microstructure and morphology of cdznte thin films,” *Journal of electronic materials*, vol. 43, pp. 4011–4017, 2014.
- [145] Y. Wang, J. Wang, H. Zhang, V. Manga, S. Shang, L. Chen, and Z. Liu, “A first-principles approach to finite temperature elastic constants,” *Journal of Physics: Condensed Matter*, vol. 22, no. 22, p. 225404, 2010.
- [146] S.-L. Shang, H. Zhang, Y. Wang, and Z.-K. Liu, “Temperature-dependent elastic stiffness constants of α - and θ -Al₂O₃ from first-principles calculations,” *Journal of Physics: Condensed Matter*, vol. 22, no. 37, p. 375403, 2010.
- [147] X. Yan, Y. Lin, L. Li, and F. Sun, “Temperature-dependent elastic and thermodynamic properties of Fe₃Ga (Do₃, L12, and DO19) alloys from first-

- principles calculations,” *physica status solidi (b)*, vol. 253, no. 11, pp. 2236–2244, 2016.
- [148] B. Karki, R. M. Wentzcovitch, S. De Gironcoli, and S. Baroni, “High-pressure lattice dynamics and thermoelasticity of MgO,” *Physical Review B*, vol. 61, no. 13, p. 8793, 2000.
- [149] R. E. Cohen and O. Gülseren, “Thermal equation of state of tantalum,” *Physical Review B - Condensed Matter and Materials Physics*, vol. 63, no. 22, pp. 1–10, 2001.
- [150] N. D. Mermin, “Thermal properties of the inhomogeneous electron gas,” *Physical Review*, vol. 137, no. 5A, pp. 1–3, 1965.
- [151] R. Arroyave, D. Shin, and Z. K. Liu, “Ab initio thermodynamic properties of stoichiometric phases in the Ni-Al system,” *Acta Materialia*, vol. 53, no. 6, pp. 1809–1819, 2005.
- [152] A. Erba, M. Shahrokhi, R. Moradian, and R. Dovesi, “On how differently the quasi-harmonic approximation works for two isostructural crystals: Thermal properties of periclase and lime,” *Journal of Chemical Physics*, vol. 142, no. 4, pp. 0–9, 2015.
- [153] R. G. Parr and W. Yang, “Density-functional theory of atoms and molecules. international Series of Monographs on Chemistry,” *Oxford University Press, New York*, vol. 3, pp. 14312–14321, 1994.
- [154] J. P. Perdew, K. Burke, and M. Ernzerhof, “Generalized gradient approximation made simple,” *Physical review letters*, vol. 77, no. 18, p. 3865, 1996.
- [155] J. Hafner, “Ab-initio simulations of materials using VASP: Density-functional theory and beyond,” *Journal of computational chemistry*, vol. 29, no. 13, pp. 2044–2078, 2008.
- [156] H. J. Monkhorst and J. D. Pack, “Special points for Brillouin-zone integrations,” *Physical review B*, vol. 13, no. 12, p. 5188, 1976.
- [157] C.-L. Fu and K.-M. Ho, “First-principles calculation of the equilibrium

- ground-state properties of transition metals: Applications to Nb and Mo,” *Physical Review B*, vol. 28, no. 10, p. 5480, 1983.
- [158] Y. Le Page and P. Saxe, “Symmetry-general least-squares extraction of elastic coefficients from ab initio total energy calculations,” *Physical Review B*, vol. 63, no. 17, p. 174103, 2001.
- [159] Y. Le Page and P. Saxe, “Symmetry-general least-squares extraction of elastic data for strained materials from ab initio calculations of stress,” *Physical Review B*, vol. 65, no. 10, p. 104104, 2002.
- [160] B. Mayer, H. Anton, E. Bott, M. Methfessel, J. Sticht, J. Harris, and P. Schmidt, “Ab-initio calculation of the elastic constants and thermal expansion coefficients of laves phases,” *Intermetallics*, vol. 11, no. 1, pp. 23–32, 2003.
- [161] X.-Q. Chen, H. Niu, D. Li, and Y. Li, “Modeling hardness of polycrystalline materials and bulk metallic glasses,” *Intermetallics*, vol. 19, no. 9, pp. 1275–1281, 2011.
- [162] M. Zacharias and F. Giustino, “One-shot calculation of temperature-dependent optical spectra and phonon-induced band-gap renormalization,” *Physical Review B*, vol. 94, no. 7, p. 075125, 2016.
- [163] F. Tran and P. Blaha, “Accurate band gaps of semiconductors and insulators with a semilocal exchange-correlation potential,” *Physical Review Letters*, vol. 102, no. 22, p. 226401, 2009.
- [164] P. Dutta, H. Bhat, and V. Kumar, “The physics and technology of gallium antimonide: An emerging optoelectronic material,” *Journal of applied physics*, vol. 81, no. 9, pp. 5821–5870, 1997.
- [165] P. Haas, F. Tran, and P. Blaha, “Calculation of the lattice constant of solids with semilocal functionals,” *Physical Review B*, vol. 79, no. 8, p. 085104, 2009.
- [166] G. I. Csonka, J. P. Perdew, A. Ruzsinszky, P. H. Philipsen, S. Lebègue, J. Paier, O. A. Vydrov, and J. G. Ángyán, “Assessing the performance of recent density functionals for bulk solids,” *Physical Review B*, vol. 79, no. 15, p. 155107, 2009.

- [167] P. Sparks and C. Swenson, “Thermal expansions from 2 to 40K of Ge, Si, and four III-V compounds,” *Physical Review*, vol. 163, no. 3, p. 779, 1967.
- [168] L. Lindsay, D. Broido, and T. Reinecke, “Ab initio thermal transport in compound semiconductors,” *Physical Review B*, vol. 87, no. 16, p. 165201, 2013.
- [169] R. Mohammad, Ş. Katircioğlu, and M. El-Hasan, “The electronic band structure of InN, InAs and InSb compounds,” *Journal of materials science*, vol. 43, no. 8, pp. 2935–2946, 2008.
- [170] H. Landolt, R. Börnstein, O. Madelung, W. Pies, A. Weiss, G. Will, K. Hellwege, and A. Hellwege, *Numerical Data and Functional Relationships in Science and Technology: New Series. Crystal and Solid State Physics. Crystal Structure Data of Inorganic Compounds. Key Elements: Si, Ge, Sn, Pb; B, Al, Ga, In, Tl; Be. Key Elements Si, Ge, Sn, Pb. Key Element Si (Substance Numbers D1... D1168)/Wolfgang Pies, Alarich Weiss in Cooperation with Georg Will; Editors: K.-H. Hellwege and AM Hellwege*. Springer., 1985.
- [171] A. L. Miranda, B. Xu, O. Hellman, A. H. Romero, and M. J. Verstraete, “Ab initio calculation of the thermal conductivity of indium antimonide,” *Semiconductor Science and Technology*, vol. 29, no. 12, 2014.
- [172] W. Boyle and R. Sladek, “Elastic constants and lattice anharmonicity of GaSb and GaP from ultrasonic-velocity measurements between 4.2 and 300 K,” *Physical Review B*, vol. 11, no. 8, p. 2933, 1975.
- [173] L. Slutsky and C. Garland, “Elastic constants of indium antimonide from 4.2K to 300K,” *Physical Review*, vol. 113, no. 1, p. 167, 1959.
- [174] R. Pässler, “Non-debye heat capacity formula refined and applied to GaP, GaAs, GaSb, InP, InAs, and InSb,” *AIP Advances*, vol. 3, no. 8, p. 082108, 2013.
- [175] A. Pashinkin, V. Fedorov, A. Malkova, and M. Mikhailova, “Heat capacity of GaB V and InB V (BV= P, As, Sb) above 298 K,” *Inorganic Materials*, vol. 46, no. 9, pp. 1007–1012, 2010.

- [176] R. Greenough and S. Palmer, “The elastic constants and thermal expansion of single-crystal cdte,” *Journal of Physics D: Applied Physics*, vol. 6, no. 5, p. 587, 1973.
- [177] B. Lee, “Elastic constants of znte and znse between 77–300 k,” *Journal of Applied Physics*, vol. 41, no. 7, pp. 2984–2987, 1970.
- [178] X. Wu, L. Liu, W. Li, R. Wang, and Q. Liu, “Effect of temperature on elastic constants, generalized stacking fault energy and dislocation cores in MgO and CaO,” *Computational Condensed Matter*, vol. 1, pp. 38–44, 2014.
- [179] D. Orlikowski, P. Söderlind, and J. A. Moriarty, “First-principles thermoelasticity of transition metals at high pressure: Tantalum prototype in the quasiharmonic limit,” *Physical Review B*, vol. 74, p. 054109, 2006.
- [180] K. Gavrichev, G. Sharpataya, V. Guskov, J. Greenberg, T. Feltgen, M. Fiederle, and K. Benz, “High-temperature heat capacity and thermodynamic functions of zinc telluride,” *Thermochimica Acta*, vol. 381, no. 2, pp. 133–138, 2002.
- [181] K. Gavrichev, V. Guskov, J. Greenberg, T. Feltgen, M. Fiederle, and K. Benz, “Low-temperature heat capacity of ZnTe,” *The Journal of Chemical Thermodynamics*, vol. 34, no. 12, pp. 2041–2047, 2002.
- [182] M. Gambino, V. Vassiliev, and J. Bros, “Molar heat capacities of CdTe, HgTe and CdTe HgTe alloys in the solid state,” *Journal of Alloys and Compounds*, vol. 176, no. 1, pp. 13–24, 1991.
- [183] W. Markert, H. Nieke, and D. Spiegler, “Halbleiteiereigenschaften von Telluriden, X. Wärmeleitfähigkeit und elektrische Eigenschaften des Systems HgTe CdTe,” *Annalen der Physik*, vol. 476, no. 7-8, pp. 387–401, 1968.
- [184] F. Kelemen, E. Cruceanu, and D. Niculescu, “Untersuchung einiger thermischer Eigenschaften der Verbindungen HgSe, HgTe und ZnTe,” *Physica Status Solidi (B)*, vol. 11, no. 2, pp. 865–872, 1965.
- [185] A. Demidenko, “Heat Capacity of CdS, CdSe, and CdTe,” *Izv. Akad. Nauk SSSR, Neorg. Mater.*, vol. 5, no. 2, pp. 252–255, 1969.

- [186] D. T. Queheillalt and H. N. Wadley, "Temperature dependence of the elastic constants of solid and liquid $\text{cd}_{0.96}\text{zn}_{0.04}\text{te}$ obtained by laser ultrasound," *Journal of applied physics*, vol. 83, no. 8, pp. 4124–4133, 1998.
- [187] N. Kolesnikov, E. Borisenko, D. Borisenko, and B. Gnesin, "Ceramic materials made of CdTe and Cd-Zn-Te nanocrystalline powders," *Open Chemistry*, vol. 9, no. 4, pp. 619–623, 2011.
- [188] R. Irwan, "Deformation characteristics and removal mechanisms of soft-brittle solids: single crystals of mercury cadmium telluride (HgCdTe) and cadmium zinc telluride (CdZnTe)," *The University of Queensland, Master of Philosophy*, 2015.
- [189] S. Saib, S. Benyettou, and N. Bouarissa, "Ab initio calculation of fundamental properties of $\text{cd}_x\text{zn}_{1-x}\text{te}$ ternary alloys in the zinc-blende structure," *Physica E: Low-dimensional Systems and Nanostructures*, vol. 68, pp. 184–189, 2015.
- [190] Y. Tsay, S. Mitra, and J. Vetelino, "Temperature dependence of energy gaps in some ii–vi compounds," *Journal of Physics and Chemistry of Solids*, vol. 34, no. 12, pp. 2167–2175, 1973.
- [191] K. Strzałkowski, "The composition effect on the thermal and optical properties across cdznte crystals," *Journal of Physics D: Applied Physics*, vol. 49, no. 43, p. 435106, 2016.
- [192] S. N. Moger, D. U. Shanubhogue, R. Keshav, and M. Mahesha, "Spectroscopic and electrical analysis of vacuum co-evaporated $\text{Cd}_x\text{Zn}_{1-x}\text{Te}$ thin films," *Superlattices and Microstructures*, vol. 142, p. 106521, 2020.
- [193] R. Nahory, M. Pollack, W. Johnston Jr, and R. Barns, "Band gap versus composition and demonstration of vegard's law for $\text{in}_{1-x}\text{ga}_x\text{as}_y\text{p}_{1-y}$ lattice matched to inp ," *Applied Physics Letters*, vol. 33, no. 7, pp. 659–661, 1978.
- [194] Y.-K. Kuo, B.-T. Liou, S.-H. Yen, and H.-Y. Chu, "Vegard's law deviation in lattice constant and band gap bowing parameter of zincblende $\text{inxga}_{1-x}\text{n}$," *Optics Communications*, vol. 237, no. 4-6, pp. 363–369, 2004.

- [195] M. Daraselia, G. Brill, J. Garland, V. Nathan, and S. Sivananthan, “In-situ control of temperature and alloy composition of $\text{Cd}_{1-x}\text{Zn}_x\text{Te}$ grown by molecular beam epitaxy,” *Journal of Electronic Materials*, vol. 29, pp. 742–747, 2000.
- [196] R. Armstrong and W. Elban, “Macro-to nano-indentation hardness stress–strain aspects of crystal elastic/plastic/cracking behaviors,” *Experimental mechanics*, vol. 50, no. 4, pp. 545–552, 2010.
- [197] R. F. Gibson, “A review of recent research on nanoindentation of polymer composites and their constituents,” *Composites Science and Technology*, vol. 105, pp. 51–65, 2014.
- [198] A. Zeilinger, J. Todt, C. Krywka, M. Müller, W. Ecker, B. Sartory, M. Meindl-humer, M. Stefenelli, R. Daniel, C. Mitterer, *et al.*, “In-situ observation of cross-sectional microstructural changes and stress distributions in fracturing tin thin film during nanoindentation,” *Scientific reports*, vol. 6, no. 1, pp. 1–14, 2016.
- [199] Y. Wang, L. Shang, P. Zhang, X. Yan, K. Zhang, S. Dou, J. Zhao, and Y. Li, “Measurement of viscoelastic properties for polymers by nanoindentation,” *Polymer Testing*, vol. 83, p. 106353, 2020.
- [200] W. C. Oliver and G. M. Pharr, “An improved technique for determining hardness and elastic modulus using load and displacement sensing indentation experiments,” *Journal of materials research*, vol. 7, no. 6, pp. 1564–1583, 1992.
- [201] W.-G. Jiang, J.-J. Su, and X.-Q. Feng, “Effect of surface roughness on nanoindentation test of thin films,” *Engineering Fracture Mechanics*, vol. 75, no. 17, pp. 4965–4972, 2008.
- [202] J. E. Jakes and D. S. Stone, “The edge effect in nanoindentation,” *Philosophical Magazine*, vol. 91, no. 7-9, pp. 1387–1399, 2011.
- [203] M. Königsberger, L. Zelaya-Lainez, O. Lahayne, B. L. Pichler, and C. Hellmich, “Nanoindentation-probed oliver-pharr half-spaces in alkali-activated slag-fly ash pastes: Multimethod identification of microelasticity and hardness,” *Mechanics of Advanced Materials and Structures*, pp. 1–12, 2021.

- [204] Y. Wang, D. Raabe, C. Klüber, and F. Roters, “Orientation dependence of nanoindentation pile-up patterns and of nanoindentation microtextures in copper single crystals,” *Acta materialia*, vol. 52, no. 8, pp. 2229–2238, 2004.
- [205] G. Muthupandi, K. R. Lim, Y.-S. Na, J. Park, D. Lee, H. Kim, S. Park, and Y. S. Choi, “Pile-up and sink-in nanoindentation behaviors in alcoerfeni multi-phase high entropy alloy,” *Materials Science and Engineering: A*, vol. 696, pp. 146–154, 2017.
- [206] R. Radebaugh, “Cryocoolers: the state of the art and recent developments,” *Journal of Physics: Condensed Matter*, vol. 21, no. 16, p. 164219, 2009.
- [207] S. Kalácska, J. Ast, P. D. Ispánovity, J. Michler, and X. Maeder, “3d hr-ebstd characterization of the plastic zone around crack tips in tungsten single crystals at the micron scale,” *Acta Materialia*, vol. 200, pp. 211–222, 2020.
- [208] T. Nagoshi, S. Kozu, Y. Inoue, B. E. O’Rourke, and Y. Harada, “Fatigue damage assessment of sus316l using ebsd and pals measurements,” *Materials Characterization*, vol. 154, pp. 61–66, 2019.
- [209] S. Johnson, J. Vigil, J. James, C. Cockrum, W. Konkell, M. Kalisher, R. Risser, T. Tung, W. Hamilton, W. Ahlgren, *et al.*, “Mocvd grown cdzn te/gaas/si substrates for large-area hgcdte irfpas,” *Journal of electronic materials*, vol. 22, pp. 835–842, 1993.
- [210] G. Qin, J. Kong, J. Yang, Y. Ren, Y. Li, C. Yang, H. Li, J. Wang, J. Yu, Q. Qin, *et al.*, “Hgcdte films grown by mbe on czt (211) b substrates,” *Journal of Electronic Materials*, pp. 1–8, 2023.
- [211] P. Chadwick, M. Vianello, and S. C. Cowin, “A new proof that the number of linear elastic symmetries is eight,” *Journal of the Mechanics and Physics of Solids*, vol. 49, no. 11, pp. 2471–2492, 2001. The Jean-Paul Boehler Memorial Volume.
- [212] A. Masolin, P.-O. Bouchard, R. Martini, and M. Bernacki, “Thermo-mechanical and fracture properties in single-crystal silicon,” *Journal of Materials Science*, vol. 48, no. 3, pp. 979–988, 2013.

CURRICULUM VITAE

PERSONAL INFORMATION

Surname, Name: Balođlu, Eyüp Can

Nationality: Turkish (TC)

Date and Place of Birth: 31/07/1989, Ankara

e-mail: canbaloglu7@gmail.com

EDUCATION

Degree	Institution	Year of Graduation
M.S.	METU Mechanical Engineering Dept.	2016
B.S.	METU Mechanical Engineering Dept.	2012
High School	Hacı Ömer Tarman Anadolu Lisesi	2007

PROFESSIONAL EXPERIENCE

Year	Place	Enrollment
2012-Present	Aselsan Inc.	Full time
2011	Türk Henkel	Internship
2010	Turkish Aerospace Industries	Internship

PUBLICATIONS

Journal Papers

Baloglu Eyup Can, Ustunel Hande and Dal Hüsni, "Temperature-dependent thermoelectric properties of GaSb and InSb semiconductors: Identification through ab initio DFT simulations.", *Physica B: Condensed Matter*, 2022

International Conference Papers

Baloglu, Eyup Can, and Erkan Atasoy. "The Effect of Adhesive and Carrier Material Properties on Thermo-Mechanical Stresses of GaSb, InSb Semiconductors due to Cryocooling." *2021 IEEE 23rd Electronics Packaging Technology Conference (EPTC)*. IEEE, 2021.

Dennis, Joseph M., Esin Akca, Andy T. Tek, Gökhan Demirci, Alp Tolunguc, Eyup Can Baloglu, Thomas Antoni, Cagla Ozgit-Akgun, Robert D. Allen "Designing adhesives for cooled infrared detectors." *Electro-Optical and Infrared Systems: Technology and Applications XV. Vol. 10795. SPIE*, 2018.

Baloglu, Eyup Can, Okutucu Ozyurt Tuba, and Dursunkaya Zafer. "Investigation of Warpage Behavior of Silicon Semiconductor on a Silicon-Adhesive-Ceramic Integrated Structure at Cryogenic Temperatures." *Additional Papers and Presentations 2016.DPC (2016): 001751-001772. International Microelectronics Assembly and Packaging Society (IMAPS), Device Packaging Conference*, 2016.

National Conference Papers

Baloglu, Eyup Can, Okutucu Ozyurt Tuba, and Dursunkaya Zafer. "Mikroelektronik aygıtların düşük sıcaklıkta şekil değiştirmelerinin incelenmesi.", *20. Ulusal Isı Bilimi ve Tekniği Kongresi*, 2015.